Deep Underground Neutrino Experiment (DUNE)

DUNE Near Detector
Updated Conceptual Design Report

SAND Chapter

May 6, 2024

The DUNE Collaboration

DEEP UNDERGROUND NEUTRINO EXPERIMENT

1

Contents

List of Figures

List of Tables

Todo list

Chapter 1

System for on-Axis Neutrino Detection (SAND)

1.1 Overview

All DUNE accelerator-based physics studies use flux uncertainties assuming that parameters such as horn positions and currents are known to certain tolerances. Beamline instrumentation is being developed to monitor these parameters but many potential deviations from the tolerances are best identified by monitoring of the neutrino energy spectra in the ND for the distortions those deviations cause. Typical sources of beamline distortion are most easily seen and diagnosed in neutrino energy spectra measured on the beam axis and are diluted in off-axis spectra. However, the DUNE-PRISM measurement program (Ch. **??**) calls for the ND-LAr and ND-GAr to spend approximately 50% of the time collecting data at off-axis positions. DUNE-PRISM relies on the well understood relationship between the off-axis angle and the neutrino energy spectrum. It is essential to DUNE-PRISM that the beam remains stable while data are taken at different positions or, failing that, that distortions in the beam can be quickly identified and (eventually) modeled well. As a consequence, DUNE needs that a component of the ND complex [2] remain on-axis where beam monitoring is most sensitive and collects a sufficient number of ν_μ charged current (CC) interactions. This role of continuous monitoring system is filled by SAND (Fig. 1.1). Furthermore, it is noteworthy to observe that this detector must operate in high-rate environment and measure external backgrounds, including cosmic and beam-induced activity.

1.1.1 Requirements and SAND Role

The overarching requirements for SAND are to monitor on-axis spectrum and position information to detect representative changes in the neutrino beam (ND-05) and to operate in high rate environment (ND-06). The first requirement implies to monitor the rate of neutrino interactions on-axis with a sensitivity better than 1% in a week (ND-M8) and to measure the muon/neutrino energy and vertex distribution (ND-M9). According to the second overarching requirement SAND must separate cosmic rays, rock muons, and other beam-induced activity from the neutrino interactions in the fiducial volume (FV), and distinguish neutrino interactions also in pile-up condition (ND-M10).

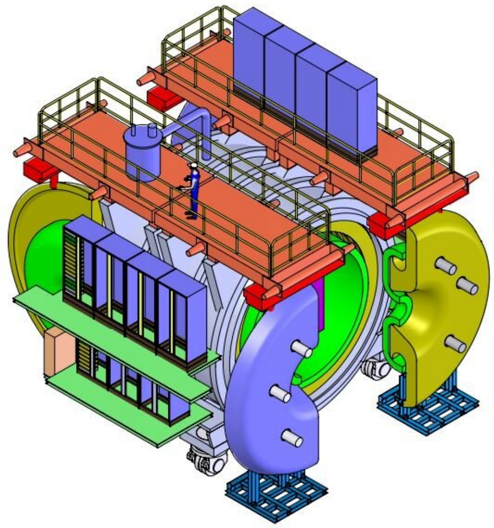

Figure 1.1: SAND sketch.

Measurement requirement ND-M8 To fulfill this requirement SAND must monitor the beam on-axis with a target mass that is large enough for the interaction rate of neutrinos to provide statistically significant feedback on changes in the beam over a short time period (one week). Regarding the collection and identification of ν_μ CC this mass is estimated to be more than 20 tons for reconstruction of p_μ and more than 5 tons for reconstruction of E_ν (ND-C5.1).

Measurement requirement ND-M9 SAND must measure the muon/neutrino energy and vertex distribution to detect representative changes in the beamline. Looking at the spectral variations, the muon/neutrino energy resolution must be $\sigma_{p_\mu}/p_\mu < 10\%$ at 5 GeV/c improving at 5% at 1 GeV/c, or $\sigma_{E_\nu}/E_\nu < 15\%$ (ND-C5.2). Furthermore, the interaction vertices in ν_μ CC events must be measured well enough to divide the sample spatially relative to the beam center. A reconstruction with a resolution < 5 cm is enough to distinguish interactions occurring over distances where the spectrum may vary (ND-C5.3).

Measurement requirement ND-M10 Due to the shallow site and the intensity of the neutrino beam, the ND operates in a high-rate environment due to cosmic rays, beam-induced background activity and neutrino interaction pile-up. In order to verify that these backgrounds are correctly accounted for and modeled, and to distinguish the neutrino interactions in the same time window SAND must have timing to identify and select activity occurring within the neutrino beam delivery window: $\sigma_t < 5$ ns on the tracker, $\sigma_t < 400$ ps on electromagnetic calorimeter (ECAL) hits (ND-C5.4). Better resolution (1 ns) on the tracker would further enable directionality capabilities. These timing requirements are also useful to fulfill the previous requirement about the vertex measurement.

1.1.2 The Overall Design of SAND

In summary, SAND must reconstruct the vertices in ν_μ CC interactions and the muons emanating from those vertices must be reconstructed with good momentum resolution over a broad momentum range (roughly $0.5 \lesssim p_\mu \lesssim 10$ GeV/c). This necessitates a tracking detector with a magnetic field.

As such, SAND is largely based on a reuse of the calorimeter (ECAL) and the solenoidal superconducting magnet from the K-LOng Experiment (KLOE) [3]. The KLOE detector was designed primarily for the study of CP violation in neutral kaon decays at the DAΦNE ϕ-factory. KLOE took data from April 1999 to March 2018. Throughout that time, the detector performance was stable. In the KLOE experiment, the inner volume of the magnet and ECAL was occupied by a large drift chamber.

In the DUNE ND, the detector itself will be installed so that neutrino beam enters through the side of the barrel, perpendicular to the magnetic field. The drift chamber has already been removed (Sec. 1.2.6) and the vacant volume will be instrumented according to the DUNE necessities. The 4π ECAL (Sec. 1.2) is useful as a target mass for the beam monitoring mission but also provides additional capabilities. The solenoid (Sec. 1.3) provides a 0.6 T magnetic field in a large volume ($\sim 43\ \mathrm{m}^3$) partially instrumented with a target and tracking system ("target/tracker"). It features hydrocarbon target masses and naturally provides for some additional capabilities. The remaining magnetized volume will be occupied by a thin LAr target (1 ton).

The tracking system (Sec. 1.5) fills most of the magnetic volume with orthogonal XY planes of straw tube tracker (STT) interleaved with various thin carbon and hydrocarbon layers to add mass and act as additional targets for neutrino interactions. A backup variant under study is a drift chamber (Sec. 1.5.2) with smaller number of channels.

The LAr element is not only a target. It is an imaging detector (Sec. 1.4), called GRanular Argon for Interactions of Neutrinos (GRAIN), and would be located inside the magnetic volume between the tracking region and the upstream inner edge of the ECAL. It is made by a cryostat shaped in an elliptical tube and instrumented with innovative devices devoted to the photon detection in the vacuum ultra-violet range. Two different devices are under test: lenses and coded masks. In both cases the photons are collected by silicon photomultiplier (SiPM) arrays. The tracker will allow the precise momentum reconstruction for particles exiting from GRAIN.

The performance studies that demonstrate how SAND fulfills the beam monitoring requirements are described in Sec. 1.11.8. Fulfilling the requirements also leads to a set of derived detector capabilities described below.

1.1.3 Derived SAND Capabilities

Because SAND is required to measure sign and momentum of muons, it is also capable of similar measurements of charged hadrons. The target/tracking systems provide particle identification by dE/dx. The ECAL is able to measure photon and electron energies by calorimetry, and adds to the particle identification capability. These capabilities stem from the beam monitoring requirements but allow SAND to conduct a neutrino interaction measurement program that augments DUNE's oscillation physics mission. In particular SAND adds the following capabilities:

- SAND is able to provide an independent measurement of the interaction rate and energy spectra of the ν_μ, $\bar{\nu}_\mu$, and ν_e, $\bar{\nu}_e$ beam components. The capability of SAND to identify and reconstruct different types of interactions will enable complementary measurements of both the normalization and energy dependence of the flux. This redundancy can be used to improve confidence in the extrapolation of the neutrino nd anti-neutrino fluxes to the far detector.

- Nuclear effects present a significant source of uncertainty for DUNE. There are large uncertainties in the modeling of (anti)neutrino-nucleus cross sections. In particular, final state interactions are not well modeled but change the composition of hadrons in the final state and the hadrons' energies. The choice of argon as the primary target nucleus in the ND is to mitigate the effect of these uncertainties in the ND to FD comparison. That said, things will not cancel perfectly in the near-to-far extrapolation, even with the implementation of DUNE-PRISM. SAND enables a program of measurements on nuclei other than argon (carbon and hydrocarbons) that may help constrain systematic uncertainties arising from nuclear effects.
- The hydrocarbon in the target/tracker results in a large event sample on carbon and also a smaller but still significant event sample on hydrogen. For some interaction channels, hydrogen enriched samples can be selected using transverse kinematic imbalance, or TKI, techniques [4–17]. The isolation of a sample enriched in neutrino-hydrogen interactions is very valuable since uncertainties due to nuclear effects are only present in the background and may potentially be mitigated by kinematic sidebands or the use of carbon targets with acceptance identical to the hydrocarbon ones. These targets are foreseen to allow a model independent background subtraction.
- SAND is able to combine information from the ECAL and tracker/target to tag neutrons and measure their energy. The use of this information will improve the neutrino energy resolution and reduce the bias in the neutrino energy measurement, leading to a reduction in the related systematics. Neutron measurements can also improve the reconstruction of event kinematics.

Summarizing the contribution by SAND to the DUNE scientific program is not confined to monitor variations of the neutrino beam. SAND can measure different neutrino spectra, and reduce the systematics in the extrapolation of the beam at the FD. Furthermore, it can constrain the cross section and the nuclear effect models.

1.1.4 Opportunities for SAND

$\nu - Ar$ cross section ...

Search for Heavy Neutral Leptons...

1.2 Lead/Scintillating-Fiber Calorimeter (ECAL)

1.2.1 ECAL Design and Structure

The KLOE ECAL [3] is a fine sampling lead-scintillating calorimeter with photomultiplier tube (PMT) readout. The central part (barrel) approximating a cylindrical shell of 4 m inner diameter, 4.3 m active length and 23 cm thickness ($\sim 15\ X_0$), consists of 24 modules with trapezoidal cross-section and fibers running parallel to the cylinder axis. Two endcaps close the barrel hermetically. Each of them consists of 32 "C" shaped modules arranged vertically along the chords of the circle inscribed in the barrel (see Fig. 1.2). In the endcap modules fibers run perpendicular to the cylinder axis, so that for the whole ECAL fibers are mostly transverse to the particle trajectories.

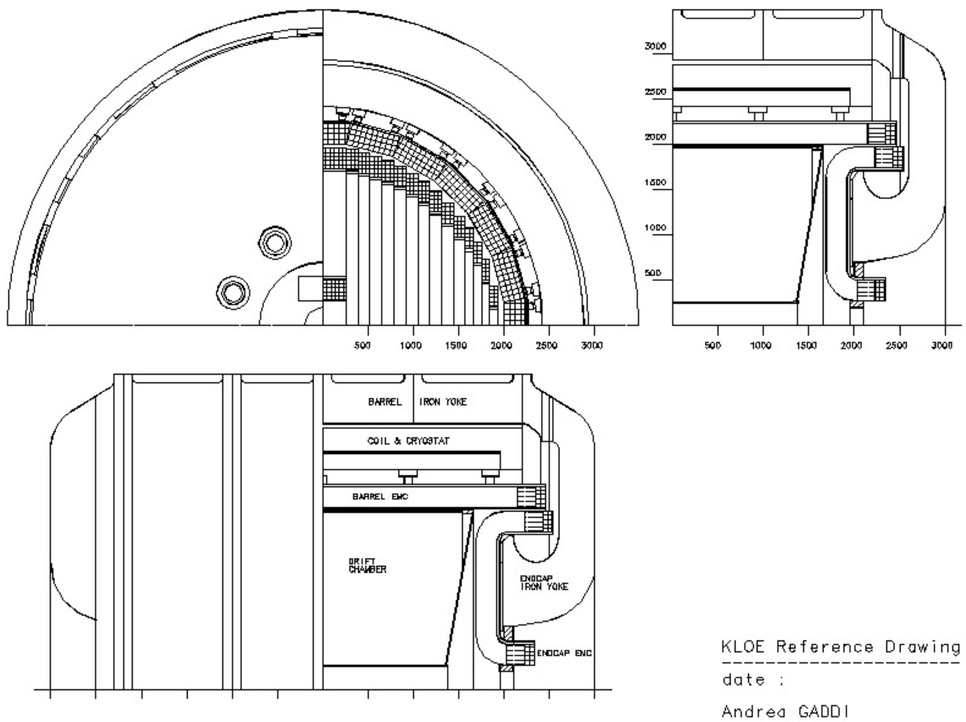

Figure 1.2: KLOE ECAL Schematic View.

The modules are read out on the two sides through Plexiglas light guides optically coupled to fine mesh PMTs. The readout granularity is $\sim 4.4 \times 4.4$ cm^2. Each barrel module has 60 channels per side while endcap modules have 10, 15 or 30 channels per side depending on their width. The total number of readout channels is 4880. Both in the barrel and in the endcaps, PMT axes are almost parallel to the magnetic field, in order to decrease the field effects on PMT response, and to increase hermeticity (see Fig. 1.2).

The basic calorimeter structure consists of an alternating stack of 1 mm scintillating fiber layers glued between thin grooved lead foils, obtained by passing 0.5 mm thick lead foils through rollers of a proper shape. The grooves in the two sides of each foil are displaced half a pitch, so that fibers are located at the comers of adjacent, quasi-equilateral triangles, resulting in an optimal and uniform arrangement of the fibers in the stack. The final composite has a fiber : lead : glue volume ratio of approximately 48 : 42 : 10, a density of ~ 5 g/cm^3 and a radiation length X_0 of ~ 1.6 cm, is self-supporting and can be easily machined. The energy sampling fraction is $\sim 18\%$ for a minimum ionizing particle (MIP) and the efficiency for low energy photons is high due to the very small lead foil thickness ($< 0.1\ X_0$).

1.2.1.1 Scintillating Fibers

Two types of fibers (Kuraray SCSF-813 and Pol.Hi.Tech. 0046) with a total length of 15,000 km have been used to assembly the ECAL. The former have higher light output and longer attenuation length, the latter are less expensive. Anyway the performance differences are not significant and the Kuraray fibers are used in the inner half of the calorimeter. All fibers have an attenuation length between 3 and 5 m and produce ~ 1 photoelectron for 1 mm of crossed fiber at a distance of 2 m from PMT. The emitted light is in the blue-green region ($\lambda_{peak} \sim 460$ nm).

1.2.1.2 Photomultipliers (PMTs)

The PMTs must operate in a magnetic field with the suitable efficiency, linearity, timing resolution and dynamical range. The Hamamatsu R5946/01 1.5' tubes [18] have been chosen because the electron multiplication occurs between dynodes made of fine mesh, very close to each other. Then the effect of the magnetic field on the electron path is very small. Furthermore housing boxes with double mu-metal shielding reduce the field to less than 0.2 T and the PMT alignment is such that the component transverse to the tube axis is less than 0.07 T. It has been measured that the PMT gain decreases by 10% when the field is on, but linearity and resolution are not affected.
The PMTs are operated with grounded cathodes in order to eliminate leakages, possible origin of noise and field distortions. A thin aluminum cylinder holds each PMT mechanically in place and a spring pushes gently it against the light guide. The optical contact PMT-light guide is made by means of Bicron optical gel BC-630.
insert here KLOE base description
The cables are in the box and carry high and low voltage, a test pulse and the output signal.

1.2.1.3 SiPMs as Possible Spare for PMTs

The SiPMs work efficiently in a range compatible with the typical wavelength-shifted light of the scintillating fibers, and are insensitive to magnetic fields, unlike PMTs. In addition, since SiPMs operate at low voltage, the high voltage power supply would no longer be required, with convenience in compactness and cost.
For the aforementioned reasons, the substitution of SiPMs with PMTs in the SAND calorimeter, with a possible improvement of efficiency and timing resolution, has been investigated [19]. The SiPMs used in this test are the 4×4 arrays of the Hamamatsu S13361-3050 series. Anyway, it is excluded to substitute the single PMT channel with 16 readout channels. Thus, in these measurements, the SiPM array is considered as a unique element. The MPPC series has been chosen since it achieves the maximum Photo-Detection Efficiency (PDE$_{MAX}$) close to the peak wavelength of the scintillating fibers (typically PDE$_{MAX} = 40\%$ at $\lambda = 450$ nm). But the quantum efficiency of the Hamamatsu R5946 1.5' mesh photomultiplier presently used in the calorimeter is 23% at $\lambda = 390$ nm.

A block ($24.5 \times 13.5 \times 40$ cm^3) of the lead-scintillating fiber calorimeter has been equipped (Fig. 1.3) with light guides like in KLOE. These light guides are shaped to cover the PMT surface and are not optimal for the smaller SiPM surface. Excluding the option to remove the present light guides and to mount new ones in the calorimeter, the test has been performed gluing a small adapter on the light guide to optimize the coupling with the SiPM (Fig. 1.3, right).

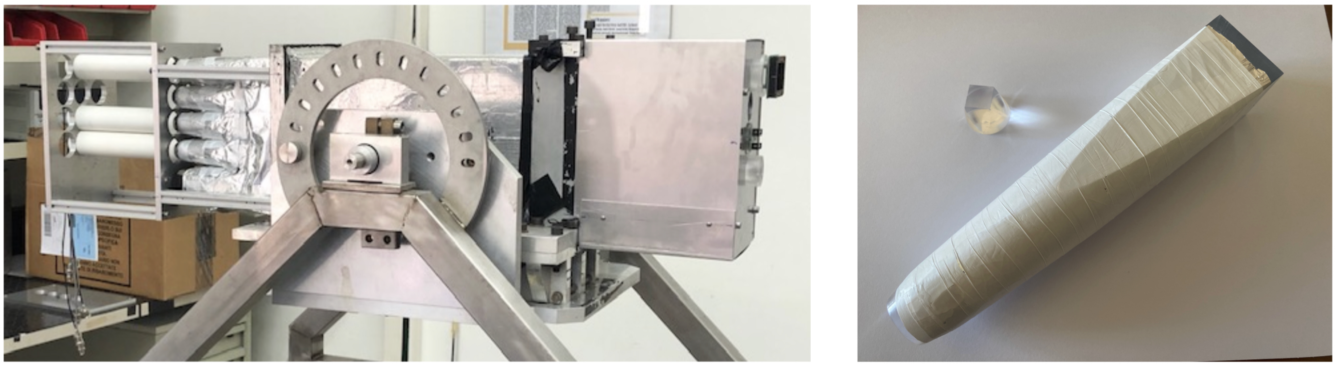

Figure 1.3: Left: experimental setup to compare PMT and SiPM. The SiPMs are on the right, the calorimeter block is at the center, the PMTs are on the left. Right: light guide and adapter for SiPM.

The signals induced by cosmic muons have been collected on one side by SiPM and on the opposite one by standard KLOE PMT. This setup allowed to compare directly the different performance. The measurements were performed for two SiPMs and two PMTs. The average results for efficiency and timing resolution in these conditions are reported in Table 1.1. Even if the differences are small, PMTs perform better in the present setup. The difficulties in coupling SiPMs with the light guides without deep mechanical changes, the lack of improvement, the cost, and the necessary commissioning time advise against the substitution of 4880 available and tested PMTs with new SiPMs. Nevertheless, the results from this study do not exclude the use of SiPMs as a spare. A mechanical setup is under study.

Table 1.1: Comparison of SiPM performance with PMT ones

	Efficiency (%)	Time Resolution (ps)
PMT	91.6 ± 0.2	197 ± 4
SiPM	90.8 ± 0.3	240 ± 3

1.2.2 Performance in KLOE and KLOE-2 Experiments

1.2.3 Requirements for DUNE Near detector (ND)

1.2.4 ECAL Calibration and Monitor System

Ideas to calibrate SAND ECAL according to KLOE experience
Cosmic muon detection with a dedicated trigger (no beam time)

1.2.5 ECAL Electronics

The neutrino interactions inside the SAND detector have to be identified by reconstructing the particles in the final state of the various processes. In particular, when these particles reach the ECAL modules, the signals of both sides of the hit cells are readout and converted by the ECAL electronics digital counts for time and amplitude. From this information the energy releases into the hit cells, their times and positions are derived [3]. In order to perform an optimal conversion, the front-end electronics should match the physical requirements in terms of dynamical range of the PMT signals and minimization of their pile-up. This is particularly relevant for SAND, as the ECAL PMTs and their associated electronics were optimized to work in the conditions of the KLOE experiment, different from those in SAND. A comparative study of the physical requirements in SAND and the characteristics of the existing front-end electronics is therefore important for the final choice of the SAND readout electronics.

1.2.5.1 Studies for the Optimization of the PMT Working Point

PMT saturation and measurement range
picoTDC
custom board

1.2.5.2 Frontend

1.2.5.3 Data acquisition (DAQ)

1.2.5.4 High-voltage

The Hamamatsu R5946/01 PMTs requires a maximum supply power of 2.3 kV, absorbing an average anode current of 0.01 mA. The CAEN SY4527 mainframe is capable of hosting up to 16 high voltage (HV) A7030P modules suitable for powering the ECAL PMTs. The CAEN A7030P is a module able to independently control up to 48 channels, with an output range of 3 kV/1 mA (1.5 W) at a low ripple (<20 mVpp-max in the range 10 ÷ 1000 Hz and <10 mVpp-max over 1000 Hz). The A7030P module is supplied with a high density multipin Radiall 691803004 connector. This connector is inadequate for powering the ECAL PMTs, therefore a multipin to SHV adapter will be used. The CAEN R648 19" rack module fits one Radiall 691803004-type multipin connector into 48 Radiall R317580-type SHV connectors, suitable for powering the ECAL PMTs. Moreover this module provides Interlock and Shield connections (through LEMO connectors). The described system includes a complete set of software tools for remote control (*via* Gigabit Ethernet or Wi-Fi) of both the mainframe and the high voltage boards, from low-level libraries to graphical application software. Furthermore a proprietary software introduces easy logging capability to the system. Through this tool it is possible to records every command sent to the system and every warning/alarm detected by the system. In this way it is possible to automatically monitor the behavior of every single parameter during operations.

Powering 4800 PMTs requires 100 CAEN A7030P HV modules that will be host in 7 CAEN SY4527 mainframes. In addition, 100 CAEN R648 Radiall to SHV connector adapters will be used to transfer HV power from HV module to PMTs. The unused mainframe slots can be used to save HV spare modules (Fig. 1.4).

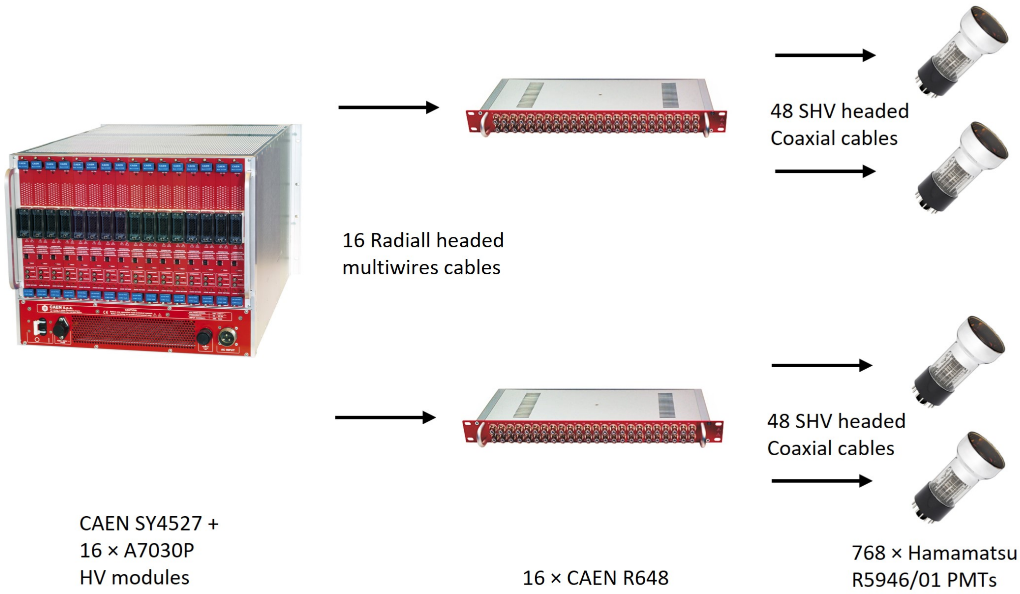

Figure 1.4: HV system to power 768 ECAL PMTs. In order to power all the PMTs, 7 of these systems are required.

1.2.5.5 Low-voltage

Each preamplifier on a PMT base is supplied with ±6 V and has a power consumption of 60 mW. Few CAEN A2551 boards, each with 8 full floating channels 8 V/12 A, are sufficient to power all 4880 PMT bases. The output voltage range is $0 \div 8$ V, with 0.2 mV monitor resolution (connector and sense voltages). The maximum output current is 12 A with 500 μA monitor resolution. The maximum channel power is 60 W. These boards can be host in the same CAEN SY4527 mainframes used for HV.

1.2.6 ECAL Dismounting Procedures

The first step to dismount the KLOE detector was the removal of cables, racks and other stuff in the experimental hall. A huge quantity of cables were unplugged from the calorimeter and the ancillary devices. Only signal and HV cables were stored to be reused at Fermi National Accelerator Laboratory (Fermilab). Twelve boxes were filled with 4880 signal cables and 4880 HV ones. Both the types of cables are 15 m long. From the six platforms aside KLOE 32 FEE+HV racks, 150 crates, and 3000 boards were removed.
The extraction of the Drift Chamber (DC) was the second step. Event though it will not be reused at Fermilab, the extraction was very careful because it will be displayed in the Laboratori Nazionali di Frascati (LNF) exhibition area. The DC structure is made of carbon fibers, the spherical endplates (EPs) are kept apart by 12 rods, and an external ring is coupled to each EP through 48 screws, to allow the recovery of the EP deformation under the wire tension load. The gas sealing of the chamber is ensured by the inner cylinder and 12 panels. About 60.000 wires are tensioned between the EPs, each of which is crimped on the copper feed through. The chamber extraction procedure has been thought considering several aims: to preserve the DC integrity, to avoid the wire breaking, and to ensure the safety of people.
The extraction of the DC was based on the insertion of a beam (Fig. 1.5, right) on the axis of the

cylindrical chamber, its clamping on the endplates and the extraction of beam and chamber as a unique piece. More in detail, at the beginning the beams (HEA200, 6 and 5 m long) were placed on 3 reinforced concrete pillars. Then the 6-m beam was inserted inside the DC. The beam and the DC were lifted up of few millimeters by means of the crane. This was enough to unload the DC weight from the static supports inside the calorimeter. A system with trolleys, suitably positioned on the endplates, allowed the DC to slide along the beam. Once the chamber was extracted from the calorimeter (Fig. 1.5, left), it was lifted, with a suitable sling bar, and placed on a handling trolley placed at the entrance of the experimental hall. Then it was ready to be taken away.

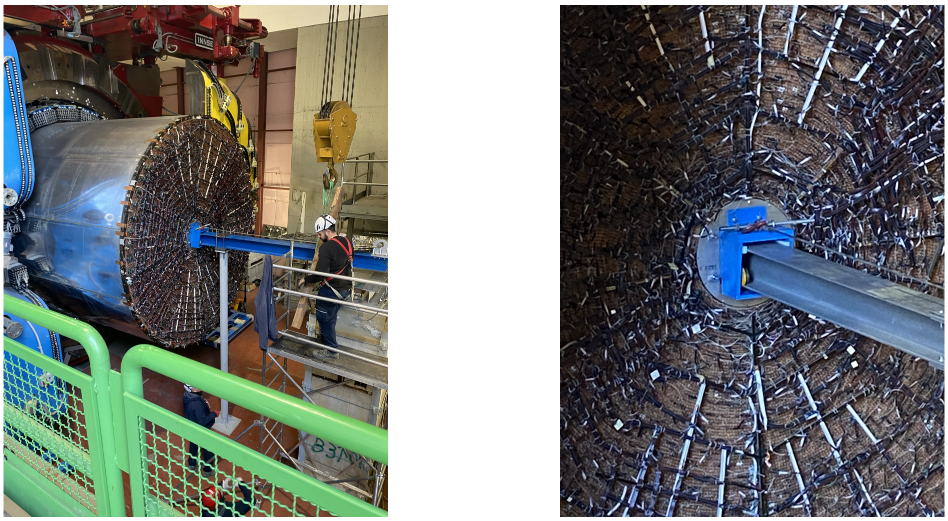

Figure 1.5: Left: extraction of the drift chamber at LNF. Right: zoom on the HEA200 beam and the trolley (detail in the text).

The dismounting of the modules of the calorimeter barrel required the construction of proper tools. These tools will be useful also in the mounting of SAND at Fermilab...

Figure 1.6: Movable platform for barrel modules extraction at LNF.

Figure 1.7: Extraction tool for barrel modules.

Figure 1.8: Extraction of the first barrel module from magnet cryostat.

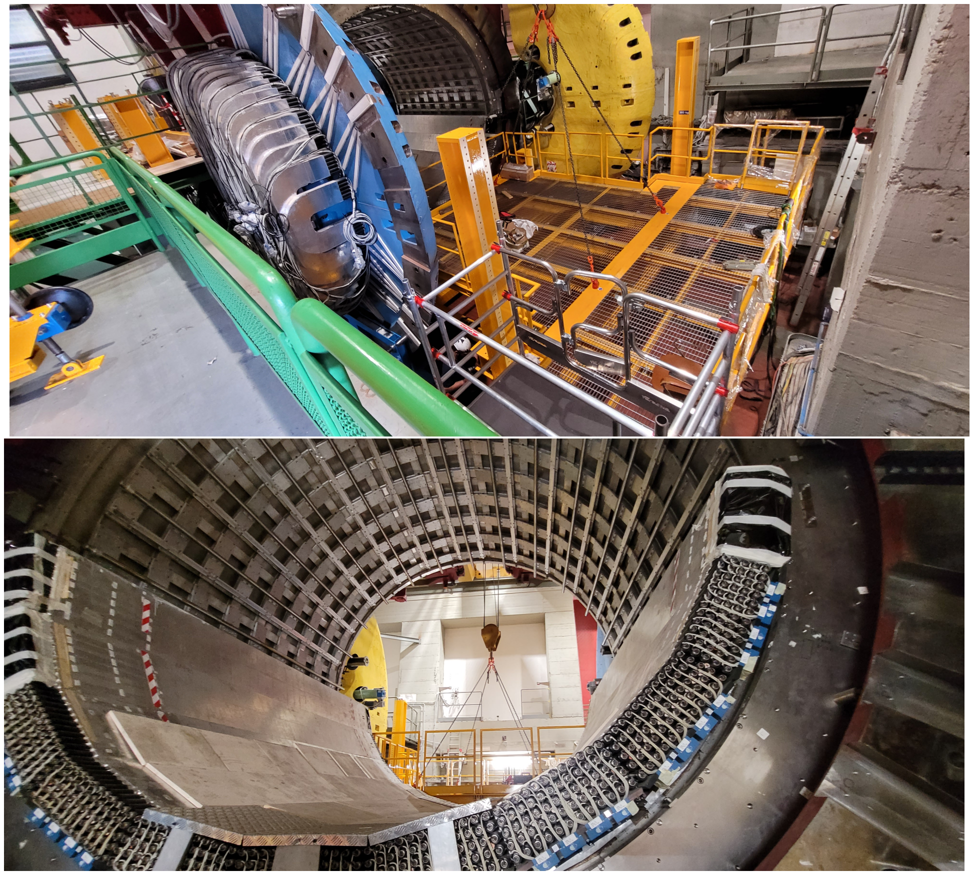

Figure 1.9: Progress of operations at LNF for the extraction of barrel modules from magnet cryostat.

Figure 1.10: Test area for ECAL modules at LNF.

1.2.6.1 Barrel Modules

1.2.6.2 Endcap Modules

1.2.7 ECAL Revamping and Test before SAND Installation

1.2.7.1 Module Tape Re-wrapping

1.2.7.2 Light Tightness and Tests with Cosmic Rays

1.2.8 ECAL Installation & Integration

1.2.8.1 Packaging and Shipping

1.2.8.2 Storage at Fermilab

1.2.8.3 Mounting in the ND Hall

1.2.8.4 Cabling in the Alcove

1.2.9 Commissioning

1.2.10 Schedule and Milestones

1.3 The Superconducting Magnet

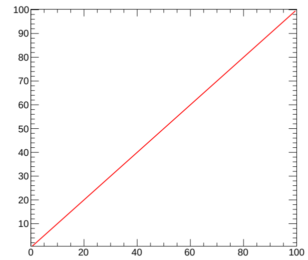

Figure 1.11: Dummy - Here insert the caption.

1.3.1 Magnet Specification

- Experimental requirements ...
- Coil parameters (operation current, stored energy ...)
- Nominal magnetic field map ...

1.3.2 Magnet Maintenance and Revamping Options

- Status
- Subsystems and components maintenance
- Obsolete or aged subsystems and components to be replaced
- New power supply (CAEN ELS)
- Power Electronics (OCEM)
- Quench detector (?)
- Control system

1.3.3 Activities at LNF

- Procurement of the cryogenic systems and materials for magnet cool down
- Magnet full operational test (full support for test/dismount/remount by ASG ?)
- Coil cool-down
- Magnet energizing test
- Coil Cryostat extraction
- Magnet turret removal
- Dismounting of Iron Yoke
- Tools, Packaging & Shipping to Fermilab

1.3.4 Installation & Integration at Fermilab

- details about the storage at Fermilab ...
- tools and mounting procedure ...
- switch-on test at Fermilab ...
- commissioning in the alcove ...
- cryogenic refrigeration plant for continuous operation of the magnet

- risk management ...
- schedule and milestones ...

1.4 Liquid argon (LAr) Active Target (GRAIN)

1.4.1 Introduction and Physics Requirements

goals for enhancing SAND capability
general requirements for neutrino event reconstruction (tracking, calorimetry, event identification)
general description of the geometry and optical detectors

GRAIN might be fundamental for providing inclusive and exclusive Ar interactions for the nuclear effect studies as well as a complementary Ar target for cross-calibration with the other DUNE Near Detector components which will be off-axis for 50% of the total time. For this purpose a high precision reconstruction of the neutrino interaction in GRAIN is crucial for the oscillation program. In particular, since low energy particles are stopped in LAr volume or in the GRAIN cryostat, as well as particles exiting at high angles with respect to the beam direction are therefore excluded by the STT acceptance, a potentially wrong topological reconstruction and a bias in the energy reconstruction can occur and it can be only compensated by instrumenting the LAr volume. In the current design, in order to collect scintillation light for reconstructing charged particle tracks emitted from neutrino interaction events, GRAIN will be instrumented with innovative detectors made by SiPM matrices coupled with optical systems. On one hand, the light readout in GRAIN will provide information about the time of the event and the calorimetric measurement of the total energy deposited in the LAr volume, on the other hand, if the optical system will be effective, the acquired images could provide additional information about the number of tracks of primary or secondary particles, the particle identification and vertex position of the neutrino interaction allowing us to reconstruct with a very high accuracy neutrino interactions in GRAIN.

1.4.2 Mechanical Design

As depicted in Figure 1.12, the GRAIN cryostat consists of an Internal Vessel placed within an External Vessel, both possessing an elliptical transverse shape. The Internal Vessel is constructed from Stainless Steel (AISI 316L) and comprises a main body with a 6 mm wall thickness and two 30 mm-thick Endcaps. The elliptical base axes measure 147 cm $\times$ 47 cm, and the main body's height is 150 cm. Within the Internal Vessel, approximately 1 ton of LAr is contained. The imaging detectors (such as lenses and masks) are affixed to frames on both Endcaps and along two rails at the Top and Bottom of the main body. Each Endcap features 4 flanges equipped with feedthroughs for signals and detector power. The mechanical design aims to minimize the material budget transverse to the beam axis. The increased thickness of the two Endcaps is essential for effective sealing under cryogenic conditions using Helicoflex seals.

The thermal insulation of the Internal Vessel relies on the vacuum created by the External Vessel. The External Vessel, operating at room temperature and having fewer mechanical requirements, will be constructed using a composite structure. This composite consists of a 40 mm honeycomb layer (made of Al alloy) sandwiched between two 6 mm Carbon Fiber layers. While the composite material will be used exclusively for the Main body, the two endcaps will be made from Aluminum. The design of the external vessel is also optimized to minimize the material budget seen by the beam. Both endcaps will feature the same number of flanges as the Internal Vessel, facilitating the transmission of signals and detector power.

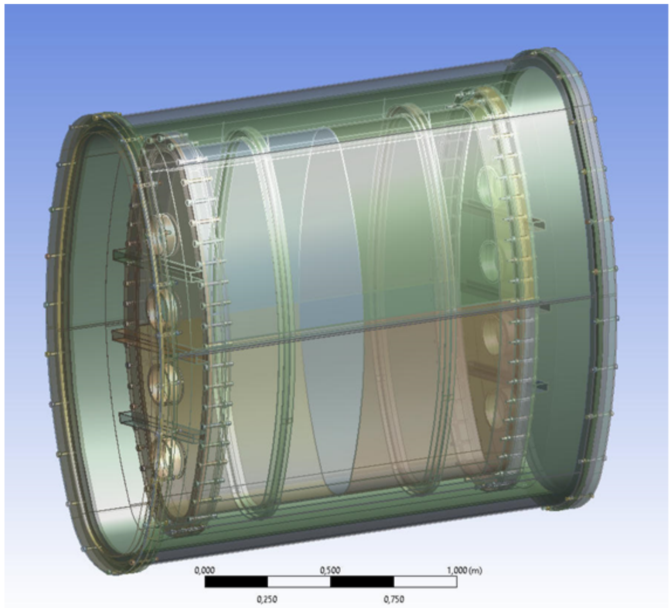

Figure 1.12: GRAIN cryostat

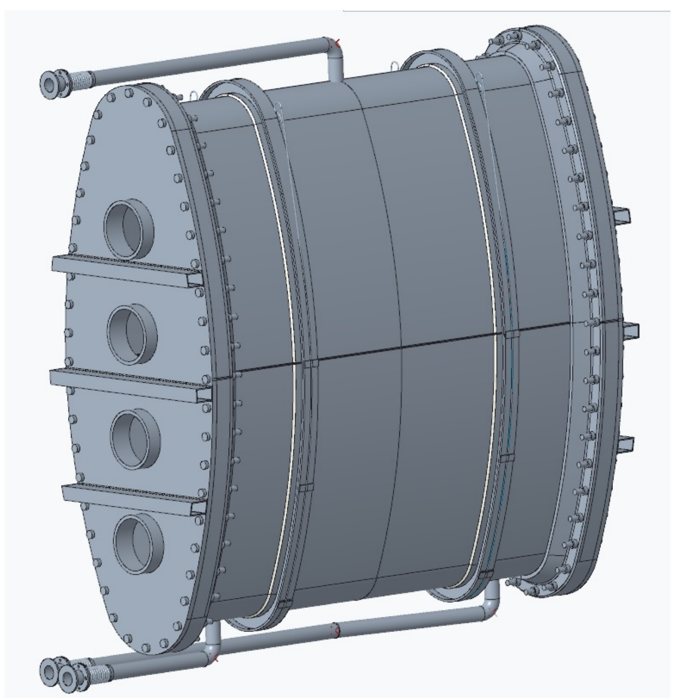

Figure 1.13: GRAIN internal vessel

1.4.3 Optical Detector

Optical systems are necessary for collecting and possibly focusing photons from Argon scintillation in order to image tracks and vertexes from neutrino interactions.

Currently two technologies for the optical detectors are being evaluated for their use in GRAIN, based either on UV lenses or on coded apertures.

- **UV lenses:** lenses are traditional imaging systems, but their use for LAr scintillation light (VUV) poses some challenges related to material properties (transmittance, index of refraction) and to the choice of the main optical parameters. Currently different materials are under test, some of these have high transmittance only at wavelength higher than 180 nm. In this case the usage of Xenon doping for shifthing the 128 nm wavelength argon scintillation light is thus necessary.
- **Coded apertures:** this technique is the direct evolution of the pinhole camera, the simplest imaging device. A perforated mask is placed in front of the photo-detector. This optical system will form an image on the sensor plane from which one can extract the track parameters through iterative numerical algorithms. This is independent on the light wavelength, but it requires a large amount of collected light for a good reconstruction.

In both the two technologies based on UV lenses or coded apertures the impinging photons are acquired by matrices of SiPM, covering an area of 64×64 mm.

1.4.3.1 SiPM matrices

GRAIN will use SiPM matrices with pixel sizes ranging from 1x1 to 4×4 mm^2, with a cell size ranging from 30 to 50 μm. The baseline option for lens-based cameras will be a 32×32 matrix, with SiPM dimension of 2×2 mm^2. Currently the Hamamatsu S13361-2050 8×8 matrix is commercially available, which has fill factor of 75%, cell pitch of 50 μm, PDE of 40% at 450 nm [**?**]. In this case 16 matrices could be employed for achieving the 32×32 channels configuration. For the lens-based system an alternative solution which might improve the final resolution on the spatial reconstruction is to use a matrix of 64×64 channels of 1×1 mm^2 each. In this case the 16×16 Hamamatsu S13615-1050N-16 matrix can be considered, which has fill factor of 74%, cell pitch of 50 μm, PDE of 50% at 450 nm [**?**]. Again 4 matrices might be employed for achieving the 64×64 configuration, but now the number of channels will increase of a factor 4 with respect to 2 mm configuration.
For the coded aperture based detector the baseline option is a 32×32 matrix with SiPM dimension of 3×3 mm^2 provided by e.g. 16 matrices Hamamatsu S14161-3050HS-08 (fill factor of 74%, cell pitch of 50 μm and PDE of 50%). However currently also the option to use matrices with 4×4 mm^2 is under evaluation and must be considered as well for the application-specific integrated circuit (ASIC) design.
Properties of representative SiPMs from Hamamatsu are shown in the table 1.2, where the terminal capacitance assumes lower value for smaller SiPM dimensions.

Finally the Single Photon Timing Resolution (SPTR) which represents the timing jitter measured when one photo-electron is detected by the photodetector, will be responsible of the final time accuracy. If the cell dimension is in the 30-50 μm as in our case, the SPTR is expected to be less

Table 1.2: Properties of representative SiPMs from Hamamatsu.

Parameter	Minimum	Maximum
Terminal Capacitance	40 pF	900 pF
Gain	1×10^6	7×10^6
Bias	35 V	60 V
Warm Dark Current	-	3.3 μA

than 100 ps.

1.4.3.2 Lens-based Optical Detector

Working principle description...**GENOVA now**

Lenses have traditionally been used as imaging systems in countless camera applications. However, their use in a cryogenic liquid, such as argon, would be innovative since the choice of the material have to satisfy a series of requirements.

In particular the material must be compatible with the cryogenics environments, have a proper refraction index with respect to the LAr index and have a high transmittivity at the interesting light wavelenght.

If we consider the 127 nm LAr scintillation wavelength the only two materials commercially employed for the production of UV lenses are magnesium fluoride (MgF2) and calcium fluoride (CaF2). However, their use in a cryogenic environment has not been documented yet, posing questions on the mechanical and thermal stability of large lenses (up to 6 cm in diameter) with these materials.

Thus a possible solution for working at higher light wavelength would be doping LAr with a small amount (few tens of ppms) of xenon (Xe). It has been demonstrated that dissolving xenon in LAr can efficiently convert the VUV light from 127 nm to 174 nm, also slightly enhancing the light yield [67]. The energy transfer between the argon excimers and xenon is quick ($\sim$ 1 ns) [68], so no degradation of space resolution occur. An efficient imaging system based on lenses would therefore be possible with Xe-doping: the photodetector PDE is 10% higher at 174 nm and also more common materials, such as fused silica, become suitable. The only downside to adding Xe is the change in the time distribution of the shifted emission: the fast component (6 ns) is not affected and remains at 127 nm, possibly also suppressed, while the slow component is shortened up to a few hundred ns (160 ns at 25 ppm) [70].

For design a lens-based optical system the refractive indexes of the different material have to be considered.

For what concerns LAr refractive index the uncertainty in the UV range is quite high. The refractive index at 127 nm can be calculated using the Sellmeier equation,having fitted the coefficients with historical datasets in the visible range. These calculations predict a value between 1.35 and 1.45 [71]. More recently, from a measurement of the group velocity at 127 nm the refractive index is reported as $n = 1.358 \pm 0.003$ [72], while the extrapolated value at 174 nm is around 1.26 (see

Fig. 4.7).

Since typical VUV transparent materials or silica glass have a refractive index around 1.3-1.4, very similar values to the LAr value, a normal bi-convex lens with spherical surfaces will not be usable for achieving the desired focal length.

Thus the lens design is based on a gas volume enclosed between two surfaces, which having a refractive index close to LAr medium does not influence the optical system, which is dominated by the LAr-gas index difference.

Thus the optical design is shown in the picture 1.14

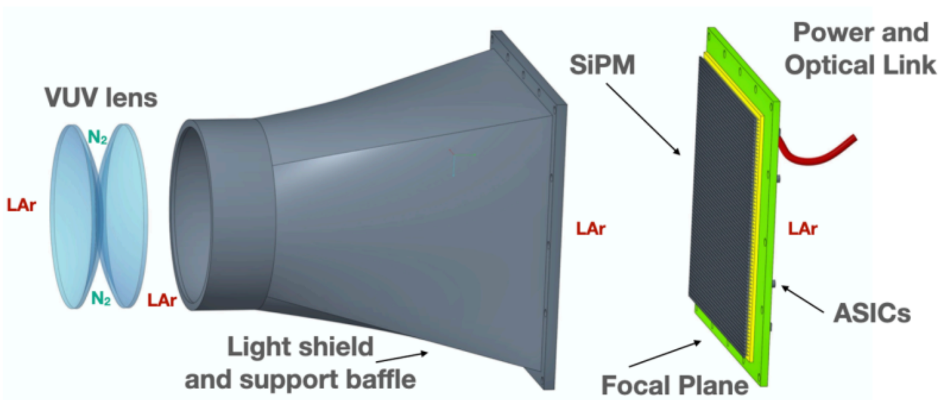

Figure 1.14: Exploded view of the lens-based camera components: the lenses, the light shield, SiPMs matrix on a supporting PCB.

It consists of four elements: the optical lens system, the light shield, the SiPM matrix and the front-end electronics.

1.4.3.3 Coded Mask Detector

Working principle description [20]...**BOLOGNA now**

1.4.3.4 Detector Layout in GRAIN

1.4.3.5 First Results with Detector Prototypes

1.4.4 Electronics

ASIC requirements and design...(**now from ASIC document**)

The main ASIC requirements are guided by the detector layout and by the needs for the physic reach of SAND. Accurate tracking and high precision reconstruction capability in GRAIN requires a reasonably precise measurement of the amount of light detected by each pixel. In addition, for increasing the physics reach, for distinguish tracks coming from different interactions within the same spill interval, precision on the measurement of the time of arrival of photons is also required. Thus ASIC should be able to provide a precise information on the number of photons detected from

each interaction and on the time of arrival of the first photon coming from the same interaction. The ASIC must be able to function at both cryogenic and room temperature, considering both its own operating parameters and the increase in SiPM current. It is possible to rely on externally controlled parameters to ensure this versatility. A consistent behaviour of the analog front end over the entire temperature range is desirable.
The exact number of cameras that will be required is not yet known, but an estimate of 50 $\pm$ 20 is realistic and it is currently under study. It is assumed that the ASICs will have 1024 channels and that it will be mounted in close proximity to the sensors, most likely on the opposite side of the same PCB. A 1024 channels ASIC which is optimal for a sensor of 32×32 SiPM or eventually for a more dense SiPM of 64×64 channels. The requirements on power consumption and data throughput consider 50k channels as baseline. It is important to note that the beam structure is characterized by an extremely low duty cycle (10 μs spill, nearly 1 s interspill). While one may want to also occasionally collect off-beam data for acquiring cosmic events for calibration and background studies, a duty cycle limitation can be accepted if it is necessary to meet the other requirements related to power consumption and data throughput.

The ASIC analog front-end must be able to adapt to all capacitance values in the range shown in the table 1.2 in the section before, if possible with some margin towards higher values. If adjustable values of internal parameters are necessary to accommodate the different SiPMs, it is sufficient to have a single, chip-wide, setting.

The ASIC must provide information that allows to accurately count photons of the fast and the slow component, but it must do it in such a way that distinguishing two overlapping events remains possible, and that the arrival time information remains available. This requirement excludes the trivial solution of simply using a very long shaping time to integrate the charge of both components. To this goal the SiPM waveform and especially the decay time constant have to be optimized with the ASIC architecture: while for the rising time of the signal a typical value of less than 1 ns is acceptable, the decay time has to be carefully optimized since it influences the behaviour of the final signal if more photons arrive in a short time scale (1-100 ns).

Each ASIC channel must be capable of counting photons that arrive with a proper time distribution It must therefore be able to both distinguish separate pulses, and to provide an amplitude information of the individual pulses. It must also provide timing information on the leading edge with a precision better than 100ps. Offline data analysis will then be able to distinguish a distribution containing one signal from one containing overlapping signals. It is understood that the definition of "separate" pulses depends in practice on the fall time of the waveform, and that this parameter can be adjusted in the analog front end. In order to satisfy the original goal of distinguishing overlapping neutrino events, the ASIC must be capable of separating pulses whose photons are more than O(100 ns) apart. Considering both the error on the amplitude measurement, and the occasional miscounting of nearby pulses, the ASIC should allow to determine the total number of photons in a pulse with an error lower than 5% (assuming the identification of separate overlapping events is perfect).

In conclusion, assuming a 1024 channel ASIC detailed study are necessary for:

- estimating the achievable precision on the number of detected photons with a signal to noise ratio bigger than 10

- estimating the achievable precision on the time of arrival of a single photon and on a bunch of photons whose signal generated by SiPM is overlapping in time
- estimating and optimizing the power consumption, taking into account the power gating possibility

1.4.5 Data Acquisition and Slow Control System

1.4.6 Neutrino Event Reconstruction

1.4.6.1 Algorithms for Track Reconstruction with Lens Images

Multiple-View Geometry and the reconstruction task In this Section we will discuss the reconstruction of 3D light sources in GRAIN, starting from a certain number of 2D images acquired by the optical sensors available in it. We will discuss this problem under rather ideal conditions, avoiding dealing with the many detailed aspects that a realistic model would require. But, at the same time we will try to highlight what restrictions exist in the discussion. The method is based on the approximation of geometric optics, obviously ignoring the diffraction of light, but also other important physical effects, such as the existence of a finite field of view, a focal distance of a coded mask or the thickness of the lens.

Although the topic has been extensively covered in several manuals (see for example [21]), the application and the extension of the techniques mentioned to the specific experimental contexts of GRAIN requires further investigation.

For GRAIN several arrangements and numbers of cameras have been proposed, possibly of different types (lenses and masks), located in various positions and differently oriented. Thus, at least up the validity of the projective approximation, one has a set of matrices $\{P_\alpha\}$ describing the whole optical detectors. Each of them provides an image of the same sources, namely the indexed sets of points $\{\mathbf{x}_{\alpha\, i}\}_{i\in\mathcal{I}_\alpha} \subset \mathbb{P}^2$, the reconstruction task means to determine the values of the unknown source points $\{\mathbf{X}_{\ i}\}_{i\in\mathcal{I}_s}$ by a suitable algorithm.

In the simulations performed up to now, the coordinates of the image points $\mathbf{x}_{\alpha\, i}$ are taken by clustering the signals on the detectors and evaluating their centroids (see for instance [20]).

The camera projective matrix The main mathematical object describing a general projective camera is the matrix P, which maps 3D world points $\mathbf{X}$ to 2D image points $\mathbf{x}$ in homogeneous coordinates, accordingly to

$$P : \mathbb{P}^3 \to \mathbb{P}^2, \quad \lambda\, \mathbf{x} = P\mathbf{X}, \quad \lambda \in \mathbb{R}_{/0},\ \mathbf{x} = \begin{pmatrix} x_1 \\ x_2 \\ x_0 \end{pmatrix},\ \mathbf{X} = \begin{pmatrix} X_1 \\ X_2 \\ X_3 \\ X_0 \end{pmatrix}. \tag{1.1}$$

Due to the above physical settings, we consider only non-affine projective cameras, described by the block decomposition

$$P = K\,[R|\mathbf{t}] = K\ R\ [\mathbb{I}| - \mathbf{c}]\,, \tag{1.2}$$

where $[\cdot|\cdot]$ is a short notation for a 3×4 matrix with a column 3 component vector as second argument, $R \in SO(3)$ is a rotation matrix, $\mathbb{I}$ is the 3D identity matrix, $\mathbf{t} \in \mathbb{R}^3$, K is called the *calibration matrix* and it can be always set in the form

$$K = \begin{pmatrix} \alpha & s & x_0 \\ 0 & \beta & y_0 \\ 0 & 0 & 1 \end{pmatrix}. \tag{1.3}$$

where α and β are the focal lengths along x and y axis, respectively, s is the skew parameter and $(x_0, y_0)^T$ is the principal point on the image plane, not necessarily coincident with axis origin on it. The normalization $K_{33} = 1$ can be imposed because of the non affinity condition.

The *camera center* $\mathbf{C}$ is defined by $P\,\mathbf{C} = 0$, then one has

$$\mathbf{C} = (\mathbf{c},\ 1)^T = \left(-R^T\,\mathbf{t},\ 1\right)^T. \tag{1.4}$$

The calibration of lenses and coded masks Although the design concept defines the camera matrices P_α, one should take it into account a stage of *calibration* of the apparatus, when the positioning of the cameras may be affected by modifications, errors and inaccuracies in the assembly of the apparatus. Particular attention must be paid in the case of sensors based on the coded mask technology, since they are not centered optical systems. Then, all the parameters involved in in the calibration matrix K may result different from 0 and the focal lengths unequal. Furthermore, in this case the projection matrix represents a rather crude approximation of a coded mask optical system, valid only for sources close to the focal plane and is also difficult to calculate starting from the mask itself.

The procedure of calibration of the camera indexed α proceeds from the knowledge of $\mathcal{I}_s$ sources and the corresponding image points $\{\mathbf{X}_i \Leftrightarrow \mathbf{x}_{\alpha\, i}\}_{1 \le i \le \mathcal{I}_s}$. Then, one can determine the projection matrix P_α from the definition (1.1) and the consequent identity $\mathbf{x}_{\alpha\, i} \wedge P_\alpha\, \mathbf{X}_i = \mathbf{0}$, leading to the over-determined system

$$A\,\mathcal{P} = 0, \quad \mathcal{P} = \left(P_\alpha^1, P_\alpha^2, P_\alpha^3\right)^T \tag{1.5}$$

where P_α^j denotes the rows of the unknown matrix P_α and the $12 \times \mathcal{I}_s$ matrix A is obtained by replicating for $i = 1, \ldots, \mathcal{I}_s$ the first two rows (for instance) of the previous identity.

In order to have a non trivial solution one must have $\operatorname{rank}(A) = 11$, implying a number of sources $\mathcal{I}_s \ge 6$.

For a number of sources > 6, possibly affected by measurement errors, one obtains an optimal solution for P_α, by proceeding to a Singular Value Decomposition (SVD) of the matrix A [22]. This means that one has to take the smallest eigenvalue in the symmetric matrix $A^T A$, represented as the diagonal 12×12 matrix D of the decomposition $A = U\,D\,V^T$, and compute the corresponding column of the matrix V.

This naive procedure can be make more robust and numerically stable by several modern techniques (see the algorithms reported in [21]). However, with such a technique we were able to find the projection matrix for a mosaic of four coded masks 19×19, reproducing with a relative error of about 3% the image points obtained in the simulations.

3D Reconstruction of point-like sources by Double View: general formulas For two distinct cameras, described by matrices P_α and P_β, the formula (1.1) maps a source point $\mathbf{X}$ into the two image points, $\mathbf{x}_\alpha$ and $\mathbf{x}_\beta$, which will be called *corresponding* points and can be observed on the two image planes π_α and π_β respectively. The converse of the above observation is less obvious. In fact, given two *corresponding* image points $\mathbf{x}_\alpha$ and $\mathbf{x}_\beta$, one can provide the **reconstruction formula** for the unique source point $\mathbf{X}$ by

$$\mathbf{X} = P_\alpha^+ \mathbf{x}_\alpha - \frac{(P_\beta\, P_\alpha^+\, \mathbf{x}_\alpha \;\times\; \mathbf{x}_\beta)\cdot [\mathbf{e}_\beta]_\times \mathbf{x}_\beta}{|\, [\mathbf{e}_\beta]_\times\, \mathbf{x}_\beta|^2}\, \mathbf{C}_\alpha = P_\beta^+ \mathbf{x}_\beta - \frac{\left(P_\alpha\, P_\beta^+\, \mathbf{x}_\beta \;\times\; \mathbf{x}_\alpha\right)\cdot [\mathbf{e}_\alpha]_\times \mathbf{x}_\alpha}{|\, [\mathbf{e}_\alpha]_\times\, \mathbf{x}_\alpha|^2}\, \mathbf{C}_\beta, \quad (1.6)$$

where the short notation $[\mathbf{a}]_\times\, \mathbf{b} = \mathbf{a} \times \mathbf{b}$ has been used and, for each camera, the respective *epipoles* and the *pseudo-inverse* matrices have been introduced

$$\mathbf{e}_\beta = P_\beta\, \mathbf{C}_\alpha \in \pi_\beta, \qquad \mathbf{e}_\alpha = P_\alpha\, \mathbf{C}_\beta \in \pi_\alpha, \qquad P_\gamma^+ = P_\gamma^T \left(P_\gamma\, P_\gamma^T\right)^{-1} \qquad \gamma = \alpha, \beta. \quad (1.7)$$

It should be noted that the reconstruction formula is in general fractional quadratic in the image point coordinates. Some simplifications are possible for special configurations of the cameras.

For instance, in the case of front-to-front ideal lenses (purely diagonal camera matrices), for the transversal coordinates with respect to the common Z axis one obtains the simplified formulae

$$X_S = \frac{2c x_\alpha x_\beta}{f\,(x_\alpha + x_\beta)}, \quad Y_S = \frac{2c y_\alpha y_\beta}{f\,(y_\alpha + y_\beta)}, \quad Z_S = (c+f)\,\frac{z_\alpha - z_\beta}{z_\alpha + z_\beta}.$$

These formulas were used with quite good results in the work [20], in which a primitive model of GRAIN was simulated, equipped with optical sensors of the coded mask type.

Subsequently, when a realistic GRAIN model equipped with lenses was conceived, the same formulas allowed the concrete reliability of using the (1.6) reconstruction formulas to be verified on a sample of approximately 1000 point sources. In fact, by simulating the images recorded by the SiPM matrices for each source, all possible pairs of them were considered. The average of all these reconstructions was then calculated, obtaining a result that differed by a few % from the original position.

However, in this reconstruction procedure a critical aspect consists of the identification of the corresponding points, which did not arise in the simulations with single sources.

A solution to this problem is offered by the use of the so-called **fundamental matrix**, which we will examine in the next paragraph.

The Fundamental Matrix in Double View Let us suppose to have a rig of two cameras, say P_α and P_β their matrices, and on the respective image planes we find $\mathbf{x}_\alpha$ and $\mathbf{x}_\beta$ a pair of image points. These points are *corresponding*, in the sense of the previous paragraph, if the unknown $(\mathbf{X}, \lambda_\alpha, \lambda_\beta)$ solve the overdetermined system $P_\alpha \mathbf{X} - \lambda_\alpha\, \mathbf{x}_\alpha = 0, \quad P_\beta \mathbf{X} - \lambda_\beta\, \mathbf{x}_\beta = 0$. The compatibility condition is expressed in the form

$$\sum_{i\,j} x_{\alpha\, i}\, F^{\alpha\,\beta}_{i\,j}\, x_{\beta\, j} = \mathbf{x}_\alpha^T\, F^{\alpha\,\beta}\, \mathbf{x}_\beta = 0, \quad (1.8)$$

where the elements of the $\left(F^{\alpha\,\beta}_{ij}\right) = F^{\alpha\,\beta}$ matrix are given in terms of the camera matrices P_α and P_β. The basic relations for the fundamental matrix are

$$F^{\beta\,\alpha} = [\mathbf{e}_\beta]_\times \; P_\beta\, P^+_\alpha, \quad ; \quad F^{\beta\,\alpha\,T} = F^{\alpha\,\beta} = [\mathbf{e}_\alpha]_\times \; P_\alpha\, P^+_\beta; \quad \det\left[F^{\beta\,\alpha}\right] = 0. \tag{1.9}$$

The matrix $F_{\beta\,\alpha}$ is independent of the specific representations of the camera matrices, but it is defined only on their optical properties and relative geometrical properties. Thus, one concludes that for a pair of equally calibrated camera stereo rig, namely with $K_\alpha = K_\beta = K$ and with $\mathbf{t}$, R the relative translation/rotation, the following relations hold

$$F^{\alpha\beta} = [\mathbf{e}_\beta]_\times\, K\; R\; K^{-1} = K^{-T}\, [\mathbf{t}]_\times \; R\; K^{-1} = K^{-T}\; R\; \left[\right]R^T\; \mathbf{t}\Big]_\times \; K^{-1} = K^{-T}\; R\; K^T\, [\mathbf{e}_\alpha]_\times\,, \tag{1.10}$$

where, because of the projective character of the mapping, a global scalar factor is ignored. From the last relation in (1.9), the fundamental matrix is a rank $= 2$ linear mapping. There exists a one-dimensional left/right kernel of $F^{\alpha\,\beta}$. In fact, if $\mathbf{x}_\alpha \in \pi_\alpha$ is corresponding to $\mathbf{x}_\beta \in \pi_\beta$, then $(\mathbf{x}_\beta + \zeta_\beta\, \mathbf{e}_\beta)^T\; F^{\beta\,\alpha}\, (\mathbf{x}_\alpha + \zeta_\alpha\, \mathbf{e}_\alpha) = 0$ holds for all $\zeta_\alpha,\; \zeta_\beta \in \mathbb{R}$, then for each image point on π_α an whole image line is singled out on π_β.

In conclusion, if $F^{\alpha\beta}$ is known for a pair of cameras, then using the relation (1.8) one can verify that two image points are indeed corresponding, modulo translations in the epipolar direction. This provides a numerical criterion criterion, for checking the correspondence of image points, applied in the simulations we performed.

The computation of the matrix $F^{\alpha\beta}$ can be performed both by using (1.9) or (1.10), but also directly from the observed images. This is particularly useful, as may happen in several concrete situations, when the cameras are not or partially calibrated.

In fact, let us suppose to know a set of n corresponding image points pairs $S_c = \{(\mathbf{x}_{\alpha\,k},\; \mathbf{x}_{\beta\,k})\}_{k=1,\ldots,n}$. Thus, applying the compatibility equation (1.8) on the n pairs one obtains a linear homogeneous system of n equations in 9 variables of the form

$$\mathcal{A}\; \mathcal{F}^{\alpha\,\beta} = 0, \quad \mathcal{F}^{\alpha\,\beta} = \left(F^{\alpha\,\beta}_{11}, F^{\alpha\,\beta}_{12}, \ldots, F^{\alpha\,\beta}_{33}\right)^T, \quad \mathcal{A} = (\overline{\mathbf{x}_{\alpha\,i} \otimes \mathbf{x}_{\beta\,i}})_{i=1,\ldots,n}\,, \tag{1.11}$$

where the short notation $\overline{\mathbf{a} \otimes \mathbf{b}} = (a_1 b_1, a_1 b_2, a_1 b_3, \ldots, a_3 b_3)$ has been used, so that $\mathcal{A}$ is a $n \times 9$ matrix.

The existence of a non vanishing solution for $\mathcal{F}^{\alpha\,\beta}$ imposes $\det[\mathcal{A}] = 0$. This is equivalent to state that $\mathcal{F}^{\alpha\,\beta}$ is defined by a subset of at most 8 independent pairs of image points extracted from S_c. If this is true, then one says that $\mathrm{rank}\,[S_c] = \mathrm{rank}\,[\mathcal{A}] = 8$ and $\mathcal{F}^{\alpha\,\beta}$ can be computed from (1.11) modulo a scalar factor, irrelevant in the projective context.

However, if one is able to empirically find more than 8 pairs of corresponding points, eventually affected by measurement errors, the system (1.11) is over-determined and noisy. So, it may be more useful to develop a variational algorithm which implements the constrained minimization problem

$$\min_{\mathbb{R}^9} ||\mathcal{A}\; \mathcal{F}^{\alpha\,\beta}|| \quad \text{with } |\mathcal{F}^{\alpha\,\beta}| = 1. \tag{1.12}$$

Furthermore, one has to implement the singular constraint $\det F = 0$ seen in (1.9). Such a problem, treated by the SVD algorithm [22], has as solution the normalized eigenvector of $\mathcal{A}^T\mathcal{A}$ of its smallest non-vanishing eigenvalue. In its completeness, the algorithm requires $O(n^2)$ computational resources. Optimized algorithms can be found in [21].

Since this procedure is irrespective of the precise knowledge of the pair of projection matrices, it can be applied to perform a **F matrix calibration** directly on the experimental set up.

Examples of a fundamental matrix The simplest case is a finite set of identical and parallel cameras located on the same plane. Thus the set of the projection matrices and the fundamental matrices for each pair of distinct cameras are

$$P_{ij} = K\,\left[\mathbb{I}| - \mathbf{c}^{i,\,j}\right] \quad \text{for}\;\; i = 1, \ldots, N_x,\; i = 1, \ldots, N_y, \quad F^{kl,\,ij} = \left[K\left(\mathbf{c}^{i,\,j} - \mathbf{c}^{k,\,l}\right)\right]_\times \tag{1.13}$$

being the epipoles $\mathbf{e}^{kl,\,ij} = K\left(\mathbf{c}^{i,\,j} - \mathbf{c}^{k,\,l}\right)$ located at infinity in the common image plane, because of the vanishing their third component. Because of the geometric restrictions only $N_xN_y - 1$ matrices are independent and the symmetry relations hold

$$F^{kl,\,ij} - F^{hm,\,ij} = F^{kl,\,hm}, \quad F^{ij,\,kl} = -F^{kl,\,ij}, \tag{1.14}$$

significantly reducing the computational complexity.

Pairs of corresponding points lie along parallel lines to the epipole ones, common to all image planes. These are parallel also to the lines connecting the camera centers if the skew parameter s is vanishing.

The above observation provides a quite useful criterion in selecting two different images the possible corresponding points. In fact, to a given image point a point $\mathbf{x}^0_{kl}$ on un the image plane π_{kl}, all image points for the camera (i, j) will be of the form $\mathbf{x}_{ij} = \mathbf{x}^0_{ij} + \zeta\,\mathbf{e}^{kl,\,ij} + \rho\,\mathbf{e}^{kl,\,ij}_\perp \;\; \forall\zeta, \rho \in \mathbb{R}$, where $\mathbf{x}^0_{ij}$ is the (unknown) corresponding point and $\mathbf{e}^{kl,\,ij}_\perp = R_z\left(\frac{\pi}{2}\right)\mathbf{e}^{kl,\,ij} = R_z\left(\frac{\pi}{2}\right)K\left(\mathbf{c}^{i,\,j} - \mathbf{c}^{k,\,l}\right)$.

Now, observing that $F^{kl,\,ij}R_z\left(\frac{\pi}{2}\right)\mathbf{e}^{kl,\,ij}_\perp = \pm|K\left(\mathbf{c}^{i,\,j} - \mathbf{c}^{k,\,l}\right)|^2\,(0, 0, 1)^T$ for a given point $\mathbf{x}^0_{kl}$, also the relation $|\mathbf{x}^{0T}_{kl}F^{kl,\,ij}\mathbf{x}_{ij}| = |x^0_{kl\,z}|\;|K\left(\mathbf{c}^{i,\,j} - \mathbf{c}^{k,\,l}\right)|^2\,|\rho|$ holds. Thus, $|\rho|$ is proportional to the distance of the point $\mathbf{x}_{ij}$ from the epipolar line emerging from $\mathbf{x}^0_{kl}$. Then, one may use this relation to select possible correspondent image points, just minimizing the functional

$$S\left(\mathbf{x}_{kl}, \mathbf{x}_{ij}\right) = \frac{|\mathbf{x}^T_{kl}\,F^{kl,\,ij}\,\mathbf{x}_{ij}|}{|K\left(\mathbf{c}^{i,\,j} - \mathbf{c}^{k,\,l}\right)|^2} \quad \forall\,\left(\mathbf{x}_{kl}, \mathbf{x}_{ij}\right). \tag{1.15}$$

Thus, a threshold on the values of $S\left(\mathbf{x}_{kl}, \mathbf{x}_{ij}\right)$ can be set, in order to introduce a criterion establishing the candidate corresponding points.

In order to suppress the ambiguity due to translations parallel to the epipolar lines, one considers a third camera P_{hm}, the associated epipoles $\mathbf{e}^{kl,\,hm}$, $\mathbf{e}^{hm,\,il}$, or equivalently the fundamental matrices $F^{kl,\,hm}$, $F^{hm,\,ij}$ and a set of image points $\{\mathbf{x}_{hm}\}$. Then, by generating all pairs of image points of the form $(\mathbf{x}_{kl}, \mathbf{x}_{ij})$ and $(\mathbf{x}_{kl}, \mathbf{x}_{hm})$, one computes $S\left(\mathbf{x}_{kl}, \mathbf{x}_{ij}\right)$ and $S\left(\mathbf{x}_{kl}, \mathbf{x}_{hm}\right)$ by (1.15). If both values are below a chosen threshold, the the triplet $(\mathbf{x}_{kl},\, \mathbf{x}_{ij},\, \mathbf{x}_{hm})$ are possibly images of the same source point. A further check consists in computing $S\left(\mathbf{x}_{ij}, \mathbf{x}_{hm}\right)$ since $F^{ij,\,hm}$ satisfies the relation (**??**).

In the simulations we performed, in which the image points data where added by a uniform distribuited relative noise of the 0.1% and several uncorrelated points, this method allowed to find the correct triplet by adopting a treshold of 0.04 for the functional S.

The Trifocal Tensor

Simulations of point sources and their images

3D reconstructions applied to simulated sources: list of cases and general estimation of the reconstruction error

The F matrix calibration and consistency relations

Simulation of tracks

Line reconstruction from 2D line images Cases of study: Vertex localization and track slopes, numerical results

1.4.6.2 Algorithms for Track Reconstruction with Coded Mask Images

BOLOGNA now

Maximum Likelihood Expectation-Maximization 3D reconstruction This reconstruction technique with Coded Aperture mask is based on a iterative process of Maximum Likelihood Expectation maximization. The measured data are considered samples from a set of random variables whose probability density functions are related to the photon source distribution according to the model of the data acquisition process. It is possible to calculate the probability that any initial distribution density in the object under study could have produced the observed data. In the set of all possible measured data, the one having the highest of such probability is the *maximum likelihood estimate* of the original photon source distribution. The algorithm can be directly applied to a three-dimensional reconstruction, with the segmentation of the fiducial detector in volume units, hereafter called *voxels*.

The data acquisition process model is based on the assumption that the emissions occur according to a spatial Poisson process in the region of interest of the source. The likelihood associated with the observed data is as follows:

$$L(\lambda) = \prod_{s=1,\ldots,S} e^{-\Lambda(s)} \frac{\Lambda(s)^{H(s)}}{H(s)!} \tag{1.16}$$

where $H(s)$, $s = 1, 2..., S$ is the measured number of photons in the sensor matrix pixel s. H(s), and $\lambda(j)$ represents the unknown photon counts of voxel j of the segmented volume of interest to be estimated from the measured data. The probability matrix $p(j, s)$, named *system matrix*, is the probability that an emission in voxel j is detected in sensor pixel s. The maximization of $L(\lambda)$ can be achieved through the iterative equation:

$$\lambda^{(k+1)}(j) = \frac{\lambda^{(k)}(j)}{\sum_{s=1}^{S} p(j,s)} \cdot \sum_{s=1}^{S} \frac{H(s)p(j,s)}{\sum_{j'=1}^{J} \lambda^{(k)}(j')p(j',s)} \tag{1.17}$$

where $\lambda^{(k)}(j)$ is the estimated number of emitted photons in voxel j at iteration k. The iterative equation converges to the best estimate of the photon source distribution, and for practical reasons the iteration is stopped when the relative likelihood difference between subsequent iterations decreases below a certain threshold.

System Matrix computation The probability for a sensor to detect a photon emitted in a voxel depends mainly on the geometry of the detector, the scintillating photons propagation medium characteristics, and the sensor detection efficiency. By describing each of these factors with a probability matrix, we can express the total probability with a factorization of these effects: $P = P_{geom} \cdot P_{LAr} \cdot P_{sensor}$.

The geometrical probability depends on the geometry of the detector, the camera geometry, and the voxel grid.
Assuming that (i) photons are emitted isotropically from each voxel; (ii) each photon propagates in a straight line; (iii) the distance is large compared to the voxel size, the geometrical probability that a photon emitted from voxel j will be detected from detector s can be approximated as $P_{geom} = \frac{\Omega}{4\pi}$, where the angle Ω is the solid angle subtended by the detector pixel area, with origin in the voxel centre. With a coded aperture mask placed between the region of interest and the sensor, one must consider the portion of sensor area that is “visible" from the voxel through the mask holes [FIG]. In the event that a sensor is visible through multiple holes, the solid angle is given by the sum of the angles subtended by all the visible sensor portions.

1.4.6.3 Calorimetric Reconstruction

1.4.6.4 Reconstruction Performances

GE-LE-BO now

1.4.7 Calibration System

1.4.8 Cryogenic System

BOLOGNA now

1.4.9 First Commissioning in Laboratori Nazionali di Legnaro (LNL)

1.4.10 Integration and Installation in SAND

1.5 Tracker

Introduction ...
Requirements and opportunities of the tracker system ...
Infrastructure...

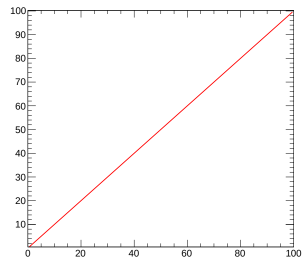

Figure 1.15: Dummy - Here insert the caption.

1.5.1 STT

1.5.1.1 A Compact Modular Design

1.5.1.2 Nuclear and “Solid" Hydrogen Targets

1.5.1.3 Engineering Model

1.5.1.4 Technology and Performance

1.5.1.5 System Integration

1.5.1.6 Electronic Readout

1.5.1.7 Cooling System

1.5.1.8 Data Acquisition and Slow Control

1.5.1.9 Prototyping and Tests

1.5.1.10 Gas System

1.5.1.11 Fabrication and Installation

1.5.1.12 Commissioning

1.5.1.13 Calibration and Monitoring

1.5.1.14 Detector Performance

1.5.2 Drift Chamber

- Backup tracking based on drift chambers with smaller number of channels
- Small scale prototype (30×30 cm^2)
- Beam test with larger prototype (120×80 cm^2)

1.5.2.1 Layout

1.5.2.2 Mechanics

1.5.2.3 Results and Performance

Calibration ...

1.5.3 Gas System

1.6 DAQ Architecture

Data readout in one spill ($\sim$ 3500 Mbits)
Common logic/interfaces board connected to specific front-end board (FEB) of each sub-detector
Endpoints: GRAIN 10, STT 450, ECAL 200
Data acquisition software

This chapters describes the architecture of the Data Acquisition system, as well as the closely related Timing, Trigger and Calibration interfaces, and the runtime configuration of the Front-end (FE) electronics. Each of the SAND subdetectors implements a different architecture for their FE, but must conform to a common standard for interfacing with the DAQ, and also with the Detector Control System (DCS) and Detector Safety System (DSS) described in Sec. 1.7 and 1.8. The element of a subdetector readout system which implements one or more of these standard interfaces will be called an *Endpoint* for the respective interface. The implementation of e.g. the timing distribution, the data processing, or the configuration of the readout boards that takes place inside the Endpoint(s) or between the Endpoint(s) and any separate FEB is the responsibility of the respective subdetector and will not be discussed in this chapter.

The DAQ and the Timing system used in SAND conforms to the design implemented by the other NDs and the far detectors (FDs). The design is summarized here in 1.6.1 and 1.6.2 respectively and more in depth information is available in

1.6.1 DAQ Interfaces

The requirements of SAND in terms of data volumes are modest, at least when compared with those of the FD. A summary of the amount of data produced by the subdetectors during a spill, outside of a spill, and during periodic calibration/alignment runs is shown in Table

1.6.1.1 ECAL

1.6.1.2 GRAIN

GRAIN is read out by custom ASICs mounted in cryogenic readout boards inside the cryostat, which are connected to warm interface boards on the outside. The latter are mounted four per side of GRAIN and serve as endpoints for all common interfaces.

1.6.1.3 STT

1.6.2 Synchronous Interfaces

Requirements, logic and implementation
- overview of DUNE timing system and endpoints
- timing requirements: $<$100 ps within each sub-detector, O(100 ps) among different sub-detectors, $\sim$ 1 ns alignment with the beam
- clock alignment: O(50 ps) for GRAIN, O(100 ps) for STT and ECAL
- clock jitter: $<$ 10 ps for GRAIN, O(10 ps) for STT and ECAL
- synchronization with the beam (custom instrumentation ?)
- $\sim$ ns timing accuracy to disentangle the bunch structure in the spill

1.6.2.1 Trigger

1.6.2.2 Calibration

1.7 Detector Control (DCS)

The DCS has exclusive control on the SAND detector, excluding the control of the cryogenic related to the magnet which responsibility resides with the cryo-group. This control is independent of the DCS as it involves safety aspects critical for the people on site and the experiment operation.

The DCS is built on certified equipment and will require dedicated training for its maintenance. The system will be based on the Ignition system.

The monitoring data collected by the DCS will be made available to the DAQ system as a Detector status authorizing the data acquisition sequence to proceed.

A brief description of the different subsystems, and how the DCS manage them, is given in the following.

1.7.1 DCS Devices

- **Detector Power Control**: The detector power control (DPC) is composed of the power supplies that provide power to the different parts of the detector. The DCS is in charge of processing the requests from the operators, and send the commands to the power supplies. Additionally, the DCS monitors and archives the power supply parameters, such as currents, voltages, temperatures allowing an analysis of the system behavior over time. A DSS system is also implemented and connected to the DCS, displaying an alarm in case any of the configured limits is exceeded. Depending on the severity of the alarms, corrective actions may be taken automatically to protect the detector.
- **Photon Detectors**:
- **Purity Monitors**:
- **Temperature Monitors**:
- **DAQ Rack Control**: The DCS system monitors all working parameters of the water circuit and of the racks and is able to cut power if the ambient temperature raises beyond a settable threshold. It also controls the staged re-powering of racks during a cold start procedure, in order to limit the instantaneous load in the electric distribution system.
- **External Systems**: The cryogenics control system does not belong to the Detector DCS but to the Cryo DCS system. However, the DCS and the DCS cryogenics control system continuously exchange information.

1.7.2 DCS Unifying Standards

The DCS provides a homogeneous environment into which all its parts can be integrated. This environment for the DUNE-SAND experiment is depicted in Fig. 1.16.

The communication protocols used to interact with different hardware components are, in most

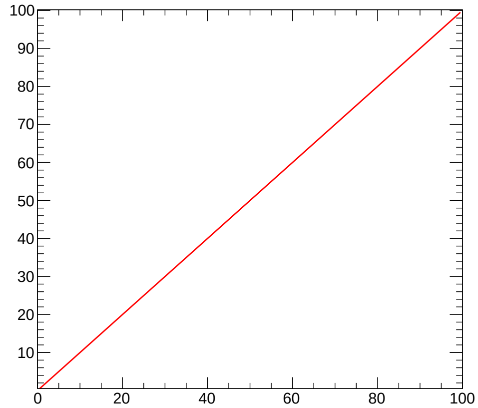

Figure 1.16: DCS preliminary layout.

cases, fixed by the manufacturers. Therefore, the DCS has to be able to support a variety of communication mechanisms and to abstract those, such that their difference is not visible to the higher levels of the supervisory system, as well as to the operators. The communication layers used within DS20k detector and their main characteristics are listed here:

- OPC classic (OLE1 for Process Control Data Access): The OPC Classic specifications are widely used in the Industry as the standard interface for hardware communication.The OPC Classic specifications provide a middleware to decouple the hardware specific elements from the software in charge of its control.
- OPC unified architecture: The OPC Unified Architecture (OPC UA) was designed to enhance and surpass the capabilities of the OPC Classic specifications. Its functionality remains the same but with several improvements that ease its operation.

1.7.3 Detector Operation

The primary challenge for the DUNE-SAND DCS was its extremely tight development and installation schedule. The DCS needed to rely on existing solutions. The software chosen to operate the DCS is a commercial supervisory control and data acquisition (SCADA) toolkit - Ignition. Ignition is based on a distributed product, where quasi-independent processes, called managers, execute different tasks. Those managers do not need to run on the same machine and may be distributed, together with the Ignition internal database, to several computers running on Linux. A critical component in the DUNE-SAND DCS is the Access Control component. With the access control enabled, every user logs in with his personal account to perform any DCS action. Three authorization levels are in use: Monitor, Operator, and Expert. Depending on the user's rights, different actions can be blocked or hidden to protect the detector integrity and to better guide the user.

Another critical interface in the DUNE-SAND DCS system is the integration with the DUNE-DAQ slow control.

In case of emergency situations the DCS will operate and control such interfaces even when the

DAQ is running.

1.7.4 Basic and Advanced Operations

The basic operation of the detector uses a simplified interface that allows to the operators a smooth execution of their tasks, minimizing unintended actions and therefore increasing the stability of the system. For monitoring purposes, the interface uses simple color coding in order to be as straightforward as possible. It is based on two main concepts:

- Dynamic objects, where all the graphical items are dynamic and thus can be used to navigate through the different parts of the detector to see its dedicated panels.
- Data widget, where the datum displayed on the DCS interface is more than a pure value and the operators may perform some extra actions such as plotting its historical values or check its status.

For advanced detector operations, specific and more details panels have been designed. Rather than using an FSM for moving the detector –or its sub-components– to a preset state, the advanced panels allow the experts, credited by the access control, the full control of the different parts of the detector. The advanced panels connect with the lowest level architecture of the detector, allowing the experts to modify operational parameters, set limits for alerts or directly control critical devices.

1.7.5 DAQ-DCS Interfaces

1.7.5.1 Calorimeter

1.7.5.2 GRAIN

1.7.5.3 STT

1.7.5.4 Magnet

Cryogenic Controls
Power

1.8 Detector Safety Systems (DSS)

The DSS is an independent safety system that interacts directly with the Cryogenics, SAND detector sub-components in order to assure the safety of the equipment and people and various power supplies.

The function of the DSS is to detect abnormal and potentially harmful situations, minimizing the resulting damage to the experimental equipment by taking protective actions in order to bring the detectors to a ”safe state“. DSS serves as an equipment protection layer between the Live Protection System (Level 3 alarms at Fermilab), which provides the highest level of safety, and the Slow Controls or Detector Control System (DCS), which performs normal operations. DCS may handle a lower level of safety.

DSS complements existing systems such as DCS or Live Protection System, and sub-detector safety systems that provide an internal sub-detector safety level are also complementary to DSS.

Based on the requirements mentioned above, the following specifications have been defined for the DSS.

- Highly reliable and available, as well as simple and robust.
- provide a cost-effective solution for experimental safety,
- operate permanently and independently of the state of DCS and Live Protections System, able to take immediate actions to protect the equipment,
- Scalable, so that it may evolve with the experiments during their assembly, commissioning, operation and dismantling (a time-span of approximately 20 years),
- Maintainable over the lifetime of the experiments,
- Configurable, so that changes in the setup can be accounted for,
- Able to connect to all sub-systems, services and sub-detector safety systems,
- To exchange information or signals with DCS and Live Protection System

1.8.1 DSS Devices

The detector safety system will be based on SIEMENS PLC architecture that will be connected directly to the DUNE-SAND power supplies as interlocks, and it will be integrated in the Ignition SCADA system as well.

1.8.2 DSS Control Hardware

DSS can adopt the standard industrial solution for critical system, by using Programmable Logical Controller (PLC) with redundant CPU in order to avoid the detector downtime. The choice of the SIEMENS S7-1500H, in particular the CPU 1517H provides an optimal solution for redundancy and high availability systems.

A backup PLC CPU synchronized with the primary PLC CPU ensures that no data is lost in the switchover in case of failure. The switchover time between the failing primary CPU to the backup is less than 100 ms. The synchronization of the CPU's is made via module/optical fiber capable up to 3 km.

The PLC network uses the industrial Ethernet protocol PROFINET, connecting the CPU's with the remote extension I/O in a ring configuration. The PLC ring configuration ensures the proper functioning of the redundancy taking into account all the possible failure cases of the CPU and/or remote I/O.

The CPUs are installed in a rack called DSS CPU racks, and the remote extension I/O is also installed in the DSS Extension rack. The primary CPU is installed either on the surface or in the service cavern, while the backup CPUs are installed in the experimental cavern. Both CPUs are synchronized by means of optical fiber.

The DSS remote expansion racks are the end-points of the DSS signals. DSS signals are only connected by hardware, by means cables. The CPU's racks contains I/O modules for connecting DSS signals. External software protocols or field buses cannot connect to DSS.

- DSS can receive digital input in PLC logic level: Low = 0 V, High = 24 V
- DSS can send digital output signals with dry relay contact format
- DSS can receive analogue signals: 0-10V, 4-20mA, 0-20 mA, PT100, PT1000 type

The design of DSS signals electrical circuit is referred to as fail-safe, due to its intended design to default to the safest mode in the event of a common failure such as a broken connection in the wiring.

The size of the DSS, in other words the number of DSS Remote Expansion racks, depends of the number of signals to be processed.

DSS racks can be strategically placed in the experimental cavern in order to minimize the routing of the DSS cables.

The back-planes allocate the different DSS I/O modules; 4 types of I/O modules are used in the default configuration.

- 32 Digital Input Module
- 32 Digital Output Module
- 8 Analogue Input Module
- 8 RTD Input Module

The I/O modules are plugged into the back-plane, as shown in Figure 1.17, according to the configuration required by the application. They communicate through the back-plane with the first module, which is the Profinet communication module linked to the communication ring.

1.8.3 DSS Rack

The design of the racks is uniform for all DSS racks, maintaining the same layout and components to minimize assembly time, costs, and simplify operation and maintenance. The typical and initial hardware format of the DSS is a 19' rack with a height of 56U, but it can also be produced in other formats such as expansion mini-crates or industrial cubicles. One of the key aspects of the DSS is the power supply circuit, which needs to be highly reliable and readily available, as well as simple and robust. The DSS PLC and all associated instrumentation are powered by 24 VDC (Volts Direct Current).

The 24 VDC is generated from a reliable 220 VAC power supply.

The cables driving the signals from/to DSS PLC are physically connected to specific modules depending of the signal type.

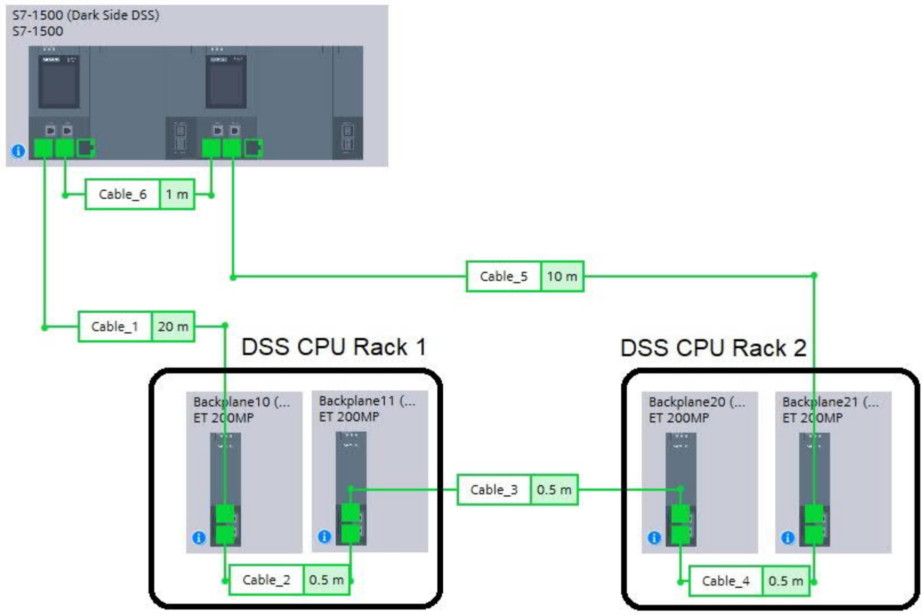

Figure 1.17: Basic layout of a DSS system with only two CPU racks: one in the service cavern and the second one in the experimental cavern. They are connected in a ring topology with the I/O back-planes to ensure redundancy. Each rack contains 2 I/O back-planes.

- The digital input signal are optocoupled and over-voltage protected for all incoming signals to DSS.
- The digital output are interfaced by using electromechanical relays in order to transmit the signals with dry relay contact.
- The analogue signals and PT100/P1000 sensors are also interfaced to the PLC module in order simplify the cable and routing.

1.9 Software and Computing

1.9.1 Code

1.9.1.1 Repositories

1.9.1.2 Formatting

1.9.1.3 Continuous Integration

1.9.1.4 Code Documentation

1.9.2 Simulations

1.9.2.1 Neutrino Fluxes

1.9.2.2 Geometry

1.9.2.3 Event Generator

1.9.2.4 Overlays

1.9.2.5 Particle Propagation

1.9.2.6 ECAL Simulation

...

1.9.2.7 GRAIN Simulation

...

1.9.2.8 STT Simulation

...

1.9.3 Reconstruction (Algorithms)

1.9.3.1 Tracker

1.9.3.2 GRAIN

1.9.3.3 ECAL

1.9.3.4 Global Event Reconstruction

1.9.4 Data Formats

1.9.4.1 Edepsim Output

1.9.4.2 Detector Simulation Output

1.9.4.3 Reconstruction Output

1.9.4.4 Common Analysis Files

1.9.5 Computing resources

1.9.5.1 Data volume

1.9.5.2 Data processing

1.9.6 Visualization

1.9.7 Integration

1.10 Event Reconstruction (Performance)

1.10.1 Single Particle Reconstruction

The reconstruction of single particles produced in neutrino interactions using the available information in the STT and ECAL detectors was firstly studied. Charged tracks are reconstructed starting from the single hits related to the energy deposited by the particle in the active gas of the straws. Figure 1.18 shows the STT hit efficiency as a function of the minimum threshold required in individual straws for muon tracks in ν_μ CC interactions. Thresholds of about 250 eV or lower are possible for tracking purpose, with a single hit efficiency >99.4%. As discussed in Sec. 1.2.4, the FE readout electronics is required to be sensitive down to energies comparable to the one of a single ion pair. In the following a conservative threshold of 250 eV is assumed. This value is consistent with the one used in the ATLAS Transition Radiation Tracker (TRT) [23], although the VMM3 readout foreseen in STT has a lower noise level. It must be stressed that the single hit efficiency for the chosen threshold is higher for p, $e^\pm$, as well as for $\pi^\pm$ and K due to the higher average energy deposition in the straws.

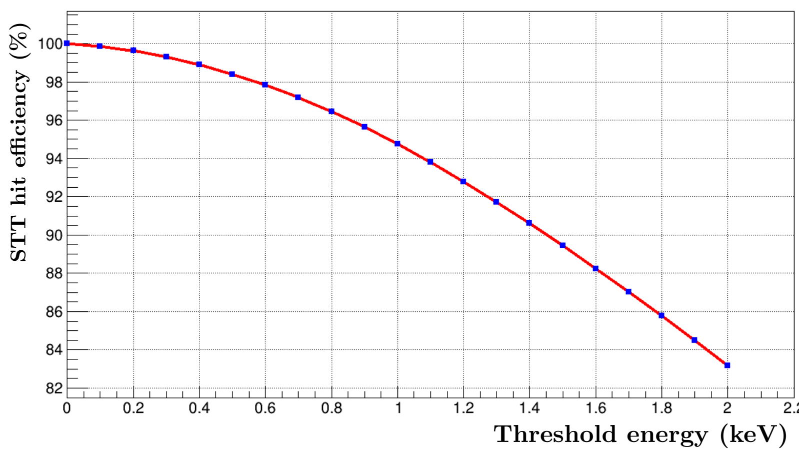

Figure 1.18: STT hit efficiency as a function of the minimum energy threshold applied to the energy detected in the active gas of the straws for muon tracks in ν_μ CC interactions. The gas mixture is Xe/CO_2 70/30 operated at an internal pressure of 1.9 atm. Results are obtained from a GEometry ANd Tracking (Geant4) simulation.

1.10.1.1 Track Reconstruction in GRAIN

Bla bla bla

1.10.1.2 Track Reconstruction in the Tracker (STT)

In order to estimate the detector performance, a simplified method for track fitting has been implemented assuming that the particle (e.g. the muon) track was well identified. The events are selected requiring at least 5 STT hits related to the track in the bending plane ($y - z$ view). This cut implies the introduction of a target fiducial volume (FV), that is the interaction vertex must be at least 30 cm far away from the walls of the detector. The sagitta method, the parabola-fit and the circumference-fit have been tested in order to estimate the muon momentum in the bending plane (p_{yz}). The two fit methods are preferred because they exploit the large number of STT hits and the circumference-fit turns out to be the best one.

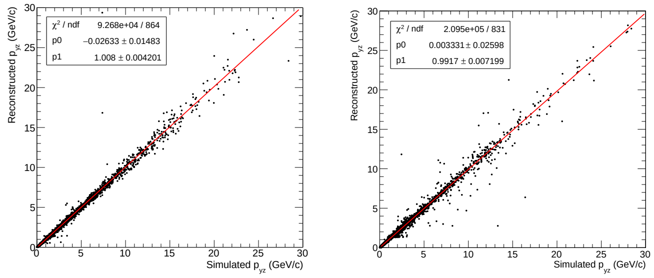

Figure 1.19: FLUKA simulation - Scatter plot of the reconstructed muon momentum on the bending plane vs the simulated one (left: GRAIN LAr, right: STT target).

The track fit, then the curvature in the bending plane and the subsequent momentum estimate, can be improved by taking into account the particle energy loss and the multiple scattering in the crossed material. These effects are exploited in the fit method using the Kalman filter.

Bla bla bla

1.10.1.3 Muon Momentum and Angular Resolutions (from STT Track)

The measurement of the muon momentum has been studied by means of two different simulation codes (Geant4 and FLUktuierende KAskade (FLUKA)). Both the models corresponding to very similar results, details are given only for the FLUKA one, whereas for Geant4 just the results are depicted.

FLUKA simulation - Assuming the DUNE-neutrino beam, two different data samples have been generated. In the first sample 10^4 neutrino interactions are simulated in the LAr in GRAIN, in the second sample 10^4 neutrinos interact in the STT volume (mainly in the radiator). In both cases the muon-track reconstruction is based on the STT hits, assuming a spatial resolution of 0.2 mm on y and x axes and 0.01 mm on z axis (beam axis).

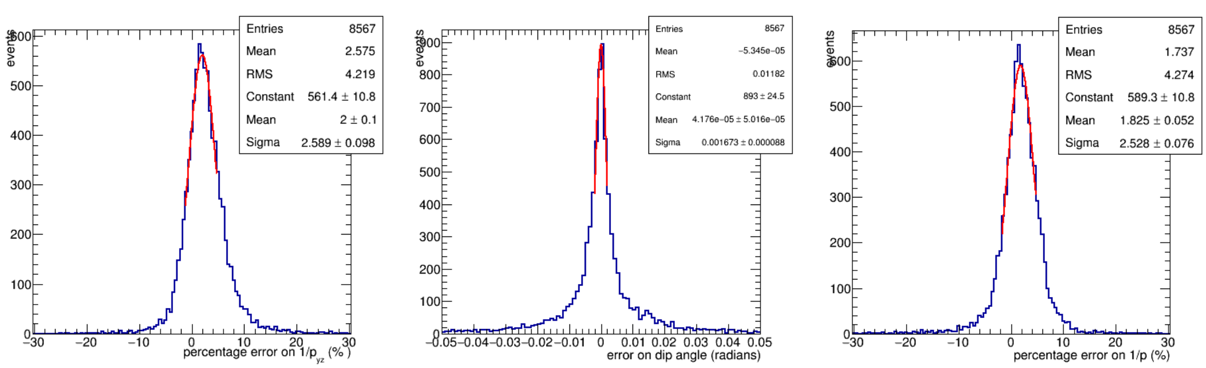

Figure 1.20: FLUKA simulation, GRAIN - Percentage errors on the muon momentum measurement: momentum on the bending plane (left), dip angle (center), momentum (right).

Then two other very loose cuts are applied looking at the fit results. One is referred to the

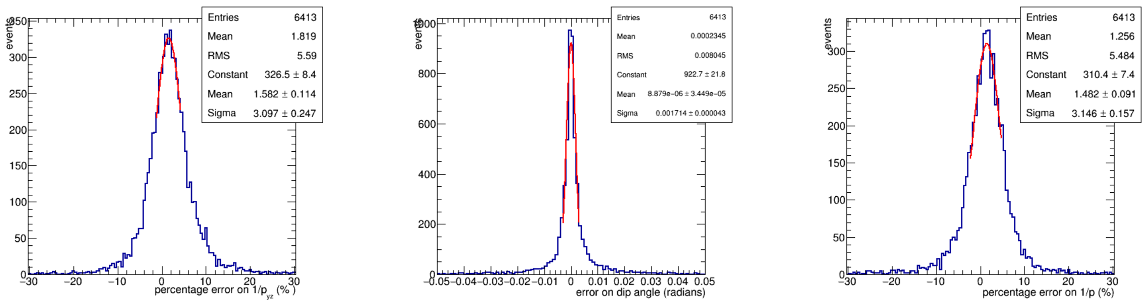

Figure 1.21: FLUKA simulation, STT target - Percentage errors on the muon momentum measurement: momentum on the bending plane (left), dip angle (center), momentum (right).

reduced-chisquare value, and the other one requires that the reconstructed Larmor radius is lower than 200 m, which implies a muon energy lower than ∼36 GeV. After the estimate of the muon momentum in the bending plane (Fig. 1.19), the dip angle (λ) is measured by the fit of the track in the $\rho - x$ plane [24]. As a conclusion the reconstructed muon momentum is $p = p_{yz}/cos\lambda$. Fig.s 1.20 and 1.21 show the percentage error on the measurement of p_{yz}, λ and p for neutrino interactions in the LAr and in the STT, respectively. In Fig. 1.22 the percentage error on p is shown for different neutrino-energy ranges. The dependence of such error on p value is finally summarized in the plots of Fig. 1.23 both for LAr and STT target interactions.

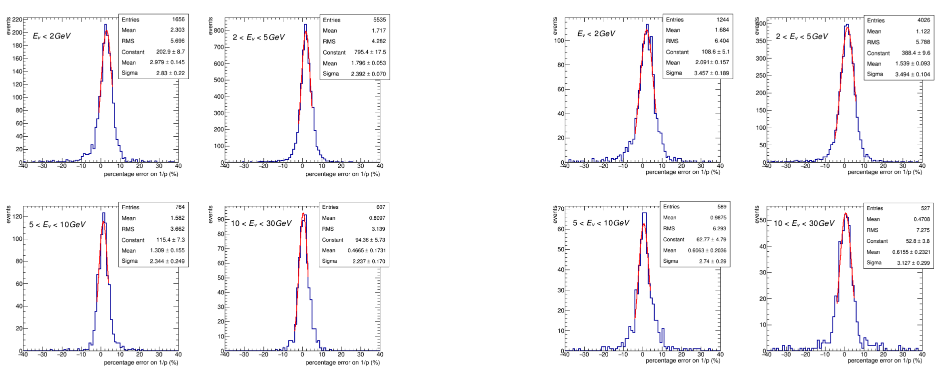

Figure 1.22: FLUKA simulation - Percentage error on the muon momentum in different neutrino-energy ranges. Left: GRAIN target. Right: STT target.

In the case of GRAIN the reconstructed momentum is compared to the *true* momentum after the energy loss in LAr layer. In order to estimate the original muon momentum, the path-length and the energy loss inside LAr should be taken into account by means of the vertex reconstruction.

For both the samples (LAr and STT) the tracking algorithm can be improved by considering the energy losses in the STT volume. Up to now the algorithm has not been updated because this energy-loss effect is estimated very small.

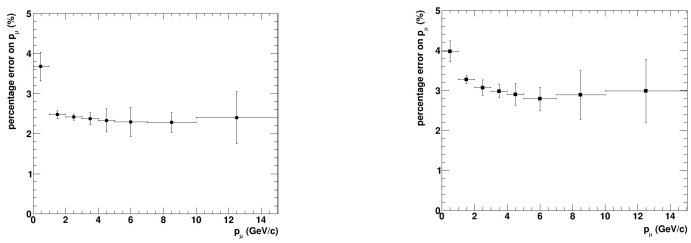

Figure 1.23: FLUKA simulation - Percentage error on the muon momentum as a function of the momentum value. Left: GRAIN target. Right: STT target.

Table 1.3: Uncertainties in the reconstruction of the muon momentum.

Simulation	Target	p_{yz} (%)	dip-angle ($mrad$)	p (%)
FLUKA	GRAIN	2.6 ± 0.1	1.67 ± 0.09	2.53 ± 0.08
FLUKA	STT	3.1 ± 0.2	1.71 ± 0.04	$3.1 \pm 0.2.$
Geant4	STT	3.50 ± 0.05	1.1 ± 0.1	3.43 ± 0.05

Geant4 simulation - The results obtained with Geant4, following the *dunendggd + edep-sim* prescription, are very close to those obtained with FLUKA. The muon track reconstruction is also based on STT hits assuming a spatial resolution of 0.2 mm in the bending plane and on the same event selection described for the FLUKA simulation. Applying a circular-fit for the estimation of the muon momentum p_{yz} and a linear fit for the dip-angle λ in the $\rho - x$ plane, the total muon momentum is reconstructed. The results in terms of percentage uncertainties, as $\delta(1/p)/(1/p) = 3.4\%$, are reported in Tab.1.3.

With this simple and preliminary reconstruction, the muon charge misidentification, defined as the ratio between the number of wrong sign charges and the total number of reconstructed charges, is estimated to be 0.8% in the full momentum range.

1.10.1.4 Electron Momentum and Angular Resolutions

As for the muon performances, the electron momentum and angular resolutions has been studied by means of the two simulations - FLUKA and Geant4. The two codes give very similar results.

FLUKA simulation Taking into account the same FV cut on the interaction vertex - 30 cm from the walls of the detector - and applying a circular-fit model, a percentage resolution on the electron total momentum of 5.3% is obtained (Fig. 1.24, center). As stated in the previous Section, the circular-fit model does not take into account for the energy loss, and this approximation is evident in the non-Gaussian tail on the right side of the distribution shown in Fig. 1.24. This also results in a bias on the mean of 4%. The resolution on the dip-angle λ is 1 mrad with unbiased mean, the angular error distribution is shown in Fig. 1.24 (right).

With this simple and preliminary reconstruction, the electron charge mis-identification for reconstructed tracks is 1.2% in the full energy range.

Geant4 simulation The results obtained with Geant4 are compatible with those obtained with FLUKA. Following the same simulation chain used for muons (*dunendggd + edep-sim*) and applying a circular-fit model, the electron total momentum resolution is 5% with a bias on the mean of 3.8% and the angular resolution on the dip-angle is 0.8 mrad.

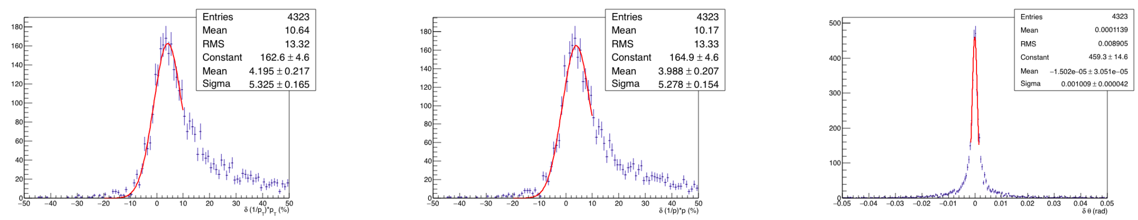

Figure 1.24: Percentage errors on electron momentum in the bending plane p_{yz} (left), on electron total momentum (center) and angular dip-angle resolution (right).

1.10.1.5 π^0 and γ Reconstruction in STT

In order to study the π^0 and γ reconstruction in STT, a sample of about 150k inclusive ν_μ charged current (CC) interactions uniformly distributed throughout the STT tracking volume has been simulated with Generates Events for Neutrino Interaction Experiments (GENIE)+Geant4.

The average number of π^0 produced per CC event is 0.375. Figure 1.25 shows the energy distribution of all the π^0 produced (left plot). About 1.2% of these π^0 undergo Dalitz decay $\pi^0 \to \gamma e^+ e^-$ with direct production of an e^+e^- pair. The maximal length of STT along the central diameter corresponds to about 1.34 X_0 – average density $\sim$ 0.18 g/cm^3 – and photons, on average, cross about 0.67 X_0 of material before reaching the ECAL (Sec. 1.5.1). Therefore, a significant fraction of the remaining γ from π^0 decay is expected to convert into e^+e^- pairs within the STT tracking volume. Figure 1.25 shows the energy distribution for the γ converted in STT (right plot), which are relatively soft.

The average fraction of γ converting into e^+e^- pairs within the STT tracking volume is 29.2%. This number is consistent with the expectations based upon the average amount of material crossed in STT. Figure 1.26 shows the distribution of the distance traveled by the γ reaching the ECAL without converting (left plot) and the distance between the primary vertex and the conversion point for γ converting in STT (right plot). This latter distribution is relatively broad, with an average value of about 1 m. The fraction of π^0 with at least one γ converting into an e^+e^- pair within the STT tracking volume is about 49%. Events with a converted γ allow a more accurate reconstruction of the π^0, given the excellent angular and momentum resolution of STT for the e^+e^- tracks. As discussed in Sec. 1.2.4, the large sample of converted γ available in STT will also provide a direct calibration of the electron identification and reconstruction efficiency. Figure 1.27 shows the reconstruction efficiency for the V^0 conversion $\gamma \to e^+e^-$ in the STT volume.

1.10.1.6 π^0 Identification and Reconstruction in CC

The sample used to study π^0's, is composed by ν_μ CC interactions with the vertex located inside the tracking volume.

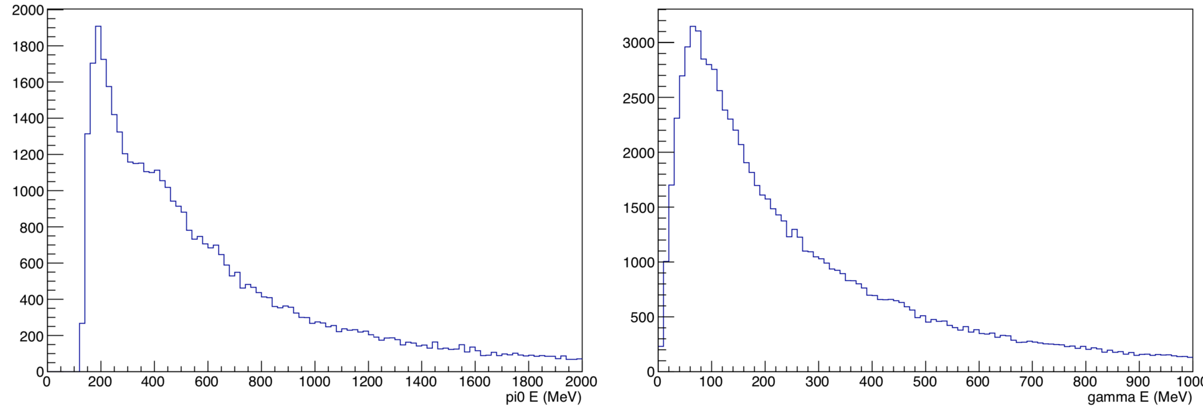

Figure 1.25: Left plot: energy spectrum of π^0 produced in inclusive ν_μ CC events with the default FHC beam. Right plot: energy distribution of γ originated from π^0 decay and converted into an e^+e^- pair within the STT tracking volume. Both distributions are obtained from GENIE+Geant4 simulations.

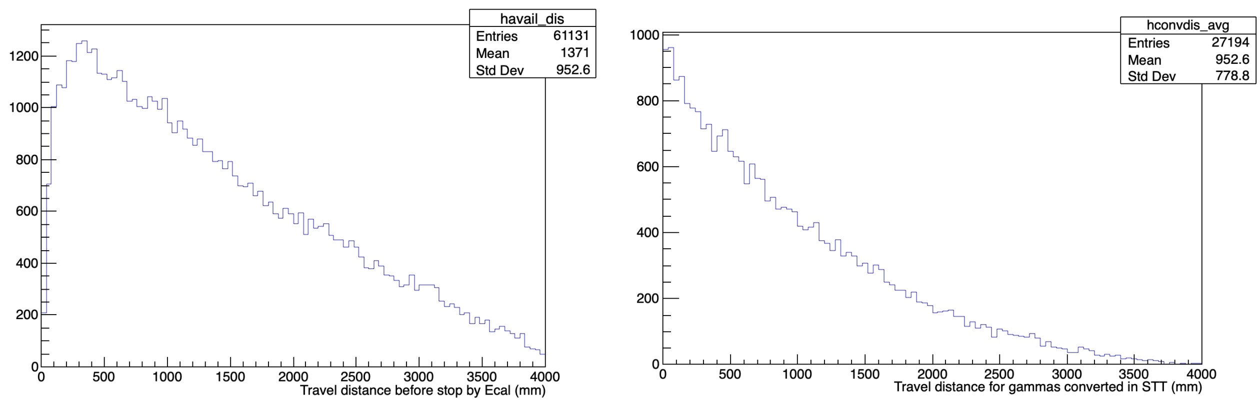

Figure 1.26: Left plot: distance traveled by the γ originated from π^0 decay before they reach the ECAL. Right plot: distance traveled by the γ from π^0 decay that convert within the STT tracking volume. The distributions are obtained from GENIE+Geant4 simulations.

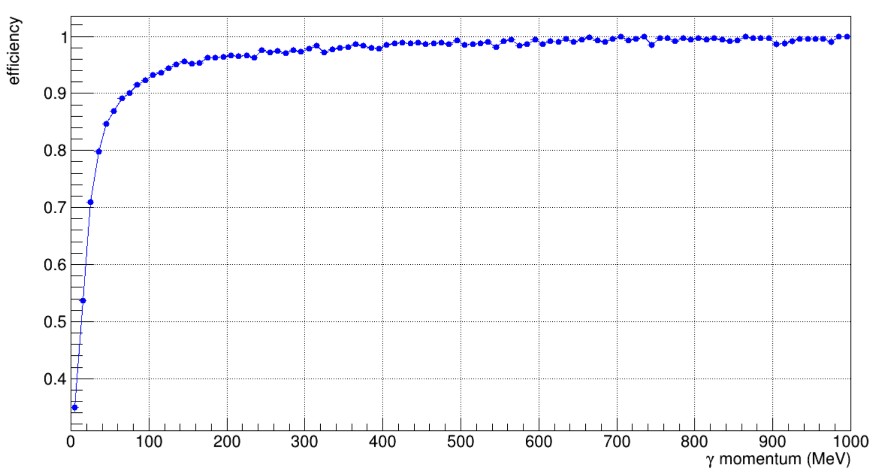

Figure 1.27: Reconstruction efficiency as a function of momentum for the conversion $\gamma \to e^+e^-$ in the STT volume. A minimum number of 4 STT hits in the YZ bending plane is required for both tracks.

To develop the algorithm for the π^0 reconstruction, a dedicated sample composed by 40000 events has been produced. The number of π^0 that decay in two photons is tabulated in Tab. 1.4.

Table 1.4: Number of π^0 that decay in two photons.

Number π^0	number of events	number of events (%)
0	25524	63.8
1	10580	26.5
2	2802	7.0
3	772	1.9
4	235	0.6
≥ 5	87	0.2
Total	40000	100

The energy spectrum of this sample is shown in Fig. 1.28.

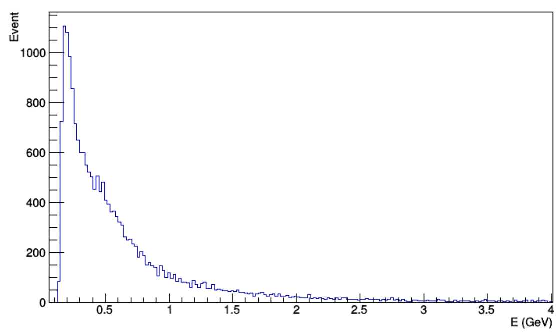

Figure 1.28: Energy spectrum of π^0 produced in inclusive ν_μ CC interactions from FLUKA simulations.

In order to develop and test the algorithm, a restricted sample with only one π^0 was selected. The calorimeter hits are associated and merged into a cluster if $\Delta x = 20$ cm and $\Delta\phi = 5°$. x is the distance along the axis of the KLOE magnet and ϕ is the azimuthal angle. These values were optimized using hits from π^0 maximizing the number of events with two reconstructed clusters while keeping the contamination of hits originating from other charged particles at a few per cent level.

Two cuts in energy are also applied: before the clusterization procedure, hits with energy lower then 1 MeV are discarded; after the clusterization, only clusters with total energy (defined as the sum of the hit energy) higher than 20 MeV are retained. The number of reconstructed cluster are tabulated in Tab. 1.5.

As first stage, only events with two reconstructed clusters were considered. The comparison between the true Monte Carlo energy and the reconstructed one (defined as the sum of the two cluster energy) is shown in Fig. 1.29.

The invariant mass of the π^0 is computed from the two clusters. Finite energy and position

Table 1.5: Number of reconstructed clusters with energy higher than 20 MeV, using the criteria $\Delta x = 20$ cm and $\Delta\phi = 5°$ for 1-π^0 events.

Number of clusters	number of events (%)
0	0.2
1	10.8
2	63.7
3	17.9
4	4.8
$\geq$ 5	2.6

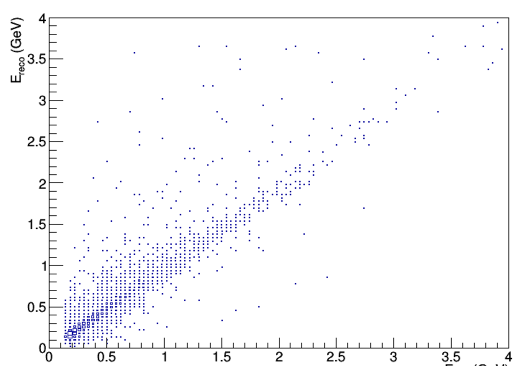

Figure 1.29: True energy (E_{true}) vs reconstructed energy (E_{reco}) in two reconstructed clusters for 1-π^0 events.

reconstruction effects are introduced at this stage smearing the true MC information of the clusters. The energy resolution is parametrized as $\sigma_E/E \simeq 5.7\%/\sqrt{E(GeV)}$. The position of the cluster is defined as the energy weighed barycenter of the hits ($E_{hits} > 1$ MeV) belonging to the cluster. The barycenter is smeared according to the space resolution of the KLOE calorimeter (4.5 mm). The invariant mass resolution for the sample of ν_μ CC events with 1-π^0 and two reconstructed clusters is 13.5%, as shown in Fig. 1.30, left.

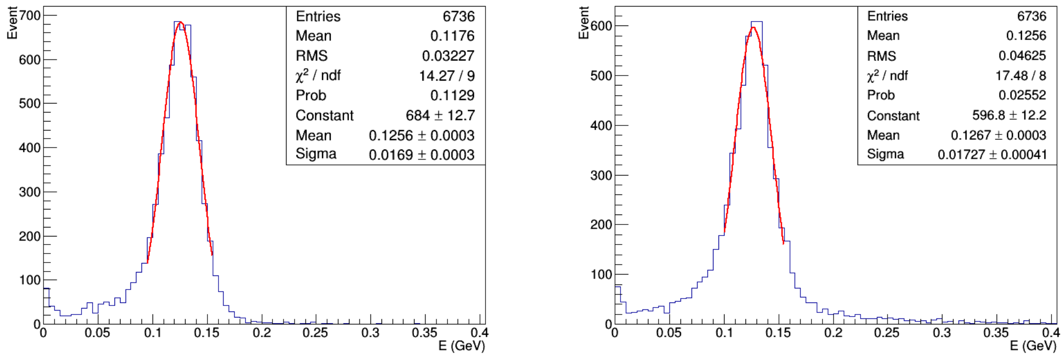

Figure 1.30: Invariant mass for two cluster event reconstructed by means true MC π^0 hits (left) and all hits deposited in the calorimeter (right). The red curve is the Gaussian fit.

1.10.1.7 Proton Reconstruction

The proton reconstruction in STT depends primarily upon the average density of the detector – tunable in the range $0.005 \leq \rho \leq 0.18$ g/cm^3 (Sec. 1.5.1) – since the relatively large energy loss of protons in matter implies short track lengths. In this section the results obtained with the maximal density of about 0.18 g/cm^3, corresponding to the lowest proton reconstruction efficiency, are discussed.

About 350k inclusive ν_μ CC interactions randomly distributed within the STT volume using GENIE+Geant4 with a detailed implementation of the detector geometry have been simulated. The largest fraction of events are originated from interactions with the C nucleus in the CH_2 and graphite targets. Figure 1.31 shows the total number hits (crossed straws) for proton tracks as a function of the proton momentum for events originated in the C nucleus. The proton track crosses typically a small number of straws at low momenta. Although the proton tracks have large angles with respect to the beam direction (Fig. 1.31), the higher track sampling of STT in the transverse direction (0.15 X_0) with respect to the longitudinal one (0.36% X_0) allows a rather uniform track reconstruction as a function of the angle.

In order to determine the proton momentum from a fit of the track curvature in the B field, it is needed the proton track to have a minimum number of four hits in the bending YZ plane. This requirement implicitly introduces a momentum threshold since different X layers of straws (providing hits in the YZ plane) are separated by thin CH_2 or graphite passive targets (Sec. 1.5.1). Figure 1.32 shows the momentum distribution and the reconstruction efficiency as a function of the momentum for protons originated from ν_μ CC interactions with the C nucleus. The average reconstruction efficiency is 65.9%. Table 1.6 summarizes the corresponding reconstruction efficiencies for the various interaction types. The smaller reconstruction efficiency for quasi-elastic processes is related to the lower momenta and larger angles.

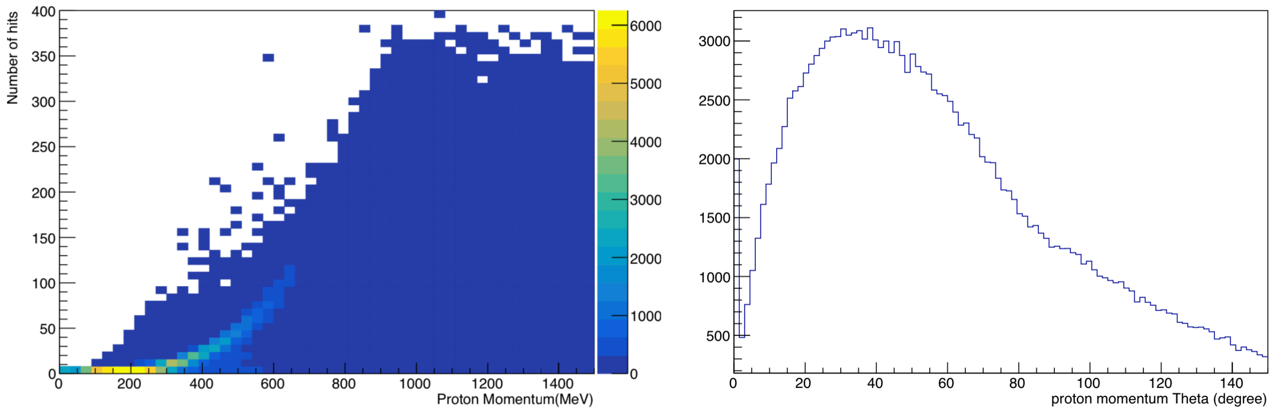

Figure 1.31: Left plot: total number of hits in STT (including both X and Y straws) for protons produced in ν_μ CC interactions on C (from CH_2 and C targets) as a function of the proton momentum. Right plot: proton angle with respect to the beam direction for protons produced in inclusive ν_μ CC interactions on C.

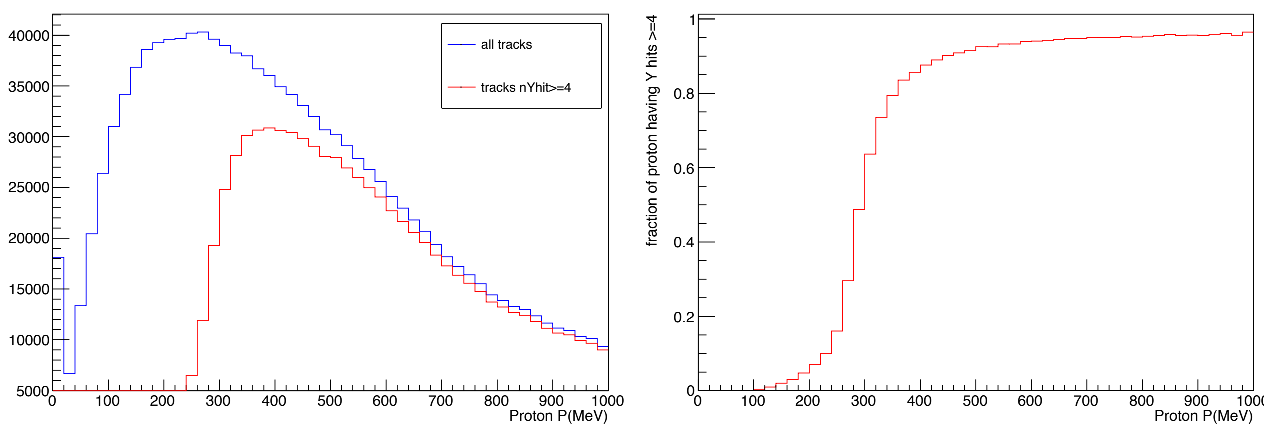

Figure 1.32: Left plot: momentum distribution for all (blue) and reconstructed (red) protons produced in ν_μ CC interactions on C (from both CH_2 and C targets) in STT. Right plot: proton reconstruction efficiency as a function of the proton momentum for ν_μ CC interactions on C in STT. A minimum number of four hits in the bending YZ plane is required.

Table 1.6: Proton reconstruction efficiency for various processes in ν_μ CC interactions on C and H. A minimum number of four hits in the bending YZ plane is required.

Target	QE	RES	DIS	Total
Carbon	53.3 %	66.7 %	73.6 %	65.9 %
Hydrogen	–	93.0 %	96.0 %	94.1 %

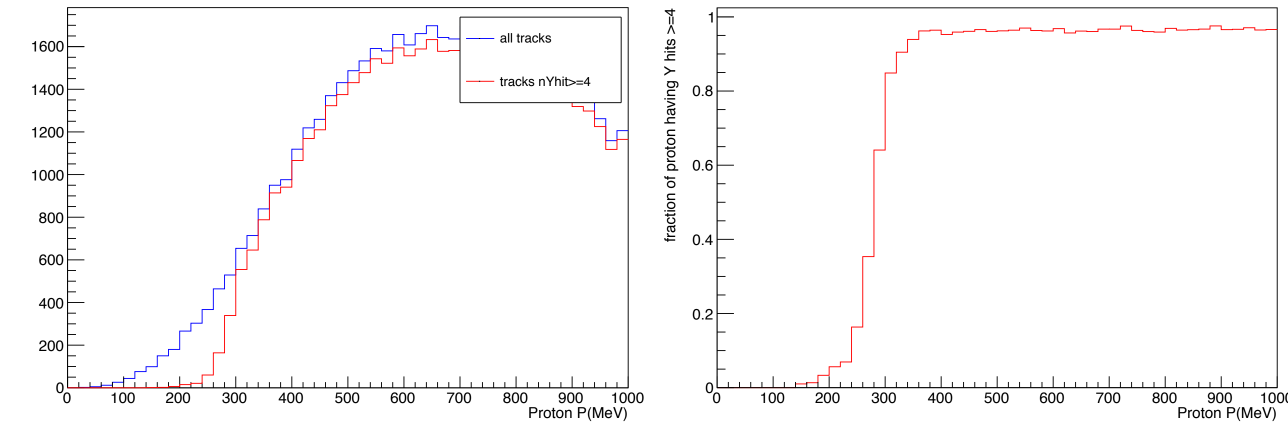

Figure 1.33: Left plot: momentum distribution for all (blue) and reconstructed (red) protons produced in ν_μ CC interactions on H (within the CH_2 target) in STT. Right plot: proton reconstruction efficiency as a function of the proton momentum for ν_μ CC interactions on H in STT. A minimum number of four hits in the bending YZ plane is required.

The reconstruction of protons originated from ν_μ CC interactions on hydrogen is particularly interesting, since one of the primary goals of the STT is to provide high statistics samples of $\nu(\bar{\nu})$-H interactions (Sec. 1.11.2). The proton reconstruction efficiency directly affects the overall selection efficiency for many of the available processes on H, including the $\nu_\mu p \to \mu^- p \pi^+$ events used for the flux determination (Sec. 1.11.3). The absence of nuclear smearing and the lack of the ν_μ quasi-elastic process in H imply higher momenta (Fig. 1.33) and smaller angles with respect to the beam direction. As a result, higher reconstruction efficiencies and lower thresholds are obtained for protons originated in interactions on H (Fig. 1.33). The average proton reconstruction efficiency on H is about 94%. Table 1.6 summarizes the corresponding reconstruction efficiencies for the various interaction types. It is noteworthy that a further increase of the average STT density beyond 0.18 g/cm^3 would start to significantly reduce the proton reconstruction efficiency for events on H. For this reason the value of $\rho \sim 0.18$ g/cm^3 is chosen as the maximal density in the STT design, still allowing the reconstruction of most protons from events on H. Protons originated from interactions on C not only have a lower reconstruction efficiency, but typically also shorter tracks and worse momentum resolution compared to interactions on H. These differences help to reduce the C background in the kinematic selection of H interactions (Sec. 1.11.2), effectively using the STT detector to filter out some of the C background.

The results discussed above refer to the reconstruction of the proton momentum by fitting the track curvature in the magnetic field. In principle, for shorter tracks (lower momentum) it is still possible to reconstruct the proton from the energy deposition in the crossed straws, thus reducing the reconstruction threshold. Although this capability is not used in current analyses, dedicated studies are ongoing.

1.10.1.8 Neutron Detection

Neutron detection efficiency The signal induced from neutron interaction can be observed in the calorimeter or with lower probability in the straw tube tracker. The amount and type of materials used, as well as the granularity of the active elements of the detectors, directly affect the neutron detection efficiency. In the KLOE calorimeter, thanks to the large percentage (about 50%)

Table 1.7: Neutron detection efficiency for various processes in $\bar{\nu}_\mu$ CC interactions on C and H in the default RHC beam. A minimum threshold on the detected energy of 1.1 photoelectrons in ECAL and 250 eV in STT is required.

STT+ECAL	QE	RES	DIS	Total
Carbon	64.8 %	76.5 %	80.1 %	73.6 %
Hydrogen	80.5 %	85.0 %	87.4 %	82.3 %

of lead in a structure of organic fiber scintillators, the neutron detection efficiency is enhanced due to the abundant production of secondary particles in inelastic interactions of the neutrons with high Z material. The signal collected from each cell (see Sec. **??** for the details) can be acquired if the total energy detected in the scintillating fibers is higher than 1.1 photoelectrons. On the other hand, neutron interactions in the STT detector are not as probable as in the calorimeter, due to the STT low mass. Nevertheless, the signal can be detected when the deposited energy in an interaction is higher than 250 eV.
A detection efficiency study was performed using GENIE+Geant4 simulations, in particular about 500k inclusive $\bar{\nu}_\mu$ CC interactions with the default RHC beam, randomly distributed within the STT volume, have been simulated. The largest fraction of events are originated from interactions with the C nucleus in the CH_2 and graphite targets. For each event the total neutron energy

$$E_N = \sum_{i=1}^{N_{tot}} E_n^i \tag{1.18}$$

defined as the sum of the neutron kinetic energy E_n for all the primary neutrons N_{tot} in the neutrino final state interaction was calculated and the fraction of neutrino energy carried out from neutrons versus the neutrino energy is shown in Fig. 1.34, left. In Fig. 1.34, right the mean value of the neutron energy for each interaction was evaluated versus the neutrino energy. As it results from the plots the neutron energy is peaked at lower energy since the mean value for $\langle E_N \rangle$ is about 170 MeV and the fraction of neutrino energy carried out from all neutrons is usually lower than 0.5 for neutrino energy lower than 5 GeV and it is no more than 0.3 for higher neutrino energy.
By analyzing the signal coming from each calorimeter cell and from the STT, the neutron efficiency was studied for the two detectors as a function of the kinetic energy of the neutrons emitted from interaction vertex inside the STT FV.

Figure 1.35 shows the momentum distribution and the detection efficiency as a function of the momentum for neutrons originated from $\bar{\nu}_\mu$ charged current interactions with the C nucleus. As expected, the calorimeter efficiency is much higher than the STT efficiency even if the STT contribution is relevant at lower energy.

Table 1.7 summarizes the corresponding reconstruction efficiencies for the various interaction types. The smaller reconstruction efficiency for quasi-elastic processes is related to the lower momenta.

The reconstruction of neutrons originated from CC interactions on hydrogen can directly affect the overall selection efficiency for many of the available processes on H, including the $\bar{\nu}_\mu p \to \mu^+ n$ events used for the $\bar{\nu}_\mu$ flux determination (Sec. 1.11.3). The absence of nuclear smearing in H results in higher average momenta (Fig. 1.36). As a result, slightly higher reconstruction efficiencies are obtained for protons originated in interactions on H (Fig. 1.36). The average neutron reconstruction

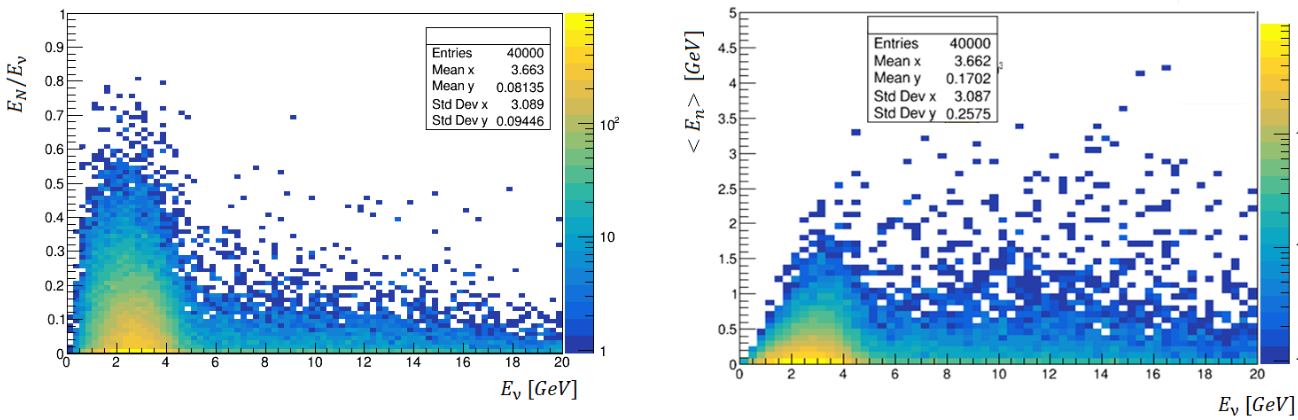

Figure 1.34: Left: Ratio of the total neutron energy E_N defined in eq. 1.18 to the neutrino energy E_ν versus the neutrino energy. Right: Mean value of the neutron kinetic energy for neutrino interaction versus neutrino energy.

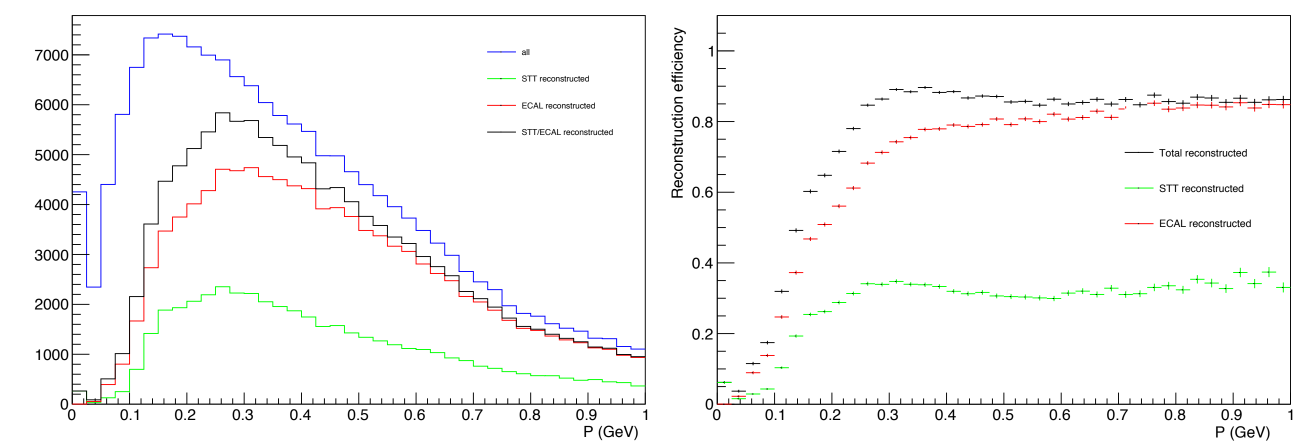

Figure 1.35: Left plot: momentum distribution for all neutrons (blue) and neutrons reconstructed in ECAL (red) and STT (green) in $\bar{\nu}_\mu$ CC interactions on C (from both CH_2 and C targets) in STT. Right plot: neutron reconstruction efficiency as a function of the neutron momentum for $\bar{\nu}_\mu$ CC interactions on C in STT. A minimum threshold of 1.1 photoelectrons in ECAL and 250 eV in STT is required.

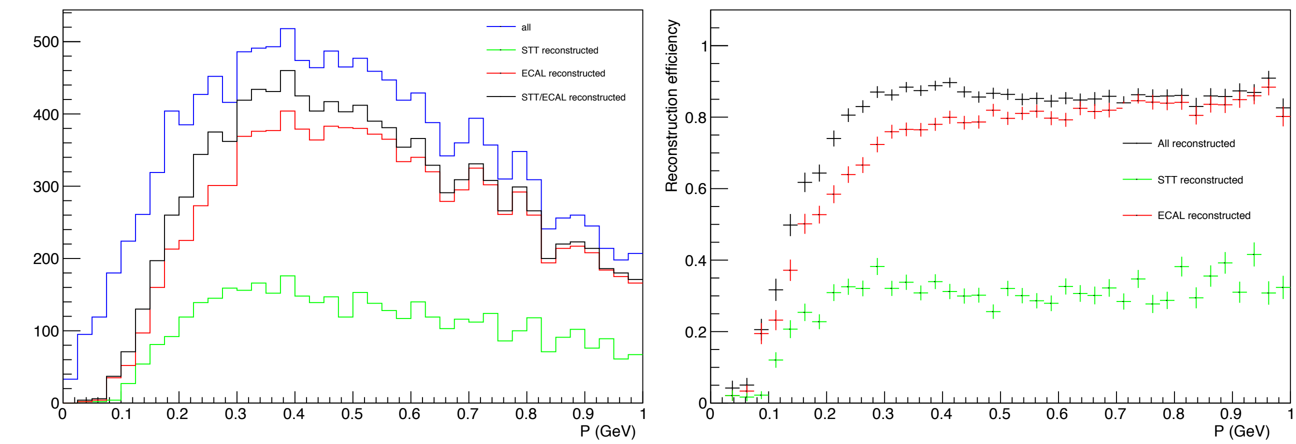

Figure 1.36: Left plot: momentum distribution for all neutrons (blue) and neutrons reconstructed in ECAL (red) and STT (green) in $\bar{\nu}_\mu$ CC interactions on H (within the CH_2 targets) in STT. Right plot: neutron reconstruction efficiency as a function of the neutron momentum for $\bar{\nu}_\mu$ CC interactions on H in STT. A minimum threshold of 1.1 photoelectrons in ECAL and 250 eV in STT is required.

efficiency on H is about 82.3%. Table 1.7 summarizes the corresponding reconstruction efficiencies for the various interaction types.

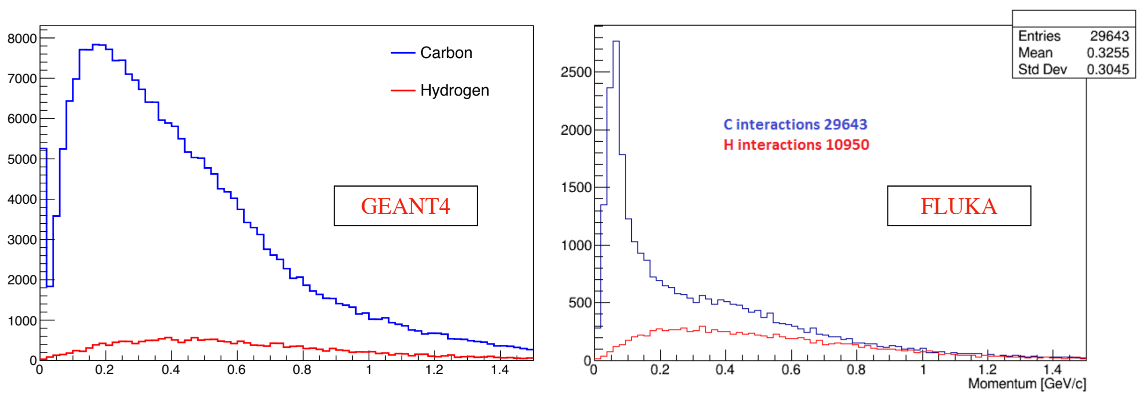

Figure 1.37: Momentum distribution of neutrons originated in $\bar{\nu}_\mu$ CC interactions within the STT FV with the RHC beam in GENIE+Geant4 (left plot) and FLUKA (right plot) simulations. Both interactions on carbon and hydrogen are shown for comparison.

A similar analysis was performed also with FLUKA simulation described in Sec. **??**, where the STT and the barrel of the KLOE calorimeter with fibers and lead was implemented. In particular, the quenching effect for the generated light was taken into account, as well as light attenuation and the time spread due to photon propagation inside the fibers. For these analysis charged current anti-neutrino interactions in the STT FV were considered even if only the neutron interacting and detected in the barrel were considered for the efficiency study since endcaps were simulated as an homogeneous medium. A comparison of the corresponding neutron spectra with the GENIE+Geant4 simulation is shown in Fig. 1.37. In these simulations an configuration of STT with a total radiator mass of about 5.5 ton was considered with respect to the previous study where a total mass of 7.4 ton was considered. For these reasons the results are not easily compatible with the Geant4 simulations reported in before. As for the analysis of GENIE+Geant4 simulation, it is required a minimum threshold on the detected energy associated to the hits of secondary

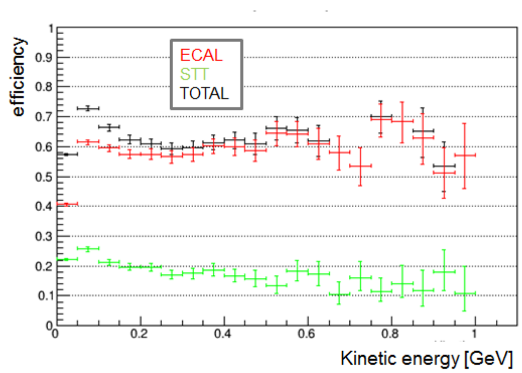

Figure 1.38: The neutron detection efficiency of the calorimeter (in red), of STT (in green), of the whole apparatus calorimeter + STT (in black) as a function of the neutron kinetic energy at the neutrino interaction vertex.

particles from neutron interactions of 1.1 photoelectrons in ECAL and 250 eV in STT. In figure 1.38 the detection efficiency is shown as a function of the neutron kinetic energy at the vertex, for the calorimeter (red), the STT (green) and their combination (black). The energy threshold considered for STT was 250 eV. Taking into account the total number of neutrons generated in neutrino interactions 21% was detected by the STT, while 49% was detected by the calorimeter. In conclusion, taking into account the cases in which the neutron is detected from both the detectors, the global neutron detection efficiency of the whole apparatus is about 61%. A very similar neutron efficiency was found for interaction vertex in the Liquid Argon target, where a global efficiency of 64% resulted.

Neutron energy reconstruction by time of flight (ToF) technique

In this analysis the kinetic energy of neutrons was determined by the ToF technique. By exploiting the knowledge of position and time of deposited energy in the calorimeter or in the STT detector and by using the vertex information from the Monte Carlo simulations, the neutron kinetic energy was reconstructed for each detected neutron. If the energy deposited from neutrons or neutron daughters was detected both in the STT and in the calorimeter, the hit with the smallest time was selected for reconstructing the velocity of the primary neutron. A time smearing of $\sigma = 0.8$ ns was considered for the STT. When the neutron velocity is reconstructed by exploiting the interactions in the calorimeter, only the cells with a detected energy bigger than 1.1 photoelectrons are considered. For each cell the reconstructed time and the coordinate of the interaction were calculated as the weighted average on the deposited energy of the times and coordinates of the hits occurring inside the cell. In figure 1.39 the histogram of β_{reco} versus $\beta_{true} = P/E$ (where P is the momentum and E is the neutron total energy) for all neutrons detected is shown.

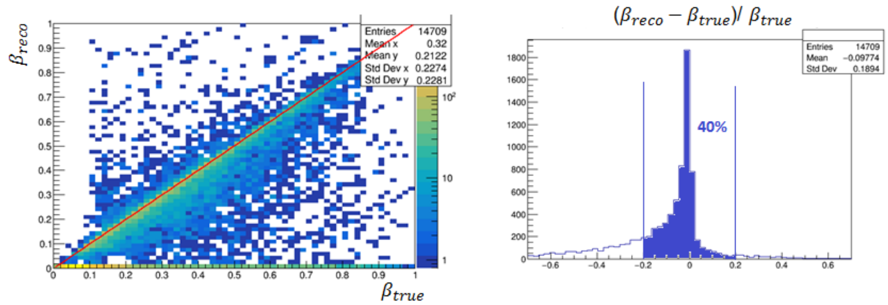

Figure 1.39: Left: β_{reco} vs β_{true}. Right: overall resolution of neutron kinetic energy reconstruction; in the coloured area where $\frac{\beta_{reco}-\beta_{true}}{\beta_{reco}} < 0.2$, the 40% of the total events was found.

Except for a small fraction of neutrons, whose reconstructed energy is close to zero, a big fraction of neutrons with β_{true} higher than 0.3 shows a good energy reconstruction by the ToF technique. In particular the fraction of neutrons for which $\frac{\beta_{reco}-\beta_{true}}{\beta_{reco}} < 0.2$ is about 40%. On the other hand, some detected neutrons are reconstructed with a very low energy. This happens when neutrons interact by elastic scattering and when the secondary particles were not detected. In fact, for these events, the signal induced in the detector is mainly due to interactions occurring very far from the first interaction of the primary neutron.

For each event the total neutron reconstructed energy E_N^{reco} was evaluated by summing the reconstructed energy of each detected neutron and the total reconstructed energy was compared with the true total neutron energy E_N^{true} calculated by using Monte Carlo information. The plot of E_N^{reco} versus E_N^{true} is shown in Fig. 1.40 at left. Since in each event some neutrons are emitted with very low energy and these are detected with very low efficiency, the reconstructed energy distribution is broader than the distribution of β_{reco} versus β_{true} shown in Fig. 1.39. However as it is shown in Fig. 1.34, the fraction of neutrino energy carried out by neutrons is on average very small and close to 6%. For this reason as it results from the plots in Fig. 1.40 the total neutron energy is reconstructed within 30% for 26% of interacting antineutrinos and this fraction increases with the ratio E_N^{true}/E_ν since at higher neutron energy the neutron detection efficiency is higher and the neutron energy resolution improves.

Neutron angle reconstruction

The angle θ between the detected neutron and the beam axis was reconstructed by considering the vertex interaction point and the neutron detection position in a STT module or in the calorimeter cell. A Gaussian smearing of 2 mm was applied to the coordinate along the beam axis of the interaction point, while a different smearing was applied on the neutron detection position accordingly

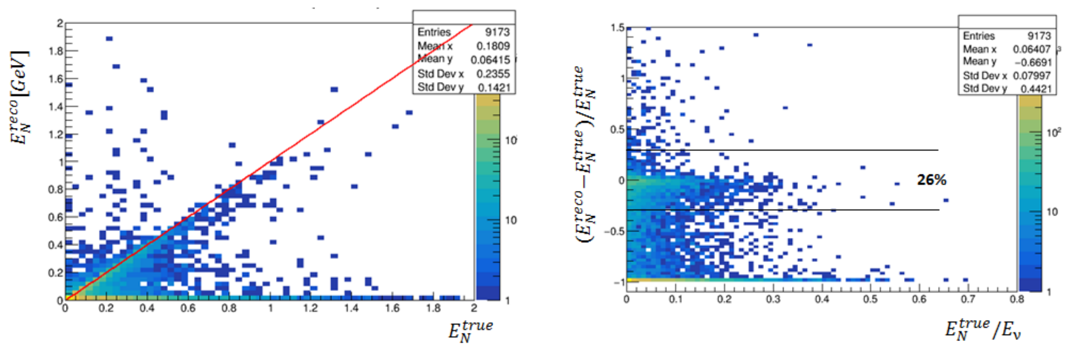

Figure 1.40: Left:The reconstructed total neutron energy E_N^{reco} versus the true total neutron energy E_N^{true}. Right: Total neutron energy resolution defined as $(E_N^{reco}-E_N^{true})/E_N^{true}$ versus the ratio E_N^{true}/E_ν of the true total neutron energy to the neutrino energy.

to the calorimeter and STT properties. In particular, if the neutron was detected in the calorimeter, the coordinates of the center of the calorimeter cell were used and it was applied a smearing of few cm to the true coordinate along the longitudinal direction of the cell. On the contrary, if the neutron was detected in the STT, the true hit coordinate was considered due to the very high position resolution of the STT detector. For this analysis only the quasi elastic interaction of antineutrino on Hydrogen present in the CH_2 radiator slabs placed between the STT modules, were considered. The reconstructed angle distribution versus the true angle distribution as achieved by Monte Carlo information are shown in Fig. 1.41 for neutron detected in the calorimeter and in the STT.

As expected the resolution on the angle reconstruction is better for neutron detected in the STT, even if, as seen in the previous section, here the neutron efficiency is lower. As it resulted from plot in the bottom of Fig. 1.41, the distribution of $(\theta_{reco}-\theta_{true})/\theta_{true}$ has a FWHM about 1% and about 0.02% for neutrons detected in the calorimeter and in the STT, respectively.

This results is very important since for quasi elastic interaction on Hydrogen (which is a two body process $\bar{\nu}_\mu p \rightarrow \mu^+ n$) if the muon momentum, the neutron energy and the neutron angle are well reconstructed the neutrino energy can be directly calculated by kinematics with very high accuracy.

1.10.1.9 K^0 and Λ^0 Reconstruction

As described in Sec. **??**, the decays $K_s^0 \rightarrow \pi^+\pi^-$ and $\Lambda^0 \rightarrow p\pi^-$ are used to calibrate the momentum scale in STT, as well as the proton reconstruction and identification. The unique combination of low-density and relatively large fiducial mass offered by STT allows the collection of a large statistics for both decays, uniformly distributed throughout the STT FV (Fig. 1.42).

Figure 1.43 shows the distance between the displaced V_0 vertex and the primary vertex for $K_s^0 \rightarrow$

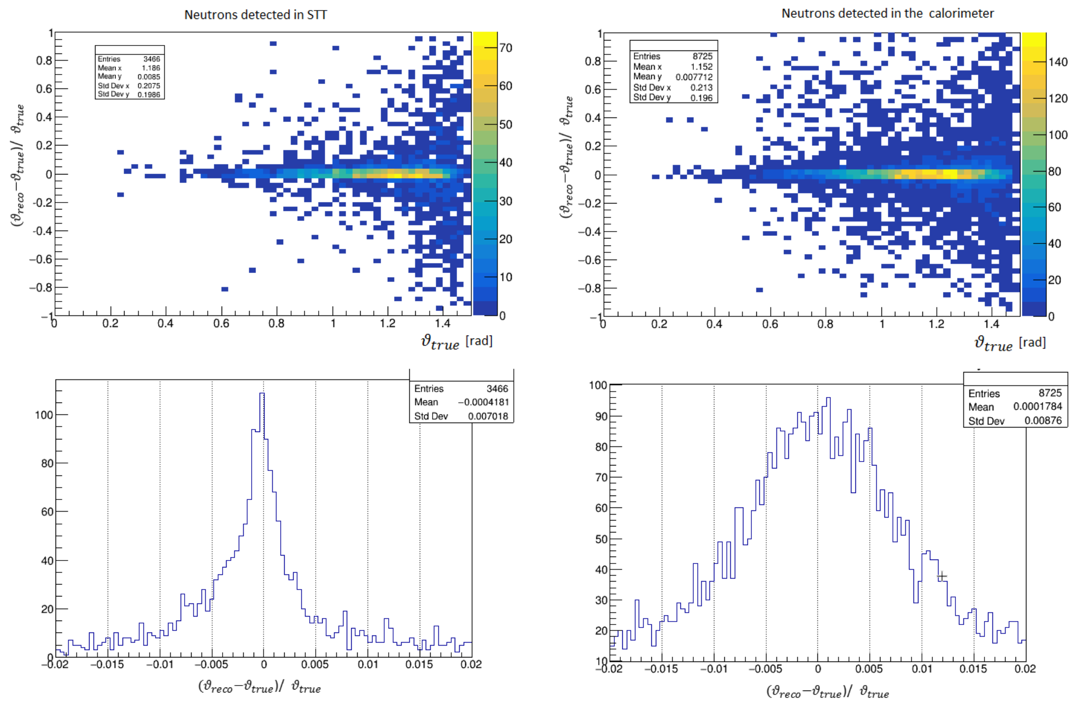

Figure 1.41: $(\theta_{reco} - \theta_{true})/\theta_{true}$ versus θ_{true} for neutron detected in the STT at left and in the calorimeter in the right part. In the bottom plots the global resolution $(\theta_{reco} - \theta_{true})/\theta_{true}$ integrated on all θ_{true} is shown.

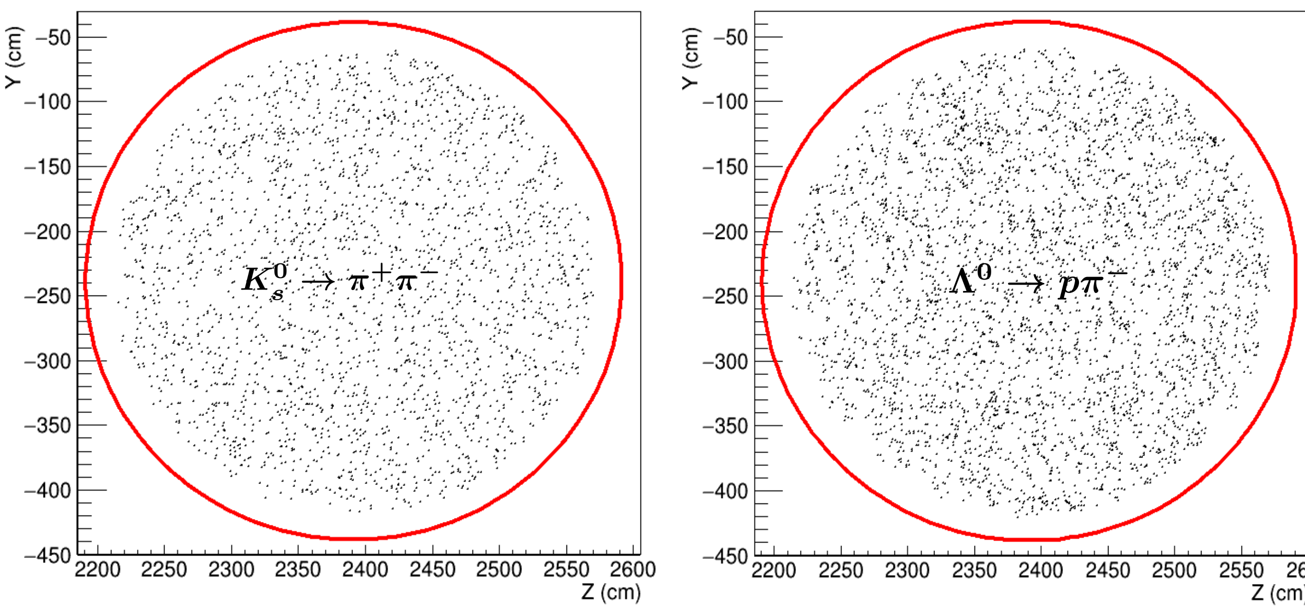

Figure 1.42: Distribution of $K_s^0 \to \pi^+\pi^-$ (left plot) and $\Lambda^0 \to p\pi^-$ (right plot) decays within the STT FV. The particles are originated from inclusive ν_μ CC interactions with the default FHC beam. The red circle represents the outer STT surface.

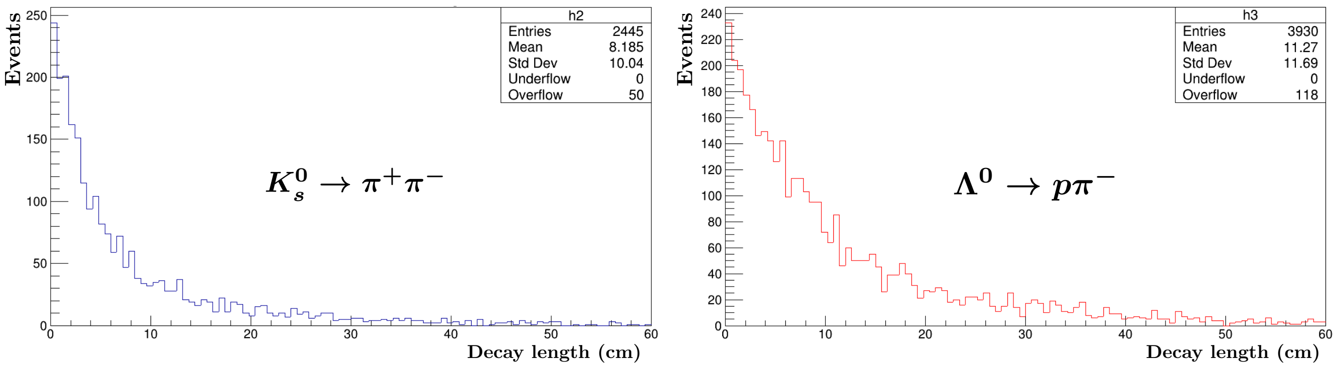

Figure 1.43: Decay length for the $K_s^0 \to \pi^+\pi^-$ (left plot) and $\Lambda^0 \to p\pi^-$ (right plot) reconstructed within the STT FV. The particles are originated from inclusive ν_μ CC interactions with the default FHC beam. A minimum number of 4 hits above threshold in the YZ bending plane is required.

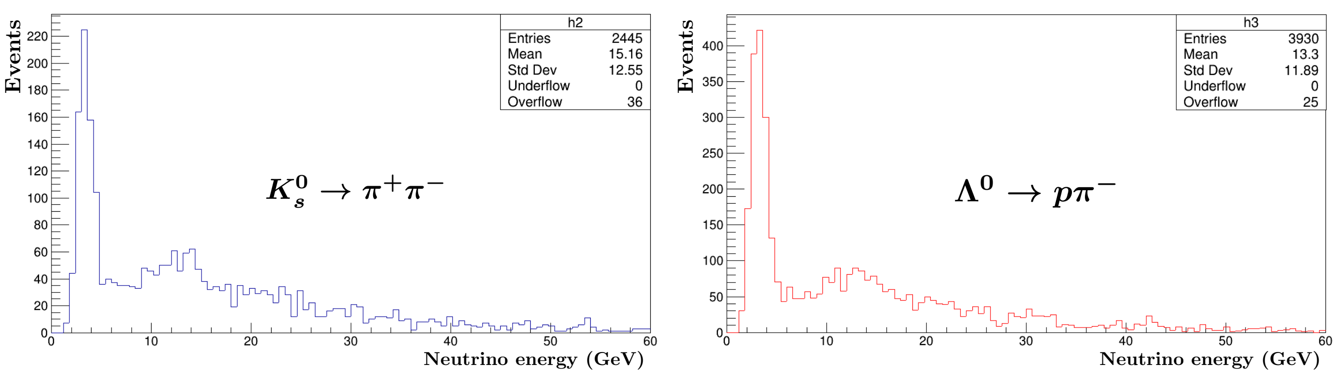

Figure 1.44: Neutrino energy for ν_μ CC interactions with a $K_s^0 \to \pi^+\pi^-$ (left plot) or $\Lambda^0 \to p\pi^-$ (right plot) decay reconstructed within the STT FV. A minimum number of 4 hits above threshold in the YZ bending plane is required.

$\pi^+\pi^-$ and $\Lambda^0 \to p\pi^-$ decays in ν_μ CC interactions. The mean decay length corresponds to about 8 cm for K^0_s and 11 cm for Λ^0. Most of the decays within the STT FV are reconstructed at distances from the primary vertex which are large compared to the expected vertex resolution (Fig. 1.70). The distribution of the neutrino energy for events with reconstructed $K^0_s \to \pi^+\pi^-$ and $\Lambda^0 \to p\pi^-$ decays is shown in Fig. 1.44. The high energy component of the spectrum is enhanced compared to inclusive CC interactions, since both the detected K^0_s and Λ^0 are originated from DIS interactions. Table 1.8 summarizes the fraction of $K^0_s \to \pi^+\pi^-$ and $\Lambda^0 \to p\pi^-$ decays which can be reconstructed within the STT FV with different requirements on the minimum number of hits in the YZ bending plane. The acceptance with ≥ 4 hits in the YZ plane is 94.6% for K^0_s and 92.8% for Λ^0 decays. It is remarkable that this latter number is dominated by the proton reconstruction and is remarkably similar to the corresponding proton reconstruction efficiency in RES interactions on H in Tab. 1.6.

Table 1.9 summarizes the total numbers of $K^0_s \to \pi^+\pi^-$ and $\Lambda^0 \to p\pi^-$ decays which can be reconstructed within the STT volume in both FHC and RHC beams. In addition to the inclusive CC and neutral current (NC) events originated in the STT FV, also the K^0_s and Λ^0 produced in CC+NC interactions in the magnet and ECAL surrounding the STT have been considered. Although only a small fraction of those particles has a decay vertex reconstructed in STT, the large mass of the magnet and ECAL still results in sizeable overall numbers.

Table 1.8: Fraction of V_0 decays originated from inclusive ν_μ CC interactions which can be reconstructed in STT for different requirements on the minimum number of STT hits in the YZ bending plane.

	Acceptance (%)	
Decay	≥ 4 YZ hits	≥ 6 YZ hits
$K^0_s \to \pi^+\pi^-$	94.6	91.3
$\Lambda^0 \to p\pi^-$	92.8	89.5

Table 1.9: Number of $K^0_s \to \pi^+\pi^-$ and $\Lambda^0 \to p\pi^-$ decays which can be reconstructed within the STT volume in both FHC and RHC default beams.

	$K^0_s \to \pi^+\pi^-$ in STT		$\Lambda^0 \to p\pi^-$ in STT	
Interaction type	≥ 4 YZ hits	≥ 6 YZ hits	≥ 4 YZ hits	≥ 6 YZ hits
FHC 5 year				
CC in STT FV	237,647	229,464	374,492	358,628
NC in STT FV	99,338	96,097	131,177	125,340
CC in magnet+ECAL	286,569	275,713	754,398	710,343
NC in magnet+ECAL	116,009	109,257	218,821	206,545
Total	739,563	710,531	1,478,890	1,400,860
RHC 5 year				
CC in STT FV	66,171	63,803	78,584	74,986
NC in STT FV	20,696	19,856	32,850	31,305
CC in magnet+ECAL	59,533	52,091	102,694	94,754
NC in magnet+ECAL	16,329	15,949	46,326	43,291
Total	162,729	151,699	260,454	244,336

1.10.2 Particle Identification

The identification of particles associated to the reconstructed tracks, or in general to the signals provided by the various SAND sub-detectors, is a crucial step in the complete event reconstruction, then for the full knowledge of the interacting neutrino properties.

Specifically, the STT combines a high resolution tracking with an efficient particle identification throughout its entire volume. The detector design was optimized for the reconstruction and identification of $e^\pm$ and γ since the most critical measurements in DUNE ND involve $e^\pm$: ν-e elastic scattering, ν_e ($\bar{\nu}_e$) CC, π^0/γ, etc.

The STT can efficiently identify $e^\pm$ using Transition Radiation, complemented by the ionization dE/dx in the active volume of the straws. Additional handles for $e^\pm$ identification are the matching of the momentum of charged tracks with the associated energy deposition and shower shape, both in ECAL.

The STT offers a 4π detection of photon conversions into e^+e^- pairs, which can be identified using the displaced V_0 vertex and the TR+dE/dx. The effect of the track bending in the magnetic field allows an excellent e/γ separation, while kinematic cuts on the invariant mass of the e^+e^- pair and on the corresponding opening angle can further enhance the purity. Overall, about 29.2% of photons convert within the STT volume.

The measurement of the energy loss dE/dx in the active gas within the straws crossed by the tracks also allows an identification of $\pi^\pm, K^\pm, p$ stopping hadrons. For protons, the measured range as a function of the momentum provides additional p/π separation.

Protons, kaons, pions stopping or slowing down in the STT or in the calorimeter can be identified through dE/dx, momentum/range relations, as well as ToF (Sec. **??**). For particles escaping the calorimeter, external muon catchers will allow to discriminate escaping muons fom pions.

In the following various studies of particle identification capabilities of the full system combining different sub-detectors will be described in details.

1.10.2.1 Electron Identification in STT

A unique feature of STT is the availability of Transition Radiation (TR) for the identification of $e^\pm$ with $\gamma > 1000$. Figure 1.45 shows that the use of TR in NOMAD provided a rejection factor of 10^3 for π with an $e^\pm$ efficiency of 90% or better [25]. Detailed simulations of the TR in the STT modules have been performed by using the code developed by P. Nevski at BNL for the ATLAS TRT detector. Tab. 1.10 summarizes the average number of TR photons detected in the straws for 10 consecutive STT modules equipped with radiators and a 5 mm CH_2 target plate. The presence of the 5 mm CH_2 target slab practically decouples individual STT modules since it absorbs most of the undetected TR photons exiting from the modules. The dependence of the number of TR photons detected in a STT module (average over 10 consecutive modules) from the electron energy is shown in Fig. 1.46.

Optimization of the STT Radiators for $e^\pm$ Identification

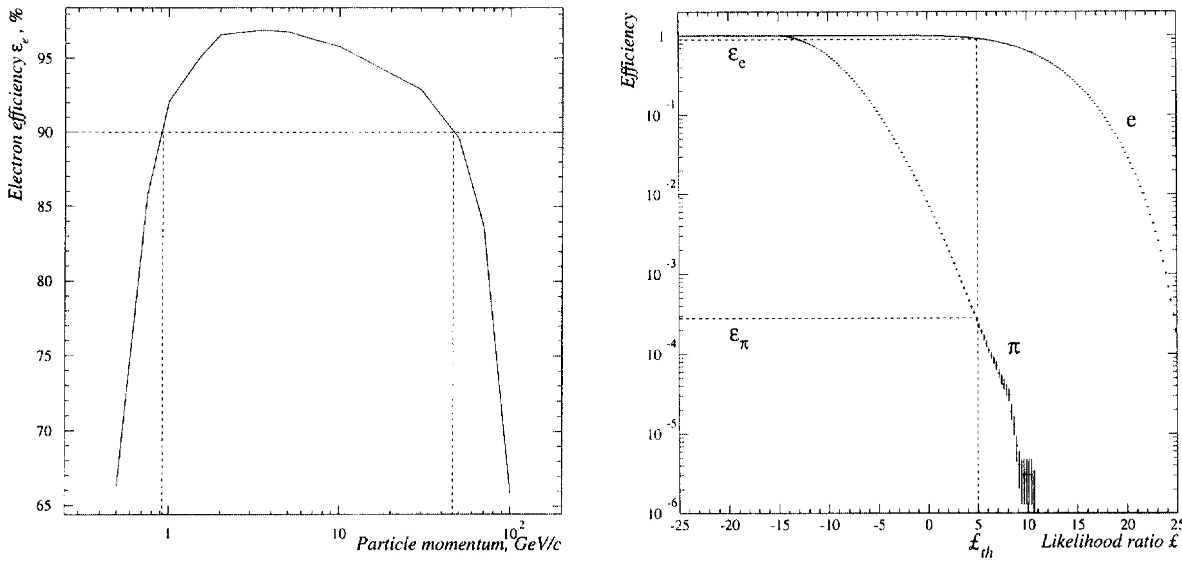

Figure 1.45: Electron identification with transition radiation (TR) in NOMAD. Left panel: $e^{\pm}$ efficiency as a function of momentum for a fixed π rejection factor of 10^{-3}. Right panel: $e^{\pm}$ and $\pi^{\pm}$ efficiencies as a function of the TR discriminant variable.

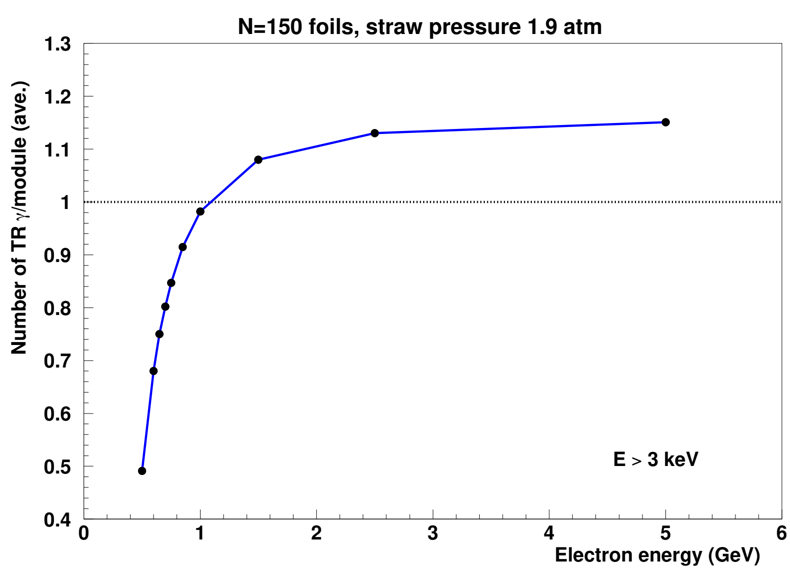

Figure 1.46: Number of detected TR photons in the straw tubes (averaged over 10 consecutive modules) as a function of the electron energy. The straw operating conditions assumed are a Xe/CO_2 gas mixture at 1.9 atm and an energy threshold of 3 keV is applied

Table 1.10: Average number of Transition Radiation photons detected in the straws (4 XXYY layers) for different energy thresholds. The result of the simulation of 10 consecutive STT modules equipped with radiators and a 5 mm CH_2 target plate is shown together with the corresponding total TR detected. The straw operating conditions assumed are a Xe/CO_2 70/30 gas mixture at 1.9 atm, with 150 CH_2 foils 15 μm thick separated by 120 μm air gaps.

	Electrons E=1.0 GeV			Electrons E=5.0 GeV		
Module #	> 3.0 keV	> 4.0 keV	> 5.0 keV	> 3.0 keV	> 4.0 keV	> 5.0 keV
1	0.93	0.89	0.80	1.09	1.04	0.94
2	0.97	0.93	0.84	1.13	1.08	0.98
3	0.98	0.94	0.85	1.15	1.10	1.00
4	0.99	0.95	0.86	1.16	1.11	1.01
5	0.99	0.95	0.86	1.16	1.11	1.01
6	0.99	0.95	0.86	1.16	1.11	1.01
7	0.99	0.95	0.86	1.16	1.12	1.01
8	0.99	0.95	0.86	1.16	1.12	1.02
9	0.99	0.95	0.86	1.17	1.12	1.02
10	0.99	0.95	0.86	1.17	1.12	1.02
Total	9.81	9.41	8.52	11.51	11.03	10.01

Table 1.11: Average number of Transition Radiation photons detected in the straws (4 XXYY layers) for different energy thresholds. The result of the simulation of 10 consecutive STT modules equipped with radiators and a 5 mm CH_2 target plate is shown together with the corresponding total TR detected. The straw operating conditions assumed are a Xe/CO_2 70/30 gas mixture at 1.9 atm, with 105 CH_2 foils 18 μm thick separated by 117 μm air gaps.

	Electrons E=1.0 GeV			Electrons E=5.0 GeV		
Module #	> 3.0 keV	> 4.0 keV	> 5.0 keV	> 3.0 keV	> 4.0 keV	> 5.0 keV
1	0.75	0.72	0.66	0.90	0.87	0.79
2	0.78	0.75	0.69	0.94	0.91	0.83
3	0.79	0.76	0.70	0.96	0.92	0.85
4	0.80	0.77	0.71	0.96	0.93	0.85
5	0.80	0.77	0.71	0.97	0.93	0.86
6	0.80	0.77	0.71	0.97	0.94	0.86
7	0.80	0.77	0.71	0.97	0.94	0.86
8	0.80	0.77	0.71	0.97	0.94	0.86
9	0.80	0.77	0.71	0.97	0.94	0.86
10	0.80	0.77	0.71	0.97	0.94	0.86
Total	7.92	7.65	7.03	9.57	9.24	8.49

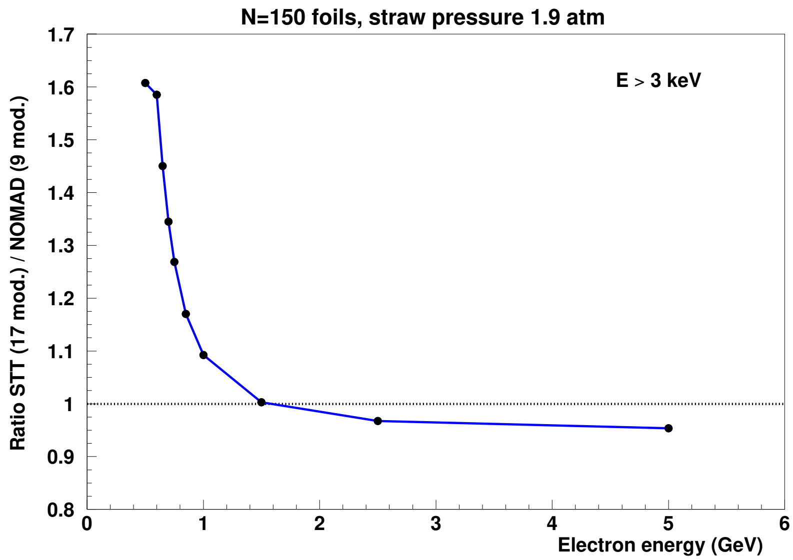

Figure 1.47: Ratio between the total number of TR photons detected in 17 consecutive STT modules and the corresponding one in the complete NOMAD transition radiator detector (9 modules) as a function of the electron energy. The straw operating conditions assumed for STT are a Xe/CO_2 gas mixture at 1.9 atm and an energy threshold of 3 keV is applied.

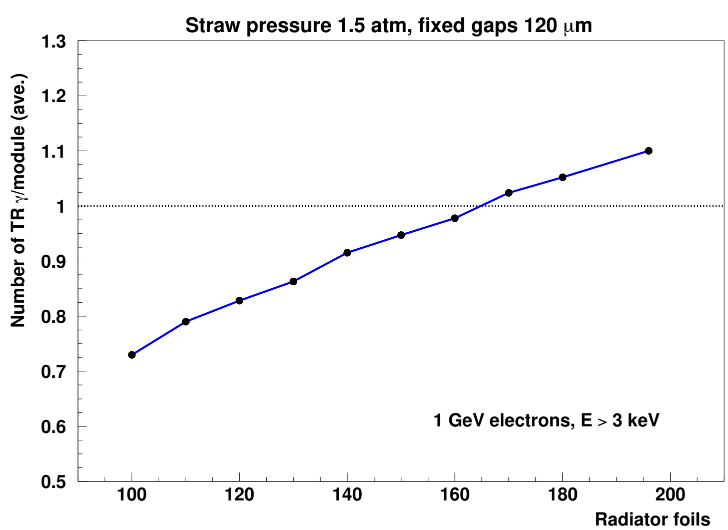

Figure 1.48: Number of TR photons detected per STT module (averaged over 10 consecutive modules) as a function of the total number of CH_2 foils in the radiator for 1 GeV electrons. A fixed air gap of 120 μm, 15 μm thick foils, a gas mixture Xe/CO_2 70/30 at 1.5 atm, and a threshold $E > 3$ keV are used.

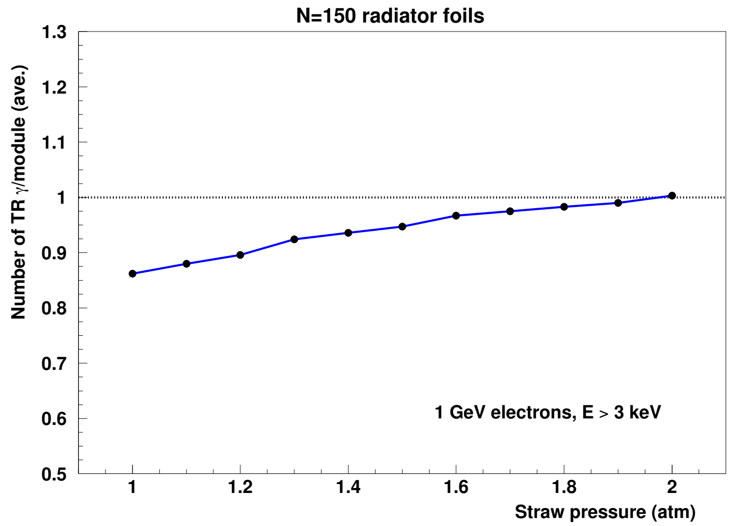

Figure 1.49: Number of TR photons detected per STT module (averaged over 10 consecutive modules) as a function of the operating gas pressure inside the straws for 1 GeV electrons. A fixed number of foils $N = 150$ 15 μm thick, air gaps of 120 μm, a gas mixture Xe/CO_2 70/30, and a threshold $E > 3$ keV are used.

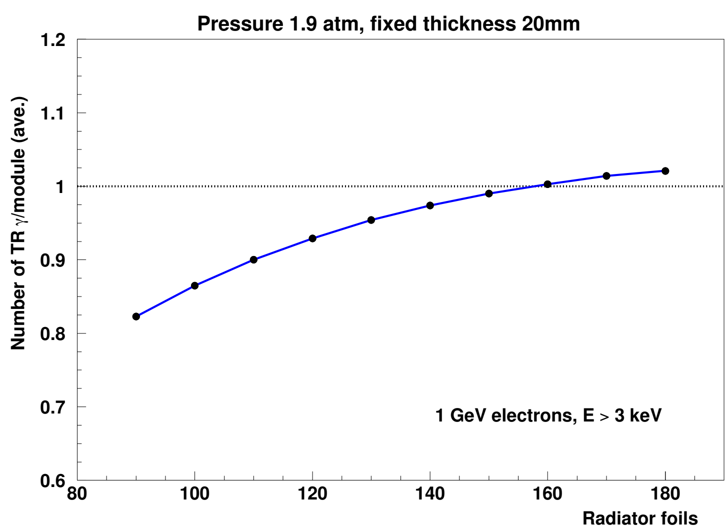

Figure 1.50: Number of TR photons detected per STT module (averaged over 10 consecutive modules) as a function of the total number of CH_2 foils in the radiator for a fixed total radiator thickness of 20 mm and 1 GeV electrons. The thickness of the air gaps varies according the number of foils used. A fixed foil thickness of 15 μm, a gas mixture Xe/CO_2 70/30 at 1.9 atm, and a threshold $E > 3$ keV are used

The radiators occupy a significant fraction of the space in the STT modules. The design of the radiators has to satisfy opposite requirements: (a) maximize the production of TR to guarantee an efficient electron ID; (b) minimize the total thickness of the STT modules in order to better exploit the limited space available inside the KLOE magnet.

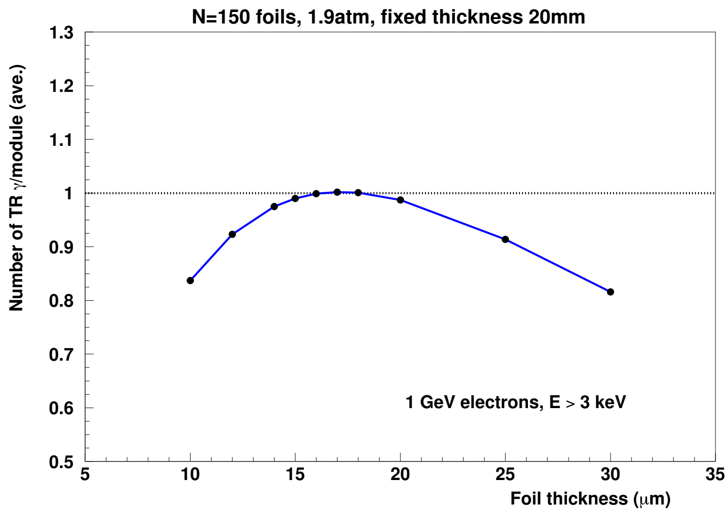

Figure 1.51: Number of TR photons detected per STT module (averaged over 10 consecutive modules) as a function of the thickness of the radiator foils for a fixed total radiator thickness of 20 mm and 1 GeV electrons. The thickness of the air gaps varies slightly according the thickness of the foils used. A fixed number of foils $N = 150$, a gas mixture Xe/CO_2 70/30 at 1.9 atm, and a threshold $E > 3$ keV are used.

Table 1.12: Comparison of the average number of Transition Radiation photons detected for different energy thresholds in NOMAD (9 modules) and in 20 consecutive STT modules. The STT operating conditions assumed are a Xe/CO_2 70/30 gas mixture at 1.9 atm, with CH_2 foils 18 μm thick separated by 117 μm air gaps.

	Electrons E=0.6 GeV			Electrons E=1.0 GeV			Electrons E=5.0 GeV		
Module #	>3.0 keV	>4.0 keV	>5.0 keV	>3.0 keV	>4.0 keV	>5.0 keV	>3.0 keV	>4.0 keV	>5.0 keV
NOMAD (9 mod.).	7.31	7.05	6.48	15.36	14.74	13.56	20.62	19.77	18.26
STT (20 mod.)	10.74	10.38	9.58	17.24	16.68	15.38	20.88	20.20	18.64
Ratio STT/NOMAD	1.47	1.47	1.48	1.12	1.13	1.13	1.01	1.02	1.02

A detailed optimization of the radiator design was performed by simulating the TR production by electrons of various energies. To this end, the TR performance is optimized using 1 GeV electrons, which are representative of the main oscillation peak expected in DUNE. For each radiator configuration 10 consecutive identical STT modules have been simulated to check build-up effects in the TR detection and to calculate the corresponding average response. The straw geometry is fixed, with 4 XXYY laters and a gas mixture of Xe/CO_2 70/30.

The first step is to select the minimal number of radiator foils (and hence the total radiator thickness) required to detect close to one TR photon per module. At this stage the air gaps between consecutive foils is fixed at 120 μm. Figure 1.48 shows that with $N = 150$ a relatively compact radiator of about 20 mm is produced, still retaining about 0.95 photons detected per

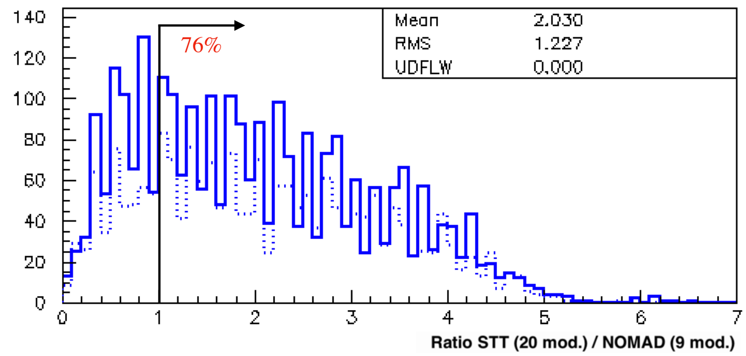

Figure 1.52: Ratio between the total number of Transition Radiation photons with $E > 3$ keV detected in 20 consecutive STT modules and the one in NOMAD (9 modules) for FHC ν_e CC (solid line) and RHC $\bar{\nu}_e$ CC (dotted line). The STT operating conditions assumed are a Xe/CO_2 70/30 gas mixture at 1.9 atm, with CH_2 foils 18 μm thick separated by 117 μm air gaps.

module. This latter number can be further increased by increasing the gas pressure inside thee straw to 1.9 atm (Fig. 1.49).

The second step of the optimization is to vary the thickness of both the air gaps and the radiator foils by keeping the total radiator thickness constant at about 20 mm. To this end, the air gaps are effectively varied by changing the number of radiator foils. As shown in Fig. 1.50, the TR response saturates for $N \geq 150$. Finally, when the thickness of the radiator foils is varied a clear peak in the TR response is visible for 15 $\mu m \leq \Delta \leq 18 \mu m$ (Fig. 1.51). Therefore the conclusion is that the optimal compromise (Tab. 1.10) for the radiator design is to have 150 foils 15 μm thick, separated by 120 μm air gaps, with straws operated at an internal pressure of 1.9 atm. An acceptable alternative (Tab. 1.11) allowing a more compact design of the STT modules would be to reduce the number of radiator foils to 105 18 μm thick with air gaps of 117 μm and the same straw operating conditions. Table 1.12 shows a comparison of the average numbers of TR photons detected with 20 consecutive STT modules in this latter configuration – corresponding to a track length of about 79 cm – with the equivalent numbers for the entire NOMAD detector. It is noteworthy to observe that this minimal track length is small compared to the size of STT. As shown in Fig. 1.52, about 76% of the leading electrons in FHC ν_e CC events result in a total number of TR photons detected in STT higher than in NOMAD. The performance of the electron ID in STT is therefore expected to be significantly better than in NOMAD.

1.10.2.2 Electron Identification in ECAL

The energy deposition and topological information in ECAL provide an additional electron identification capability, independent from the STT. The first step is to collect the energy depositions originated by electrons in ECAL. The bending of the electron track in the magnetic field can result in the emission of energetic Bremsstrahlung photons (Fig. 1.53) tangentially to the electron trajectory. Since the emitted photons may take most of the energy of the electron it is important to add their energy to the one deposited by the final electron track segment. To this end, we consider a vertical strip defined by the ECAL projection of the initial and final electron momenta, and collect all ECAL energy depositions within this Bremsstrahlung strip. The resulting total energy E in ECAL is consistent with the initial momentum p of the electron measured in STT as shown in Fig. 1.55. The ratio E/p provides a good electron/pion separation.

Various topological variables related to the structure of the electromagnetic showers in ECAL can also be used for electron identification. Figure 1.54 shows that the longitudinal profile of the energy deposition in the 5 ECAL layers is significantly different for electrons and pions. The energy measured in the initial ECAL layer is particularly important since electromagnetic showers result in an energy deposition larger than pions, which are largely consistent with minimum ionizing particles. Figure 1.55 shows the main variables used for electron identification in ECAL in addition to the longitudinal profile. We combine the following 13 variables into a ANN: (a) E/p; (b) fraction of total energy deposited in the layer 1; (c) fraction of total energy deposited in the layer 2; (d) fraction of total energy deposited in the layer 3; (e) fraction of total energy deposited in the layer 4; (f) fraction of total energy deposited in the layer 5; (g) asymmetry (max-min)/(max-min) in the energy fractions among the 5 layers; (h) energy deposited in the first layer; (i) maximal energy in a cell within the first layer; (l) total number of cells with deposited energy; (m) number of cells in the first layer; (n) number of cells in the last layer; (o) ratio between the energy deposited in the central cell and the one in the surrounding cells in the last layer. Figure 1.56 shows the distribution of the NN output for electrons and pions and the corresponding sensitivity as a function of the NN cut. An electron efficiency of 90% corresponds to a pion efficiency of about 6.4%.

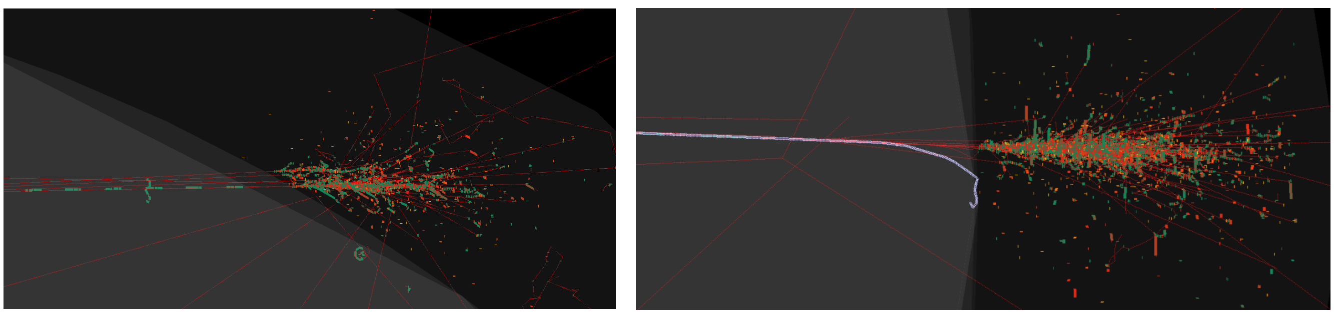

Figure 1.53: Examples of primary electrons with Bremsstrahlung photons detected in ECAL.

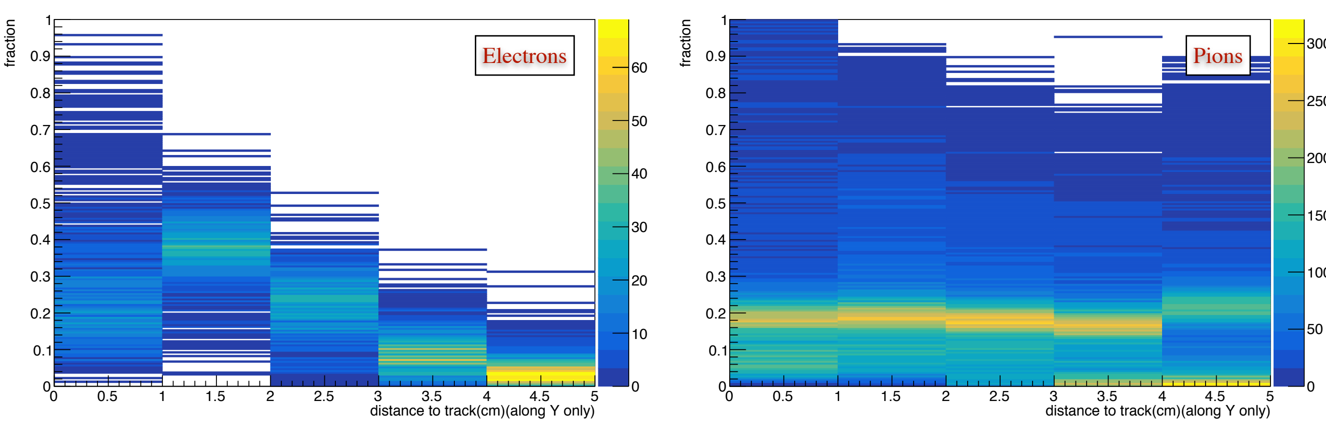

Figure 1.54: Longitudinal shower profile: fraction of the total shower energy reconstructed in each of the 5 ECAL layers for electrons (left plot) and pions (right plot).

1.10.2.3 Proton Identification

Proton Identification with dE/dx and Range Since the readout electronics of STT provides precise detector hit charge and time measurements for each straw (Sec. 1.5.1.6), the energy loss

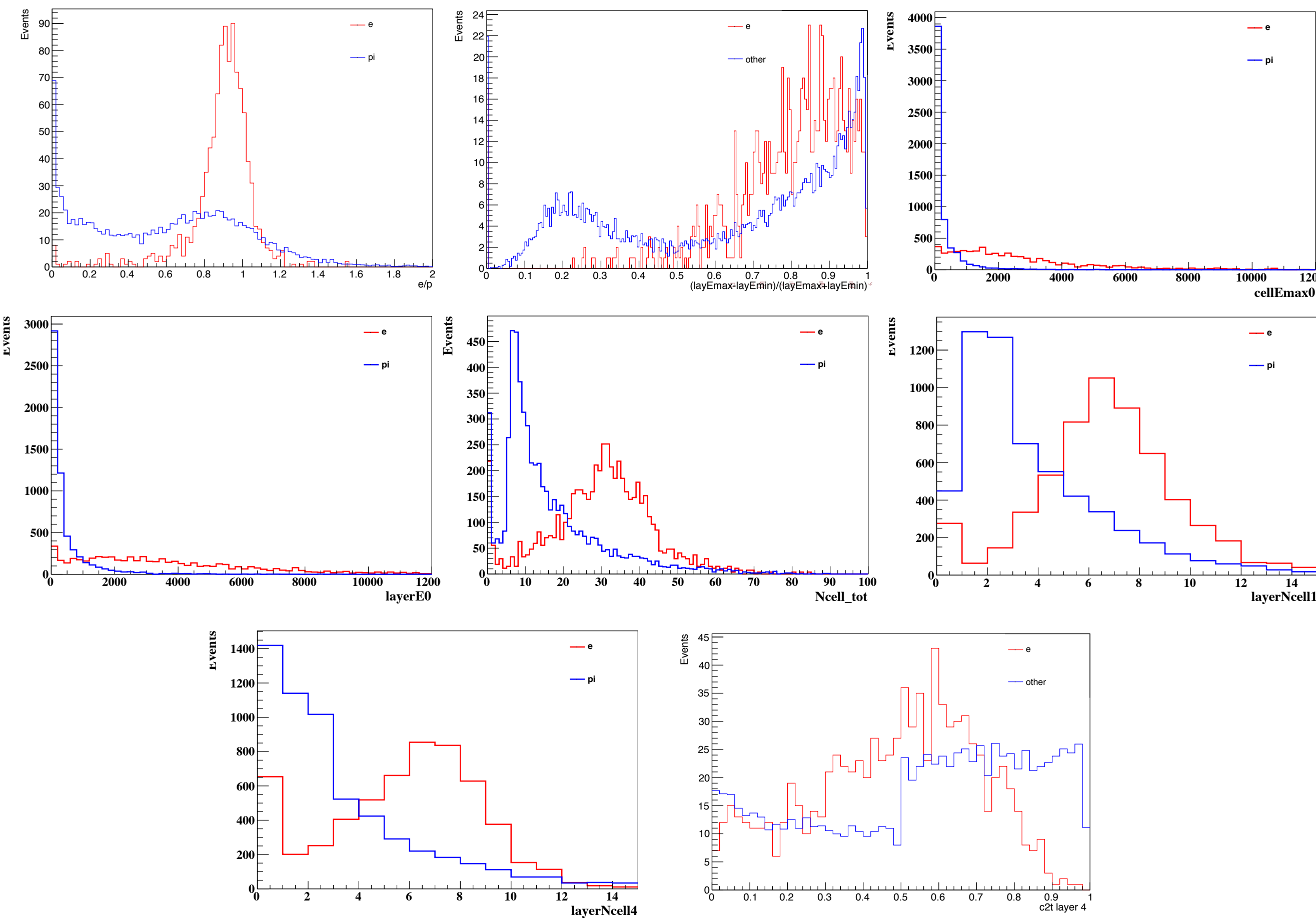

Figure 1.55: Distributions of ECAL variables used as ANN input for electron/pion separation.

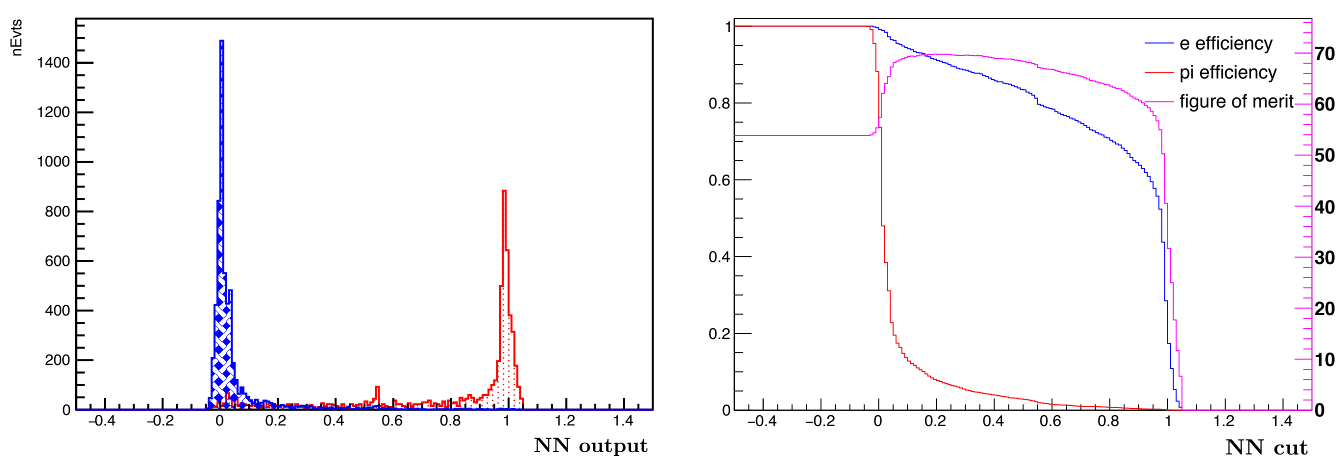

Figure 1.56: Left plot: distribution of the NN output for electron identification in ECAL for electrons (red signal) and pions (blue background). Right plot: electron/pion efficiency and figure of merit $\sqrt{S/(S+B)}$ as a function of the NN cut.

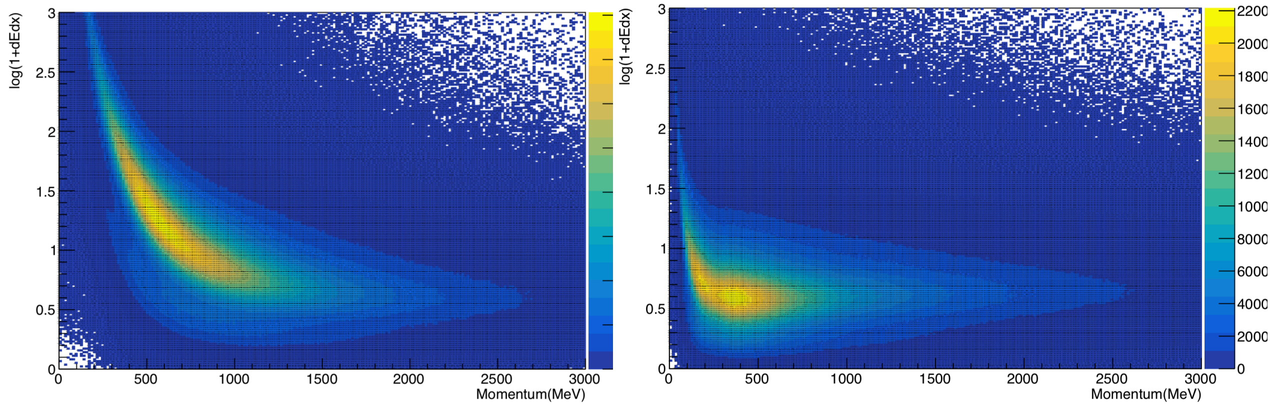

Figure 1.57: Distribution of $\log(1 + dE/dx)$ as a function of the momentum for protons (left plot) and pions (right plot) in STT. The energy deposition in the gas mixture Xe/CO_2 (or Ar/CO_2 for modules with graphite targets) of each straw crossed by the particle is used. Reconstruction effects are taken into account in the plots.

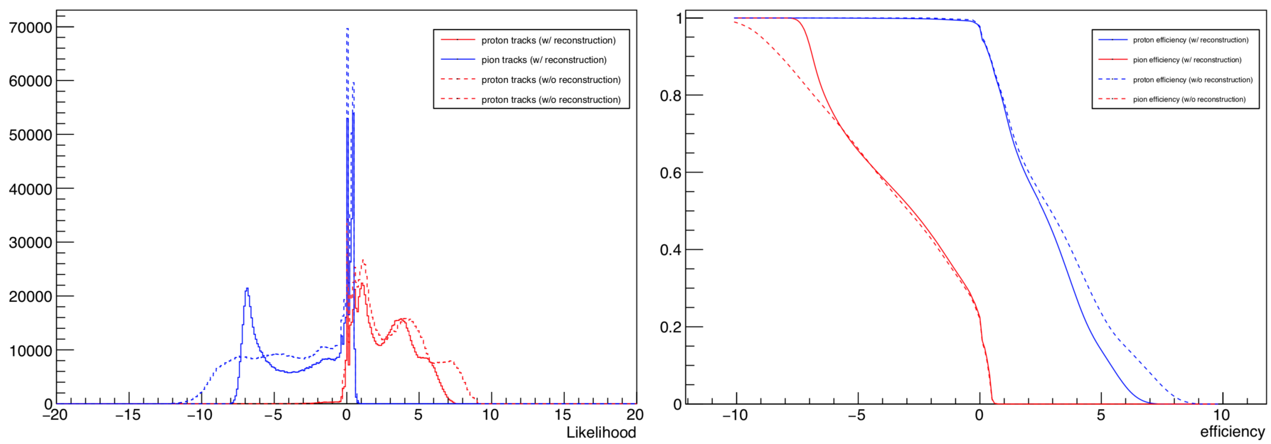

Figure 1.58: Left plot: distributions of the logarithm of the average likelihood ratio, $\ln \lambda^{p/\pi}_{dE/dx}$, between the proton and pion hypotheses corresponding to the binned 2D distribution dE/dx vs momentum (Fig. 1.57). The values shown are averaged over all the hits associated to each track. Right plot: proton and pion efficiencies as a function of the cut on the average $\ln \lambda^{p/\pi}_{dE/dx}$ with (solid lines) and without (dashed lines) reconstruction effects.

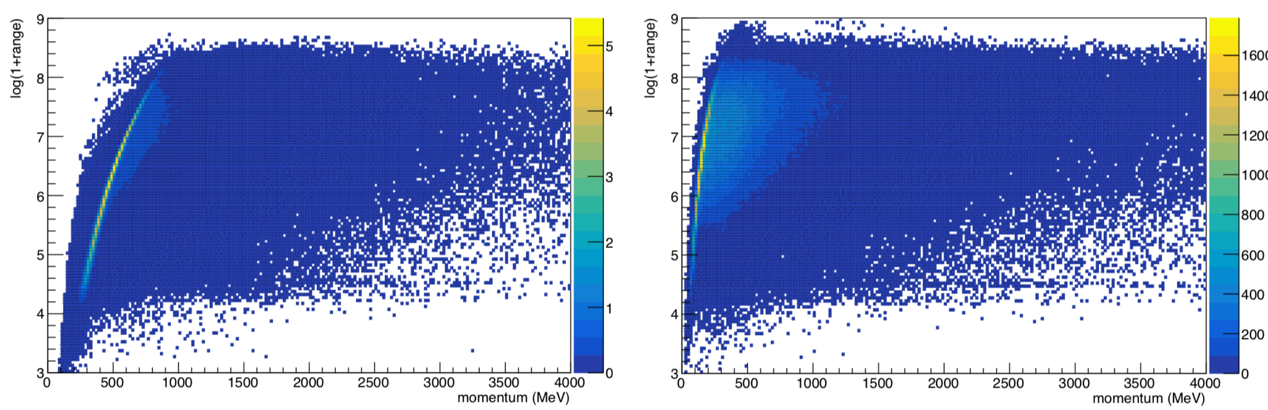

Figure 1.59: Distribution of $\log(1 + \text{range})$ as a function of the momentum protons (left plot) and pions (right plot) in STT. The range includes the various passive targets.

dE/dx inside the gas – Xe/CO_2 70/30 for radiator modules and Ar/CO_2 70/30 for modules with nuclear targets, with an internal pressure of about 1.9 atm (Sec. 1.5.1) – can be used for particle identification. To this end, the independent measurements of the energy deposition in each of the straws crossed by the particle can be combined thus enhancing the discriminating power. In this section, the proton/pion separation achievable using the energy loss dE/dx in the gas of the straws are studied. While protons deposit, on average, a much larger energy in the straws compared to other particles, they also cross fewer straws, thus providing a smaller number of independent dE/dx measurements.

About 350k inclusive ν_μ CC interactions randomly distributed within the STT volume Were simulated using GENIE+GEANT4 with a detailed implementation of the detector geometry. Protons and pions with reconstructed momentum were selected by requiring a minimum number of four hits (crossed straws) in the bending YZ plane (Sec. 1.10.1.7). Both the momentum and the dE/dx are smeared to take into account the expected experimental resolutions. Figure 1.57 shows the distribution of the resulting dE/dx as a function of the measured momentum for all straws crossed by protons and pions. A clear separation is visible in spite of the relatively large fluctuations associated to a single measurement in an individual straw. We use the 2D distributions in Fig. 1.57 to build binned likelihood functions for the proton and pion hypotheses and use the logarithm of their ratio, $\ln \lambda^{p/\pi}_{dE/dx}$, as discriminant. Figure 1.58 (left plot) shows the distribution of the $\ln \lambda^{p/\pi}_{dE/dx}$ for independent samples of protons and pions, averaged over all the hits (crossed straws) associated to the considered tracks. The proton and pion efficiencies obtained with a cut on the average $\ln \lambda^{p/\pi}_{dE/dx}$ are also illustrated in Fig. 1.58 (right plot). With a 90% proton efficiency we obtain a pion efficiency of about 7.5%, while with a proton efficiency of 87% the pion efficiency drops to less than 1%.

Additional p/π separation can be obtained by analyzing the range (total track length) of the particles within the STT tracking volume. This quantity is partially correlated with the average dE/dx since larger energy depositions correspond to a shorter range. However, while the dE/dx measurement only takes into account the direct energy depositions inside the straw gas, the particle range is dominated by the amount of passive material (CH_2 and C targets) crossed by the particles. Figure 1.59 shows the distribution of the range as a function of the measured momentum for protons and pions. Similarly to the procedure used for dE/dx, these 2D distributions were used to build binned likelihood functions for the proton and pion hypotheses and calculate the logarithm of their ratio, $\ln \lambda^{p/\pi}_{range}$. Since the dE/dx and range measurements are partially correlated, the 2D distribution of $\ln \lambda^{p/\pi}_{range}$ vs. $\ln \lambda^{p/\pi}_{dE/dx}$ is used as combined discriminant. Figure 1.60 shows the efficiencies obtained from the combined dE/dx and range information for protons and pions. With a 90% proton efficiency, a pion efficiency of about 5.5% is obtained.

The results discussed above are obtained with binned likelihood functions based on the 2D distributions of dE/dx and range as a function of the momentum. Further improvements can be obtained by using the unbinned likelihood calculated from the parameterized function describing the expected energy loss. Studies with the unbinned likelihood are currently ongoing.

Proton Identification with time-of-flight and ECAL The performance of the proton identification based on dE/dx and range in STT can be further improved by considering the time-of-flight measurement and, for the tracks reaching ECAL, the corresponding nformation. The time-of-flight

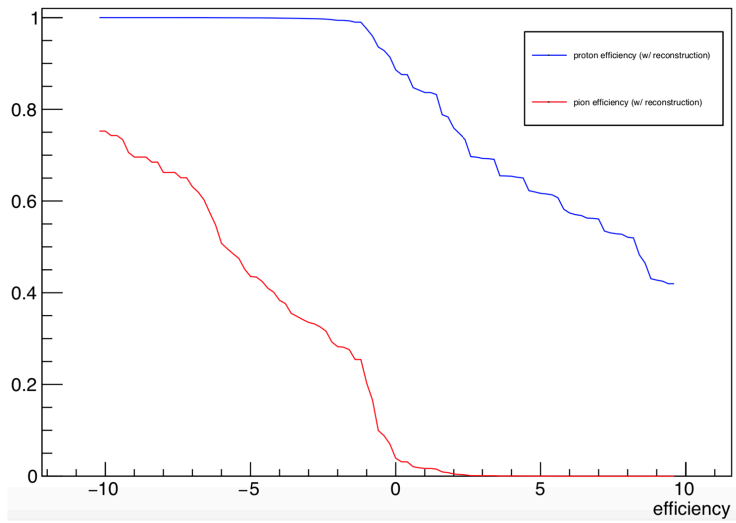

Figure 1.60: Proton and pion efficiencies as a function of the cut on the $\ln \lambda^{\mathrm{ID}}$ combining both the dE/dx and the range information.

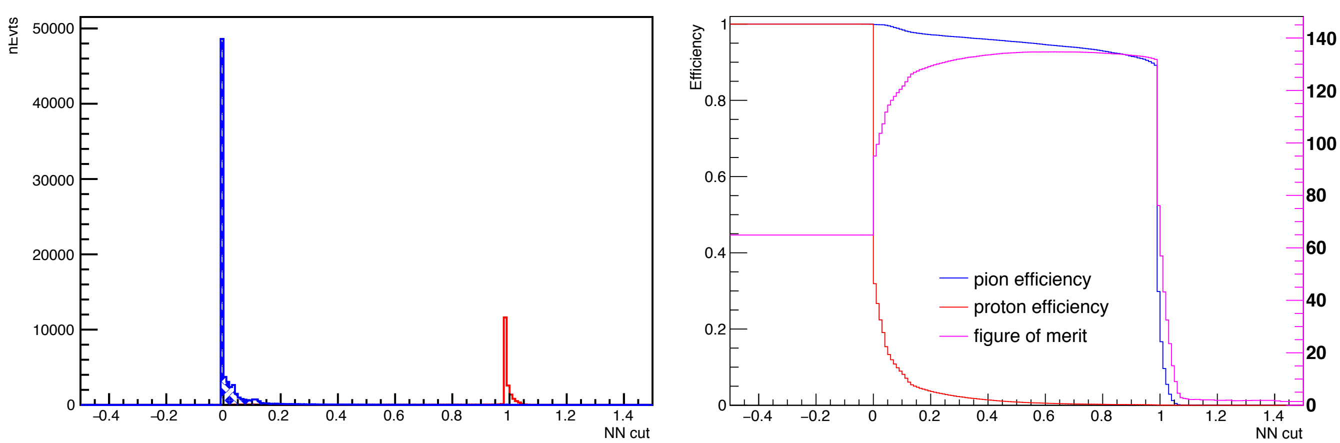

Figure 1.61: Distribution of the NN output for proton identification (left plot) and corresponding sensitivity as a function of the NN cut (right plot).

(ToF) is obtained from the time difference between the primary vertex and the last hit of the track (either in STT or ECAL), properly smeared with the corresponding time resolutions. From the ToF and the total length of the track in space we obtain the $\beta = v/c$ of the charged track considered. The mass of the particle can then be determined from the momentum measured in STT as $m = p/(\beta\gamma)$. We combined the following 7 variables into a ANN: (a) $\ln \lambda^{p/\pi}_{dE/dx}$ from dE/dx as described above; (b) total range; (c) momentum measured in STT; (d) β; (e) reconstructed mass m; (f) flag determining if the track reaches ECAL; (g) maximal number of cells in ECAL. Figure 1.61 shows the distributions of the corresponding NN output for protons and pions. With a 90% proton efficiency we obtain a pion efficiency of about 1.1%. The same NN can be used to veto protons in the kinematic tagging of the leading CC leptons described in Sec. 1.11.1.1. For this application, a proton efficiency of 0.7% with a muon efficiency of 95% (Fig. 1.61) is obtained.

1.10.2.4 Muon Identification

Muon Identification using STT and ECAL An efficient identification of both μ^+ and μ^- is required to select various CC processes in the FHC and RHC beams. A study of the muon/pion separation capability using about 500k inclusive ν_μ CC interactions randomly simulated within the STT volume using GENIE+GEANT4 was performed. The goal is twofold: to evaluate the performance achieved by matching STT charged tracks with the ECAL energy depositions, and to outline the requirements for an external muon identifier for the remaining unidentified particles.

Table 1.13: Summary of $\mu^\pm$ selection for different types of events in the STT fiducial volume. See text for details.

Cut	FHC ν_μ CC	FHC NC	RHC $\bar{\nu}_\mu$ CC
No cut	100.0 %	100.0 %	100.0 %
No interaction/kink in STT	100.0 %	55.4 %	100.0 %
Tagged μ candidate	99.1 %	–	99.3 %
Tagged h candidate	0.9 %	18.8 %	0.7 %
Tagged track reaches ECAL	98.7%	18.8 %	99.0 %
Tagged track reaches outer yoke	69.8 %	0.3 %	86.4 %

Firstly, μ^-, π^-, and π^+ primary tracks reconstructed in STT and matched to an energy detected above 1.1 photoelectrons in the barrel ECAL are selected. Then the charged tracks are required not to have large kinks from scattering within the STT volume. Figure 1.62 shows the distribution of the outermost ECAL layer with a detected energy deposition above threshold. Most muons cross all 5 layers and exit from the outer ECAL surface, while a significant fraction of pions stop or interact within the first 4 ECAL layers. The charged tracks are subdivided in two categories: (i) tracks reaching the outermost layer 4; (ii) tracks stopping or interacting in layers 0-3. For both samples, the pions crossing all 5 ECAL layers without interacting are initially disregarded and the focus is put on the ones either stopping or interacting in ECAL. The identification algorithm starts from the first sample and 10 discriminant variables are selected: (a) maximal energy in a cell; (b) asymmetry in the cell energy (max-min)/(max+min); (c) total number of cells; (d) mean energy among the 5 layers; (e) RMS of energy among the 5 layers; (f) asymmetry in layer energy (max-min)/(max+min); (g) energy in outermost layer 4; (h) maximal energy in layers; (i) minimal energy in layers; (l) maximal number of cells in layers. Figure 1.63 shows the distributions of these variables for muon and pion tracks. The 10 variables are combined into an ANN and this is trained with all muon tracks (signal) and with the sub-sample of pions stopping or interacting in ECAL (background), as illustrated in Fig. 1.64. The tracks with NN>0.28 are selected as muon candidates, with an efficiency of 98% for actual muons and 7.5% for pions (Fig. 1.65).

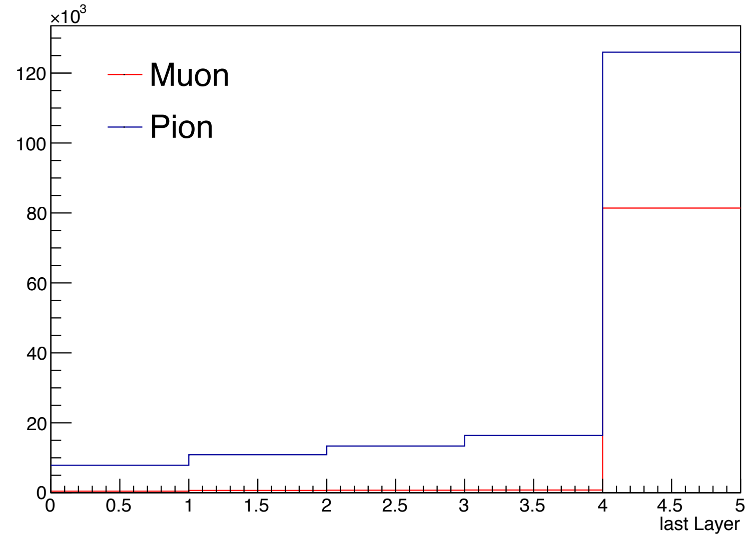

Figure 1.62: Distribution of the outermost ECAL layer with detected energy above 1.1 photoelectrons for pion and muon tracks.

A similar procedure is applied for the second sample of tracks stopping or interacting within the first 4 ECAL layers. The following 8 discriminant variables are combined into an Artificial Neural Network (ANN): (a) maximal energy in a cell; (b) total number of cells; (c) mean energy among the layers; (d) asymmetry in layer energy (max-min)/(max+min); (e) maximal energy in layers; (f) minimal energy in layers; (g) range inside ECAL; (h) reconstructed momentum in STT. Figure 1.64 shows the ANN output. The cut NN>0.49 is selected, based on the global sensitivity $S/\sqrt{S+B}$, including the events from the other sample passing the cut in layer 4 (Fig. 1.65). The combined muon efficiency is 98% and the pion efficiency is 10.9%. So far, the pions crossing all the 5 ECAL layers – total thickness about one interaction length λ – without interacting were ignored. Figure 1.66 shows the distribution of the layer 4 NN output for this sample. The same NN cut above rejects about 43% of this pion sample, mainly due to the energy deposition in the ECAL layers. The total fraction of pions passing the NN selection in ECAL is 23.7%.

1.10.2.5 Muon/Pion Separation

External muon tagger In order to reject the pions surviving the ECAL identification we plan to instrument the 5 cm gap available between the external cryostat wall and the magnet yoke, as well as to add an external muon identifier (EMI) outside of the yoke. Figure 1.67 shows that minimum energies of about 350 MeV and 800 MeV are required for the muon to reach the inner and outer yoke surfaces, respectively. Only a fraction of 0.3% of the tagged hadrons in NC interactions can reach the outer yoke surface (Tab. 1.13), while this fraction raises to 69.8% and 86.4% for the leading $\mu^{\pm}$ in ν_μ and $\bar{\nu}_\mu$ CC, respectively. The tracks emerging from the outer yoke are characterized by relatively small angles with respect to the original beam direction, as illustrated in Fig. 1.68. The corresponding exit points of these tracks are located mainly in the forward region (Fig. 1.68), as the magnet yoke effectively filters out low energy tracks emitted at large angles. As a result, the

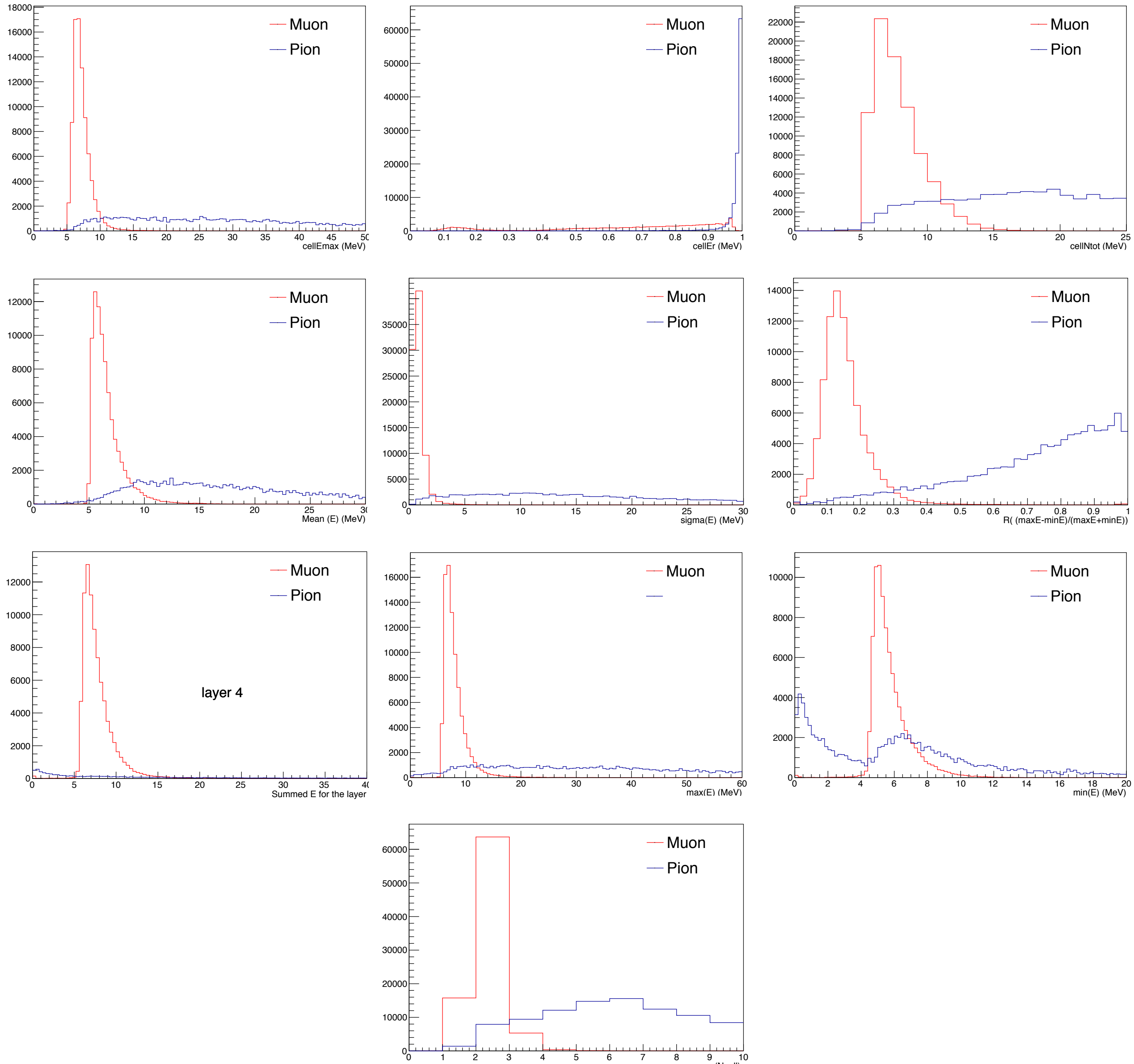

Figure 1.63: Distributions of variables used as ANN input form muon (red) and pion (blue) tracks reaching layer 4 in ECAL. Only pions stopping or interacting are considered. See text for details.

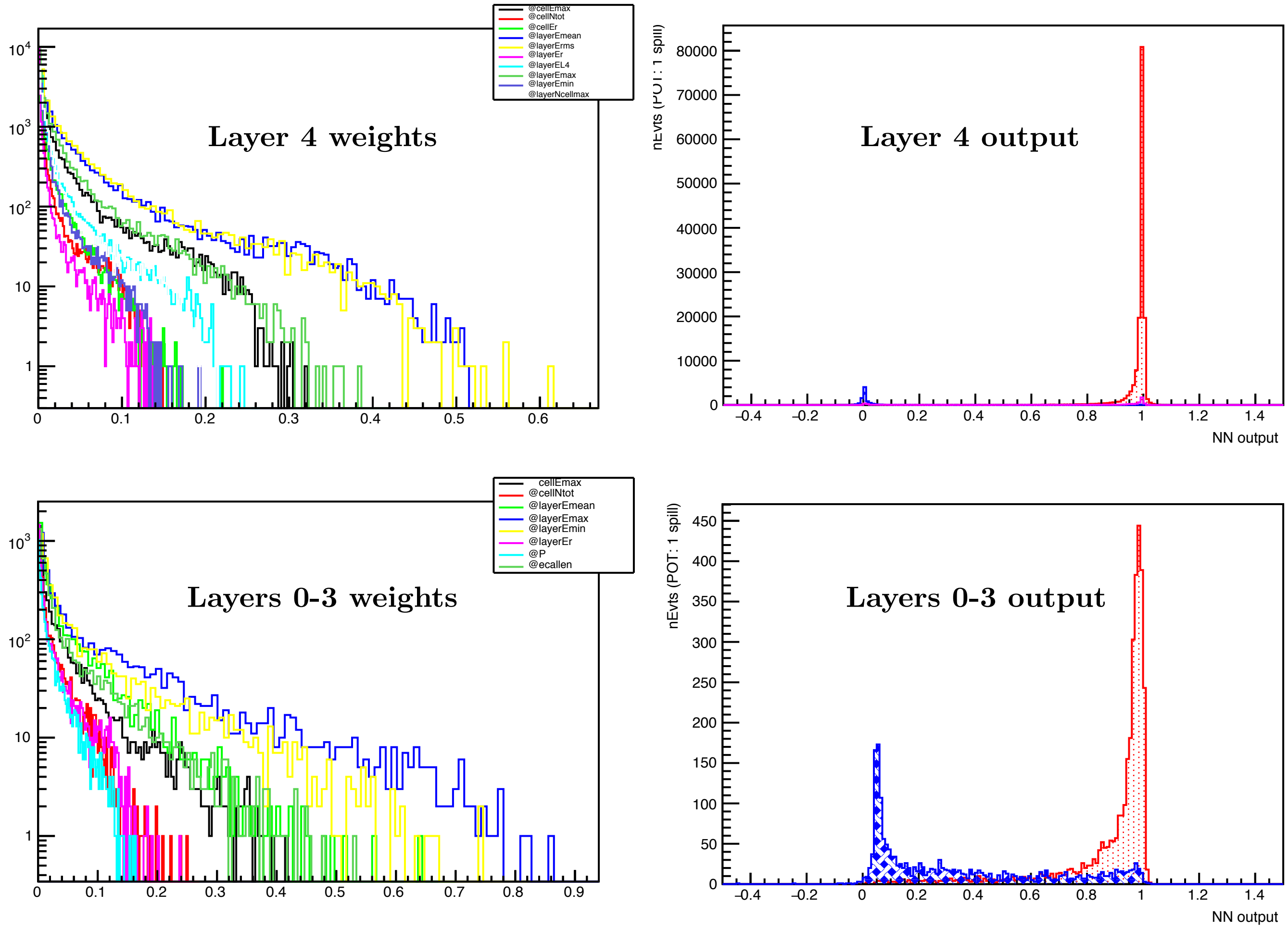

Figure 1.64: Weights of ANN variables (left plots) and ANN output (right plots) for muons and pions with outermost energy in layer 4 (top plots) and for the ones stopping or interacting in layers 0-3 (bottom plots).

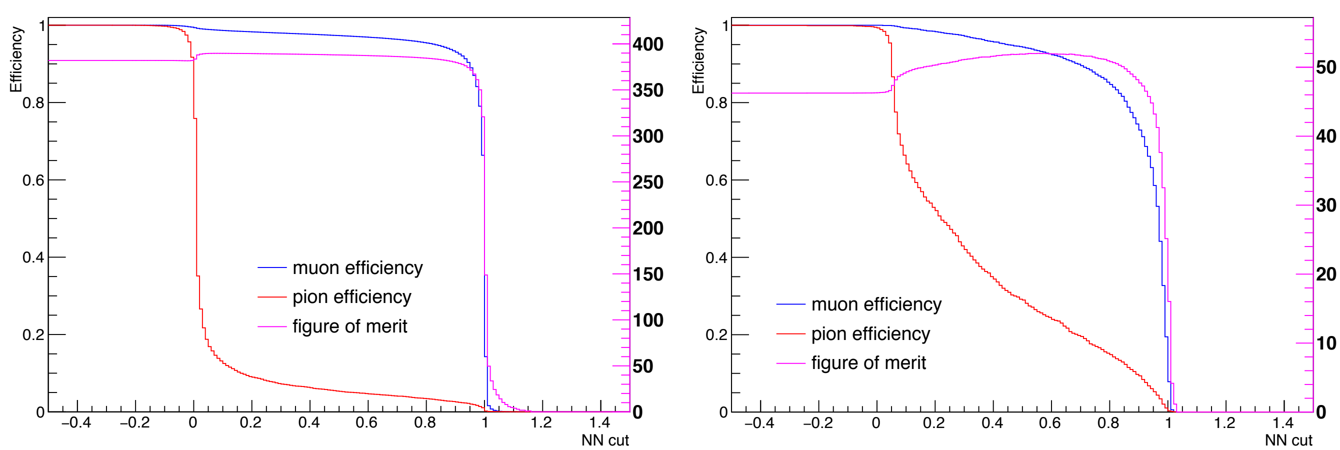

Figure 1.65: Muon and pion efficiencies and sensitivity $S/\sqrt{S+B}$ as a function of the NN cut for tracks with outermost energy in layer 4 (left plot) and the ones stopping or interacting in layers 0-3 (right plot).

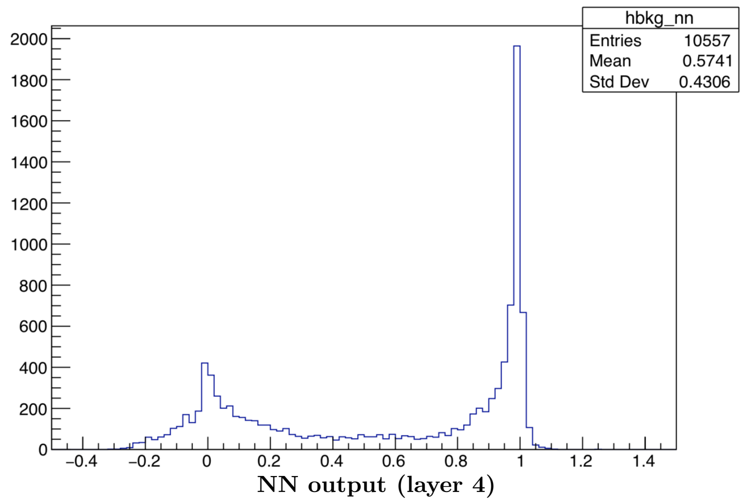

Figure 1.66: Distribution of the ANN output for the sample of pions crossing all 5 ECAL layers without interacting.

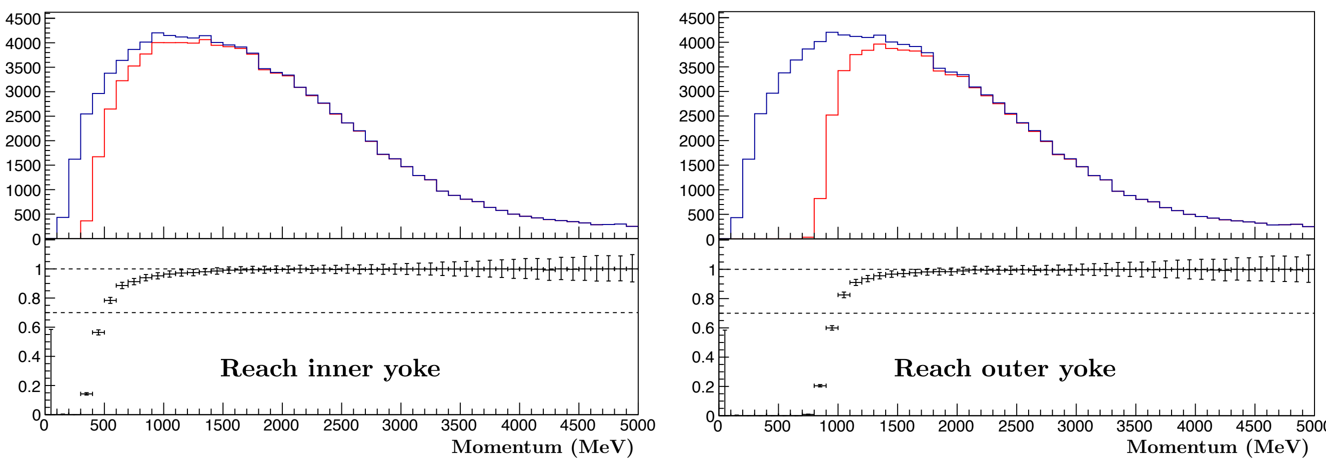

Figure 1.67: Acceptance of muon tracks passing the ECAL identification to reach the inner (left plot) and outer (right plot) surfaces of the magnet yoke. See text for details.

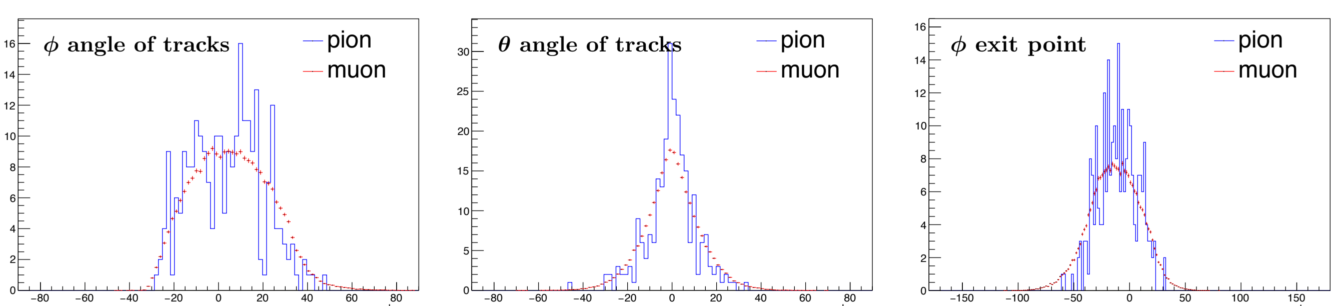

Figure 1.68: Distributions of the ϕ angle (left plot) in the YZ plane, the θ angle (middle plot) along the X axis, and of the ϕ exit point (right plot) for tracks reaching the outer surface of the magnet yoke.

design of the external muon identifier can be simplified. Dedicated simulation studies are ongoing in order to optimize the performance of this system.

1.10.3 Neutrino Interaction Identification in the Spill

1.10.3.1 Expected Rates per Spill

1.10.3.2 Event Separation inside the Spill

1.10.4 Event Reconstruction in GRAIN

1.10.4.1 Vertex Reconstruction

1.10.4.2 Multiple Track Reconstruction

1.10.4.3 Energy Deposit Reconstruction

1.10.5 Tracker and CC Acceptance for Muons, Protons, Pions

1.10.6 Event Reconstruction in STT

A full realistic event reconstruction is based only on detected quantities, avoiding to use MC *true* information (vertex position, number and nature of generated particles, trajectories, and so on). This full reconstruction has been performed on samples simulated with the FLUKA code, assuming the DUNE-neutrino beam and interactions both in the LAr target (GRAIN) and in the STT volume. As a preliminary step of this reconstruction procedure, a coarse STT *digitization* has been implemented, where the MC hits are simply grouped together by taking into account their position, thus getting a single digit for each straw tube of $x - z$ and $y - z$ layers. In this phase, position and time are assigned to the *STT digits* assuming a spatial resolution of 200 μm and a time spread of $\sim 1ns$.

After such digitization, a first rough reconstruction of the neutrino-interaction vertex is performed, on both views separately, based on topology criteria, that is on the spread profile of the STT-digits normalised to the digit-number as a function of the layer z-coordinate. When the minimum spread position is found into an internal STT layer (not the two upstream layers), it is taken as a first estimate (*step 0*) of the interaction vertex which is then assumed to be located inside the tracker volume. On the contrary, if the position of the minimum spread in STT-digit coordinates is located in the two upstream STT-layers, the neutrino interaction vertex probably occurred inside the GRAIN volume. In this case, its position is estimated at *step 0* by the backward extrapolation along z-axis up to the central z coordinate of GRAIN.

Such preliminary vertex position estimate is then used for the subsequent track-finding algorithm which consists in a global algorithm based on the coordinate transforms. In the $y - z$ view the transforms are

$$z \to u = \frac{+z - z_V}{(z - z_V)^2 + (y - y_V)^2} \qquad y \to v = \frac{-y + y_V}{(z - z_V)^2 + (y - y_V)^2}$$

where z_V and y_V are the coordinates of the previous reconstructed vertex in that view. Similar transforms are also used in the $x - z$ view. In the transformed-coordinate plane, the curved trajectories originating in (z_V, y_V) or in (z_V, x_V) become straight lines crossing the origin $(u, v) =$

$(0, 0)$. Thus, the 2-dimensional track-finding in each view becomes a 1-dimensional search for the peaks on the distribution of the variable $\phi = atan(v/u)$. Each peak is related to a track, thus allowing the association of the STT-hits to the particle trajectories. Then the hits related to a possible track are fitted in each view. More precise the vertex reconstruction is, more easily the ϕ-peaks will be identified, then better will be the track-hits association and the resulting track fit.

After the fit of the tracks, a new (*step 1*) estimate of the interaction vertex is obtained from the crossing of the couple of tracks with greatest rigidity. Fig. 1.69 shows the uncertainty on the vertex reconstruction in the $x - z$ view and in the space (from both the views) at *step 0* and *step 1*. A clear improvement (lower mean value, more events with distance within 5 cm) is visible at *step 1* where the rigid-tracks crossing is used. The uncertainties on the different axes are shown in Fig. 1.70.

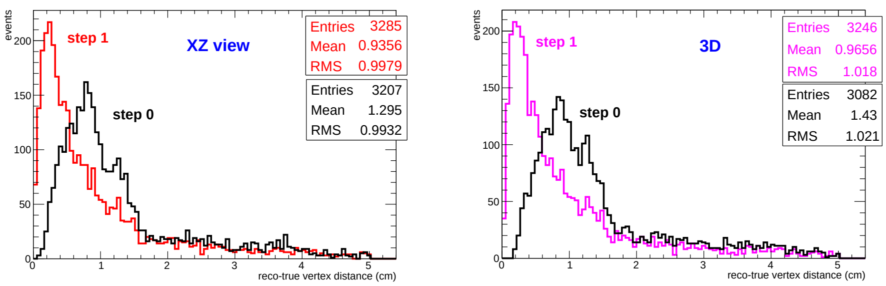

Figure 1.69: Fluka simulation, STT target - Uncertainty on the vertex reconstruction at *step 0* and *step 1*. Left panel: $x - z$ view. Right panel: 3-dimensional space.

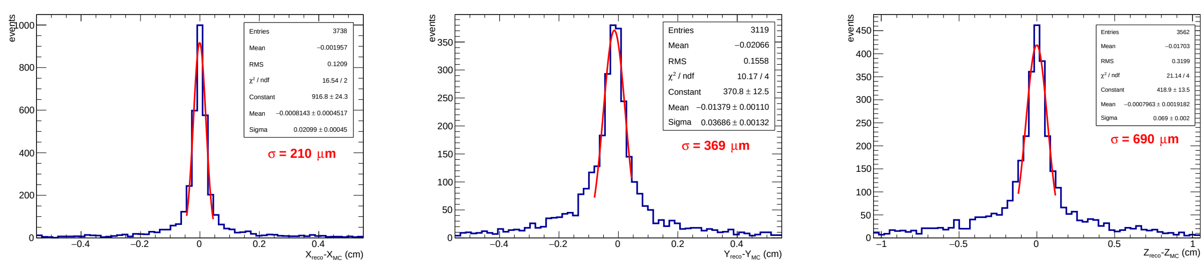

Figure 1.70: Fluka simulation, STT target - Uncertainty on the vertex reconstruction at *step 1* on x, y and z axes.

As an example to illustrate the procedure, Fig. 1.71 includes a MC event with a neutrino resonant interaction in the STT radiator: in the left panels, the full MC event in the $y - z$ and $x - z$ views is shown, while the right panels show the same event as it appears after STT-hit digitisation.

For such an event, the vertex is well reconstructed since *step 0*, thus allowing a good identification of ϕ peaks and the proper hits-track association, as illustrated in the plots of Fig. 1.72. The three charged-particle tracks in the event are clearly fully reconstructed (the fit parameters are also reported in the left bottom plot).

In Fig. 1.73, the number of tracks reconstructed in each view through the above described procedure is compared with the *true* multiplicity of charged particle tracks (requiring at least three STT-hits), for the LAr-target interaction sample. In particular, the right plot refers to the sub-sample

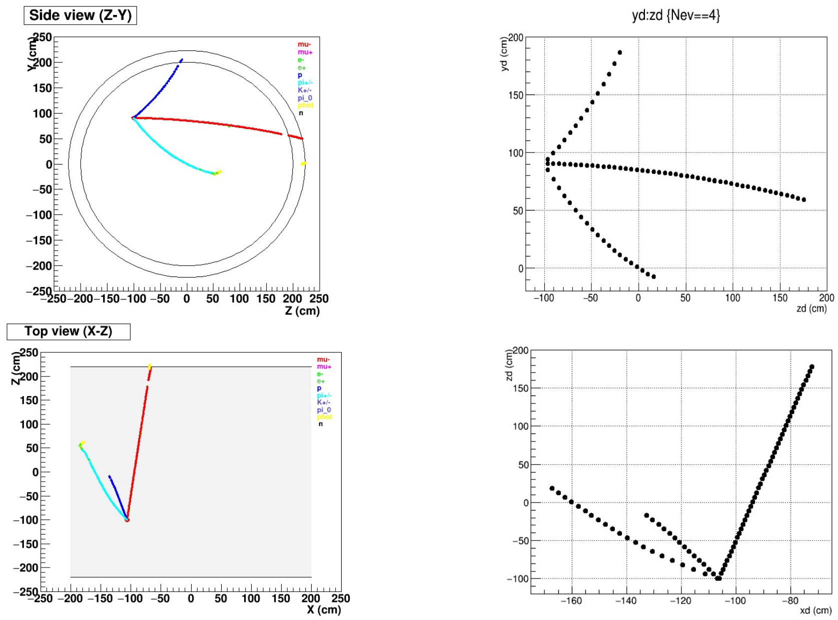

Figure 1.71: Fluka simulation - Event with a muon-neutrino resonance interaction in the STT radiator as it appears in the MC display (left upper and lower panels) and after STT-hit digitisation in the $y-z$ (right upper panel) and $x-z$ (right lower panel) view.

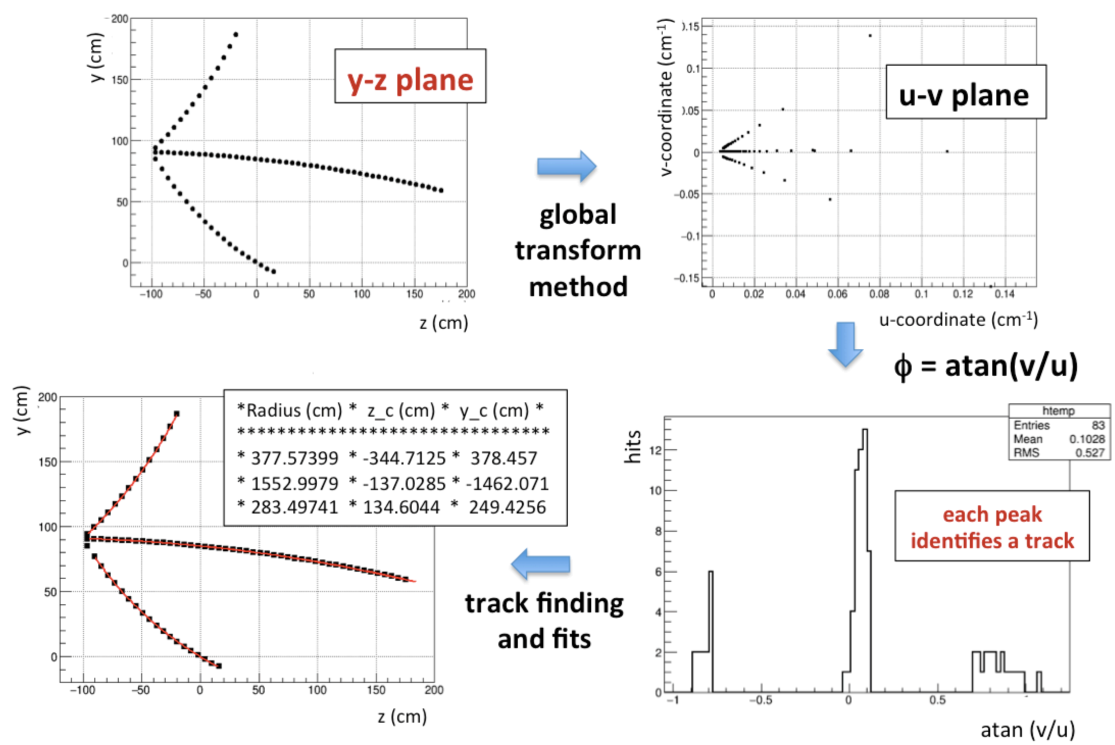

Figure 1.72: Full reconstruction of the event already shown in Fig. 1.71: the vertex is well reconstructed at *step 0* (left upper panel), the coordinate-transforms (right upper panel) allow the identification of ϕ peaks (right bottom panel) and the proper hits-track association. Finally the event is fully reconstructed and the track-fit parameters are reported in the left bottom panel.

of quasi-elastic neutrino interactions. As can be seen, about half of events in such sub-sample contain a single charged track. Such fraction is a little bit higher when the reconstructed tracks are considered.

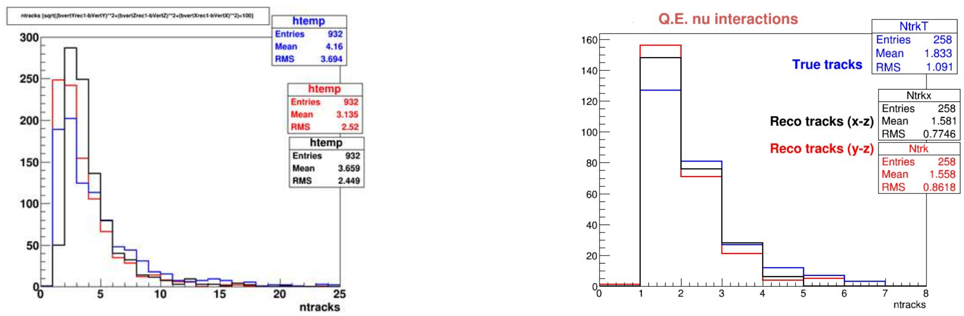

Figure 1.73: Fluka simulation, LAr meniscus - Multiplicity of reconstructed tracks using the procedure described in the text, compared with the MC charged particle multiplicity (requiring STT-hits ≥ 3). In the right plot the same comparison is shown for the quasi-elastic interaction sample.

The circular fit of tracks in the $y-z$ view allows to reconstruct the particle-momentum component in the bending plane (p_{yz}). The resulting percentage error track-by-track is shown in Fig. 1.74. In order to fully reconstruct the particle momentum, the dip-angle estimate is also needed (see Sec. 1.10.1.3), which requires an unambiguous match of the tracks in the two views. This can be easily obtained in the case of a single track reconstructed in $x-z$ and $y-z$ view. Therefore a single-track sub-sample was firstly considered for a first check of the reliability of this full-event reconstruction. The related resulting percentage errors on p_{yz}, dip-angle and p are shown in Fig. 1.75.

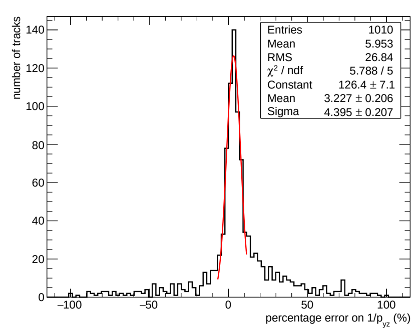

Figure 1.74: Fluka simulation, LAr meniscus - Percentage error on p_{yz} for each reconstructed track in the bending plane, for events with no more than three tracks.

1.10.7 Neutrino Energy Reconstruction in Inclusive CC Events

Since DUNE will be exposed to wide-band neutrino beam, the resolution of the near detector in reconstructing the neutrino energy is a key feature in order to fulfill the experimental physics goals.

1.10.7.1 Neutrino Interaction in STT

FLUKA simulation A sample of events from ν_μs interacting by CC in the STT, with at least one charged particle track, has been used to fully reconstruct the event and try to infer the neutrino

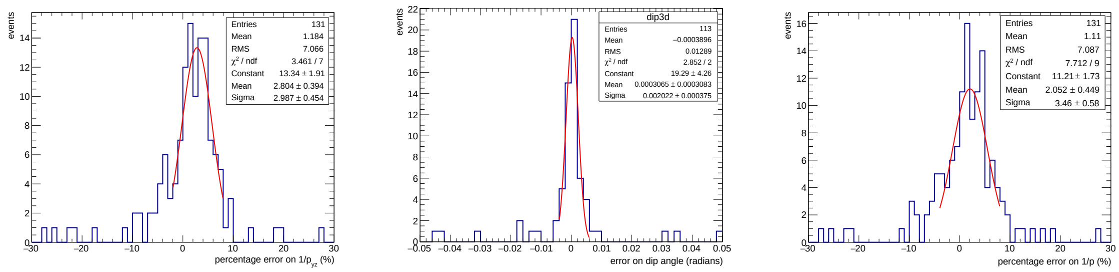

Figure 1.75: Fluka simulation, LAr meniscus - Percentage error on p_{yz} (left panel), dip-angle (central panel) and total p (right panel), for the sub-sample of events with a single track reconstructed in $x-z$ and $y-z$ view. The errors are referred to the particles (mainly muons) associated to the track.

energy. For this aim, firstly the charged particle tracks and momenta in the event have been reconstructed with the procedure described in previous section, after the association of STT digits to each track driven, in this case, by the MC. Then, the off-track energy deposited in the calorimeter has been finally added to the total energy of identified particle tracks, in order to estimate the interacting neutrino energy. ...

1.10.7.2 Neutrino Interaction in GRAIN

GEANT4 simulation In order to evaluate the energy resolution, about 50k muon neutrino CC interactions in the liquid argon meniscus have been generated using GENIE. The optimized flux presented at Oct 2017 Beam Optimization Review has been used [**?**]. The detector response to produced particles has been simulated using *Edep-sim* and a custom digitization process. The particle identification exploits the MC truth.

The STT digits of each track are grouped using the MC truth and then fitted applying least-squares method. The track model is a circle in the $z-y$ plane perpendicular to the magnetic field [**?**] and a straight line in $\rho-x$ plane as defined in [**?**]. The track is so described by seven parameters: the circle center (z_c, y_c), the radius (R), the initial angle (ϕ_0), the sense of rotation of the circle ($h=\pm1$), the initial x coordinate (x_0) and the dip angle (λ). Consequently the particle momentum is evaluated as:

$$\begin{aligned} p_\perp &= 0.29979 \cdot B \cdot R \\ p_x &= p_\perp \cdot \tan\lambda \\ p_y &= p_\perp \cdot \sin\phi_0 \\ p_z &= p_\perp \cdot \cos\phi_0 \end{aligned}$$

Neutrons, neutral pions and photons are reconstructed mainly using the information provided by the electromagnetic calorimeter. Time and charge of the two photomultiplier reading out the same cell are combined to obtain the energy deposit, time and longitudinal position of the hit. The hit transverse coordinate is given by the cell position. The calorimeter performances in term of time and electromagnetic energy resolution, as measured in [26], are well reproduced. The calorimeter hits related to the same particle are grouped in cluster using the MC truth. The momentum of the neutron originating from the neutrino interaction is obtained measuring its velocity. The path and time of flight is measured by the difference between the time and position of the interaction and the ones of the earlier calorimeter hit related to the neutron. Neutral pions momentum and energy are obtained by the ones of the daugther photons. The photons energy and direction are obtained either by measurements of electron and positron in case the photon converts before reaching the calorimeter or by the cluster of hits produced in the calorimeter. In the latter case, the photon energy is obtained by the sum of the deposited energy over the cluster and the direction is reconstructed linear fitting the deposited energy weighted averaged position evaluated layer by layer.

The neutrino energy is obtained summing up the kinetic energy of nucleons, assuming they are nuclear remnants, and the total energy of all the other particles. Comparing with the true values and fitting the Gaussian part of the residual distribution, a resolution of about 6% is obtained. The deviation from Gaussian behavior and the asymmetry is probably caused by the circular fit of the track which systematically underestimates the particle momentum.

1.10.7.3 Neutrino Interaction in Upstream CC

1.11 Analysis

1.11.1 Selection of CC Interactions

1.11.1.1 Kinematic Tagging of Leading CC Lepton

1.11.1.2 Selection of ν_μ & $\bar{\nu}_\mu$ CC Interactions

1.11.1.3 Selection of ν_e & $\bar{\nu}_e$ CC Interactions

1.11.2 Measurements of $\nu(\bar{\nu})$-Hydrogen Interactions

1.11.3 Determination of Relative and Absolute Fluxes

1.11.4 Constraining the Nuclear Smearing in Ar

1.11.5 ν-e Elastic Scattering

1.11.6 Coherent $\pi^{\pm}$ Production

1.11.7 ν_e/ν_μ & $\bar{\nu}_e/\bar{\nu}_\mu$ Flux Ratios

Low-ν relative flux...

1.11.8 On-Axis Beam Monitoring

1.11.8.1 Monitoring of the Beam Parameters

1.11.8.2 Monitoring of the Beam Direction

1.11.9 External Backgrounds

1.11.9.1 Expected Rates per Spill

1.11.9.2 Rejection of Random Neutron Background in $\nu(\bar{\nu})$-H Interactions

1.11.9.3 Rejection of Random Neutron Background in Inclusive $\nu(\bar{\nu})$ CC

1.11.9.4 Rejection of Rock Muons and Magnet Events in Upstream CC

1.11.9.5 Rejection of External Neutrino Interactions in STT

1.11.9.6 Pile-up Background in Upstream Barrel CC

1.12 Installation & Integration

Installation and integration, power, disposal ...
DOE standard, safety, logistic supply chain ...

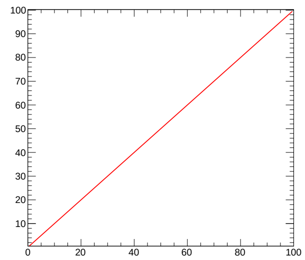

Figure 1.76: Dummy - Here insert the caption.

1.12.1 Organizational Structure and Sharing of Responsibilities

Storage area, mounting tools ...

1.12.2 Transport and Handling

Storage area ...

1.12.3 Experimental Hall and Facilities

Area (footprint) for mounting, cranes and special tooling for assembly, electrical infrastructure ...

1.12.4 Cryogenics and Gas Distribution

Area (footprint) for mounting ...
External, Proximity and Internal Cryogenics, gas system ...

1.12.5 Installation Sequence

Area (footprint) for mounting ...
Alcove area, gas system ...

1.12.6 Critical and Special Lifts

Area (footprint) for mounting ...
Alcove area, gas system ...

1.12.7 Commissioning

Sequence of operations ...

1.12.8 Safety

Applicable codes and safety infrastructure ...

1.12.9 Risk Matrix and Risk Management

Applicable codes and safety infrastructure ...

1.13 Safety

...

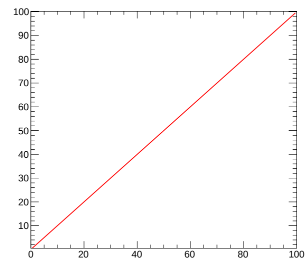

Figure 1.77: Dummy - Here insert the caption.

1.13.1 Applicable Codes and Standards

...

1.13.2 Organizational Structure

...

1.13.3 ORC List

... Operational readiness clearance (ORC) ...

1.13.4 Risk Matrices

...

Table 1.14: Dummy - An example of post-mitigation risk summary

1	ID	Risk	Mitigation	Probabil	Cost Impact	Schedule Impact
2	(id 1)	Sapien eget mi proin	Lorem ipsum dolor sit amet	L	M	L
3	(id 2)	Libero enim sed.	Urna cursus eget nunc	M	L	M
...						
n	(last id)	risk text	...	...	...	...

1.13.5 Risk Mitigation and Management

...

1.14 Organization & Management

Coordination of the groups participating in the R&D, assembling and operation of SAND is critical to successfully reach the scientific goals. Then, the SAND consortium has been created, Luca Stanco (Istituto Nazionale di Fisica Nucleare (INFN), Padua, Italy) and Claudio Montanari (INFN, Pavia, Italy) being appointed as Consortium Leader(CL) and Technical Leader (TL), respectively, by the DUNE management.

Internal boards have been setup:

- Advisory Committee (Sergio Bertolucci, Marco Pallavicini, Laura Patrizii, Roberto Petti, Milind Diwan and Bipul Buhyan)
- Steering Committee (Lea Di Noto, Matteo Tenti, Cl and TL)
- Consortium Board is foreseen but not yet defined

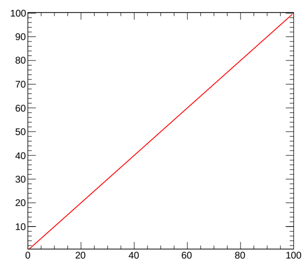

Figure 1.78: SAND consortium organizational chart.

Moreover, the consortium has been organized in Working groups (WG) related to each area of activity:

- ECAL - convenors: A. Di Domenico, D. Domenici
- GRAIN - convenors: L. Di Noto, A. Montanari
- STT - convenors: S. Di Falco, R. Petti, G. Sirri
- DAQ, trigger, timing and slow control - convenors: S. Di Domizio, C. Mariani, N. Tosi
- Physics, software - convenors: A Surdo, M. Tenti
- Calibration - convenor: P. Gauzzi

Evaluate the adequacy of the anticipated required resources
– Financial plan
– Human resources

- project organization and responsibilities
- people organization and management
- Milestones for SAND

1.14.1 Contribution by Fermilab

MoU

1.15 Time Schedule

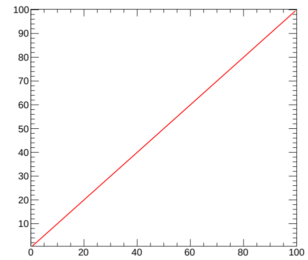

Figure 1.79: Dummy - Here insert the caption.

1.15.1 Resource-Loaded High Level Schedule

...

1.15.2 Working Groups Specific Resource-Loaded Schedules

1.15.2.1 KLOE-TO-SAND: Yoke, Magnet, ECAL

1.15.2.2 GRAIN

1.15.2.3 Tracker

1.15.2.4 DAQ, Trigger & Timing, Slow Controls

1.15.2.5 Integration, Installation and Commissioning

...

1.15.3 Milestones

...

1.15.4 Schedule-Related Risks

...

1.15.5 Schedule-Related Risk Mitigation and Management

...

Table 1.15: Example of a consortium X (fix short title, label and caption, and add your consortium items to table in chronological order among the fixed entries)

Item	Date (Month YYYY)
Start of module 0 component production for ProtoDUNE-II	(your date)
End of module 0 component production for ProtoDUNE-II	(your date)
Start of -II installation	March 2021
Beneficial occupancy of cavern 1 and central utility cavern (CUC)	October 2022
CUC counting room accessible.	April 2023
Top of #1 cryostat accessible	January 2024
End of (component 1) production	(your date)
...	...
Start of far detector module #1 TPC installation	August 2024
End of far detector module #1 TPC installation	May 2025
Top of far detector module #2 accessible	January 2025
Start of far detector module #2 TPC installation	...
End of far detector module #2 TPC installation	May 2026
...	...
last item	(your date)

1.16 Possible Upgrades

... [27]

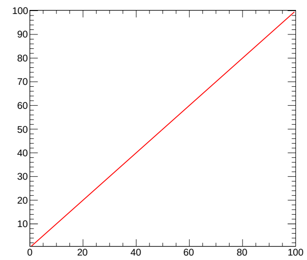

Figure 1.80: Dummy - Here insert the caption.

1.16.1 GRAIN Charge Readout

1.16.2 New Targets

Glossary

application-specific integrated circuit (ASIC) ASIC is an integrated circuit designed for a particular use. 20, 22

charged current (CC) Refers to an interaction between elementary particles where a charged weak force carrier (W^+ or W^-) is exchanged. 1, 42, 46

European Organization for Nuclear Research (CERN) The leading particle physics laboratory in Europe and home to the ProtoDUNEs. (In French, the Organisation Européenne pour la Recherche Nucléaire, derived from Conseil Européen pour la Recherche Nucléaire). 96, 97

conventional facilities (CF) Pertaining to construction and operation of buildings and conventional infrastructure, and for LBNF and DUNE project (LBNF/DUNE), CF includes the excavation caverns. 95

central utility cavern (CUC) The utility cavern at the 4850L of Sanford Underground Research Facility (SURF) located between the two detector caverns. It contains utilities such as central cryogenics and other systems, and the underground data center and control room. 92

data acquisition (DAQ) The data acquisition system accepts data from the detector front-end (FE) electronics, buffers the data, performs a , builds events from the selected data and delivers the result to the offline . ii, 8, 33, 36, 89, 91, 95, 97

Detector Control System (DCS) The system devoted to .... ii, iv, 33–37

dual-phase (DP) Distinguishes one of the DUNE far detector technologies by the fact that it operates using argon in both gas and liquid phases; sometimes called double-phase. 97

Detector Safety System (DSS) Independent system interacting directly with the Cryogenics, SAND detector sub-components in order to assure the safety of equipment, people, and various power supplies. ii, iv, 33, 34, 36–39

Deep Underground Neutrino Experiment (DUNE) A leading-edge, international experiment for neutrino science and proton decay studies. 95–97

electromagnetic calorimeter (ECAL) A detector component that measures energy deposition of traversing particles (in the near detector conceptual design). i, 2, 5, 33, 40–42, 89, 91

far detector module The entire DUNE far detector is segmented into four modules, each with a nominal 10 kt fiducial mass. 92, 97

far detector (FD) The 70 kt total (40 kt fiducial) mass liquid argon time-projection chamber (LArTPC) DUNE detector, composed of four 17.5 kt total (10 kt fiducial) mass modules, to be installed at the far site at SURF in Lead, SD, USA. 33, 96, 97

front-end (FE) The front-end refers a point that is "upstream" of the data flow for a particular subsystem. For example the single-phase (SP) front-end electronics is where the cold electronics meet the sense wires of the TPC and the front-end data acquisition (DAQ) is where the DAQ meets the output of the electronics. 33, 42, 94

front-end board (FEB) Board devoted to manage the detector signal. 33

Fermi National Accelerator Laboratory (Fermilab) U.S. national laboratory in Batavia, IL. It is the laboratory that hosts Deep Underground Neutrino Experiment (DUNE) and serves as its near site. i, iii, 9, 10, 15, 16, 90, 96

FLUktuierende KAskade (FLUKA) FLUKA is a fully integrated particle physics MonteCarlo simulation package. 43

far site conventional facilities (FSCF) The conventional facilities (CF) at the DUNE far detector site, SURF. 97

fiducial volume (FV) The detector volume within the time projection chamber (TPC) that is selected for physics analysis through cuts on reconstructed event position. 1, 42

GEometry ANd Tracking (Geant4) A software toolkit developed by CERN for the simulation of the passage of particles through matter using Monte Carlo (MC) methods. 42, 43

Generates Events for Neutrino Interaction Experiments (GENIE) Software providing an object-oriented neutrino interaction simulation resulting in kinematics of the products of the interaction. 46

GRanular Argon for Interactions of Neutrinos (GRAIN) Subdetector of System for on-Axis Neutrino Detection (SAND). ii, iii, 3, 18, 22, 33, 36, 40–42, 79, 83, 89, 91, 93

high voltage (HV) Generally describes a voltage applied to drive the motion of free electrons through some media, e.g., LAr. 8

Istituto Nazionale di Fisica Nucleare (INFN) Italian institution devoted to nuclear research. 89, 96

K-LOng Experiment (KLOE) KLOE is an e^+e^- collider detector spectrometer operated at DAFNE, the ϕ-meson factory at Frascati, Rome. In DUNE it will consist of a 26 cm Pb+scintillating fiber ECAL surrounding a cylindrical open detector region that is 4.00 m in diameter and 4.30 m long. The ECAL and detector region are embedded in a 0.6 T magnetic field created by a 4.86 m diameter superconducting coil and a 475 tonne iron yoke. 3, 91

liquid argon (LAr) Argon in its liquid phase; it is a cryogenic liquid with a boiling point of 87 K and density of 1.4 g/ml. i, 18, 21, 97

liquid argon time-projection chamber (LArTPC) A TPC filled with liquid argon; the basis for the DUNE far detector (FD) modules. 95

Long-Baseline Neutrino Facility (LBNF) The organizational entity responsible for developing the neutrino beam, the cryostats and cryogenics systems, and the conventional facilities for DUNE. 96, 97

LBNF and DUNE project (LBNF/DUNE) The overall global project, including Long-Baseline Neutrino Facility (LBNF) and DUNE. 94

Laboratori Nazionali di Frascati (LNF) Istituto Nazionale di Fisica Nucleare (INFN) laboratory in Italy. i, 9–11, 14, 16

Laboratori Nazionali di Legnaro (LNL) INFN laboratory in Italy. ii, 30

Monte Carlo (MC) Refers to a method of numerical integration that entails the statistical sampling of the integrand function. Forms the basis for some types of detector and physics simulations. 95

minimum ionizing particle (MIP) Refers to a particle traversing some medium such that the particle's mean energy loss is near the minimum. 6

neutral current (NC) Refers to an interaction between elementary particles where a neutrally charged weak force carrier (Z^0) is exchanged. 61

near detector (ND) Refers to the detector(s) installed close to the neutrino source at Fermi National Accelerator Laboratory (Fermilab). i, 7, 15, 33

operational readiness clearance (ORC) Final safety approval prior to the start of operation. 88

photomultiplier tube (PMT) A device that makes use of the photoelectric effect to produce an electrical signal from the arrival of optical photons. 5, 6, 8

ProtoDUNE Either of the two DUNE prototype detectors constructed at European Organization for Nuclear Research (CERN). One prototype implements SP technology and the other dual-phase (DP). 97

ProtoDUNE-SP The SP detector at CERN. 92

System for on-Axis Neutrino Detection (SAND) The beam monitor component of the near detector that remains on-axis at all times and serves as a dedicated neutrino spectrum monitor. i, ii, 1–93, 95

secondary DAQ buffer A secondary DAQ buffer holds a small subset of the full rate as selected by a . This buffer also marks the interface with the DUNE Offline. 94

silicon photomultiplier (SiPM) A solid-state avalanche photodiode sensitive to single photoelectron signals. 3, 6, 18, 20

single-phase (SP) Distinguishes one of the DUNE far detector technologies by the fact that it operates using argon in its liquid phase only. 95, 97

straw tube tracker (STT) Tracker in SAND. ii, iv, 3, 31, 33, 40, 42, 89

Sanford Underground Research Facility (SURF) The laboratory in South Dakota where the LBNF far site conventional facilities (FSCF) will be constructed and the DUNE FD will be installed and operated. 94, 95

time of flight (ToF) The time a particle takes to fly between two visible interactions observed in the detector. If combined with the distance traveled by the particle, for example a neutron, it can be used for energy reconstruction. 56

time projection chamber (TPC) A type of particle detector that uses an E field together with a sensitive volume of gas or liquid, e.g., liquid argon (LAr), to perform a 3D reconstruction of a particle trajectory or interaction. The activity is recorded by digitizing the waveforms of current induced on the anode as the distribution of ionization charge passes by or is collected on the electrode (TPC is also used for “total project cost”). 95, 96

trigger candidate Summary information derived from the full data stream and representing a contribution toward forming a trigger decision. 97

trigger command Information derived from one or more s that directs elements of the to read out a portion of the data stream. 97

trigger decision The process by which trigger candidates are converted into trigger commands. 94, 97

Transition Radiation Tracker (TRT) The TRT is a tracking system based on individual drift tubes (or straws) interleaved with fibres or foils. 42

References

[1] DOE Office of High Energy Physics, "Mission Need Statement for a Long-Baseline Neutrino Experiment (LBNE)," tech. rep., DOE, 2009. LBNE-doc-6259.

[2] A. A. Abud *et al.*, "Deep Underground Neutrino Experiment (DUNE) Near Detector Conceptual Design Report," *Instruments* **5** (2021) . `https://www.mdpi.com/2410-390X/5/4/31`.

[3] M. Adinolfi *et al.*, "The KLOE electromagnetic calorimeter," *Nuclear Instruments and Methods in Physics Research Section A: Accelerators, Spectrometers, Detectors and Associated Equipment* **482** (2002) 364. `https://www.sciencedirect.com/science/article/pii/S0168900201015029`.

[4] X.-G. Lu, L. Pickering, S. Dolan, G. Barr, D. Coplowe, Y. Uchida, D. Wark, M. Wascko, A. Weber, and T. Yuan, "Measurement of nuclear effects in neutrino interactions with minimal dependence on neutrino energy," *Phys. Rev. C* **94** no. 1, (2016) 015503, `arXiv:1512.05748 [nucl-th]`.

[5] A. P. Furmanski and J. T. Sobczyk, "Neutrino energy reconstruction from one muon and one proton events," *Phys. Rev. C* **95** no. 6, (2017) 065501, `arXiv:1609.03530 [hep-ex]`.

[6] **T2K** Collaboration, K. Abe *et al.*, "Characterization of nuclear effects in muon-neutrino scattering on hydrocarbon with a measurement of final-state kinematics and correlations in charged-current pionless interactions at T2K," *Phys. Rev.* **D98** no. 3, (2018) 032003, `arXiv:1802.05078 [hep-ex]`.

[7] S. Dolan, U. Mosel, K. Gallmeister, L. Pickering, and S. Bolognesi, "Sensitivity of Neutrino-Nucleus Interaction Measurements to 2p2h Excitations," *Phys. Rev. C* **98** no. 4, (2018) 045502, `arXiv:1804.09488 [hep-ex]`.

[8] X.-G. Lu, D. Coplowe, R. Shah, G. Barr, D. Wark, and A. Weber, "Reconstruction of Energy Spectra of Neutrino Beams Independent of Nuclear Effects," *Phys. Rev. D* **92** no. 5, (2015) 051302, `arXiv:1507.00967 [hep-ex]`.

[9] **MINERvA** Collaboration, X. Lu *et al.*, "Measurement of final-state correlations in neutrino muon-proton mesonless production on hydrocarbon at $\langle E_\nu \rangle = 3$ GeV," *Phys. Rev.*

Lett. **121** no. 2, (2018) 022504, arXiv:1805.05486 [hep-ex].

[10] S. Dolan, "Exploring Nuclear Effects in Neutrino-Nucleus Interactions Using Measurements of Transverse Kinematic Imbalance from T2K and MINERvA," arXiv:1810.06043 [hep-ex].

[11] X.-G. Lu and J. T. Sobczyk, "Identification of nuclear effects in neutrino and antineutrino interactions on nuclei using generalized final-state correlations," *Phys. Rev. C* **99** no. 5, (2019) 055504, arXiv:1901.06411 [hep-ph].

[12] L. Harewood and R. Gran, "Elastic hadron-nucleus scattering in neutrino-nucleus reactions and transverse kinematics measurements," arXiv:1906.10576 [hep-ex].

[13] T. Cai, X.-G. Lu, and D. Ruterbories, "Pion-proton correlation in neutrino interactions on nuclei," *Phys. Rev. D* **100** (2019) 073010, arXiv:1907.11212 [hep-ex].

[14] **MINERvA** Collaboration, T. Cai *et al.*, "Nucleon binding energy and transverse momentum imbalance in neutrino-nucleus reactions," *Phys. Rev. D* **101** no. 9, (2020) 092001, arXiv:1910.08658 [hep-ex].

[15] **MINERvA** Collaboration, D. Coplowe *et al.*, "Probing Nuclear Effects with Neutrino-induced Charged-Current Neutral Pion Production," arXiv:2002.05812 [hep-ex].

[16] H. Duyang, B. Guo, S. R. Mishra, and R. Petti, "A Novel Approach to Neutrino-Hydrogen Measurements," arXiv:1809.08752 [hep-ph].

[17] H. Duyang, B. Guo, S. Mishra, and R. Petti, "A Precise Determination of (Anti)neutrino Fluxes with (Anti)neutrino-Hydrogen Interactions," *Phys. Lett. B* **795** (2019) 424–431, arXiv:1902.09480 [hep-ph].

[18] "https://www.digchip.com/datasheets/parts/datasheet/190/r5946.php.".

[19] F. Alemanno, P. Bernardini, A. Corvaglia, G. D. Matteis, L. Martina, A. Miccoli, M. Panareo, M. P. Panetta, C. Pinto, and A. Surdo, "Study of silicon photomultipliers for the readout of a lead/scintillating-fiber calorimeter," 2024.

[20] M. Andreotti *et al.*, "Coded masks for imaging of neutrino events," *The European Physical Journal C* **81** (2021) 1011. http://dx.doi.org/10.1140/epjc/s10052-021-09798-y.

[21] R. I. Hartley and A. Zisserman, *Multiple View Geometry in Computer Vision*. Cambridge University Press, ISBN: 0521540518, second ed., 2004.

[22] G. H. Golub and C. F. Van Loan, *Matrix Computations*. The Johns Hopkins University Press, fourth ed., 2013.

[23] E. Abat *et al.*, "The ATLAS TRT electronics," *JINST* **3** (2008) P06007.

[24] F. Ragusa, "An Introduction to Charged Particles Tracking." www.mi.infn.it/~ragusa/tracking_sns_28.05.2014.pdf.

[25] G. Bassompierre, S. Bunyatov, T. Fazio, J.-M. Gaillard, M. Gouanère, E. Manola-Poggioli, L. Mossuz, J.-P. Mendiburu, P. Nédélec, Y. Nefedov, H. Pessard, D. Sillou, V. Valuev, and D. Verkindt, "Performance of the nomad transition radiation detector," *Nuclear Instruments and Methods in Physics Research Section A: Accelerators, Spectrometers, Detectors and Associated Equipment* **411** no. 1, (1998) 63–74. https://www.sciencedirect.com/science/article/pii/S0168900298001053.

[26] M. Adinolfi *et al.*, "The KLOE electromagnetic calorimeter," *Nucl. Instrum. Meth.* **A482** (2002) 364–386.

[27] B. Abi *et al.*, "Long-baseline neutrino oscillation physics potential of the DUNE experiment," *The European Physical Journal C* **80** (2020) 978.